Multi-spectral System for Autonomous Robotic Location of Fires Indoors

Brian Matthew Keller

Thesis submitted to the faculty of the Virginia Polytechnic Institute and State University in partial fulfillment of the requirements for the degree of

Master of Science
In
Mechanical Engineering

Brian Y. Lattimer
Kevin B. Kochersberger
Alexander Leonessa

April 25th, 2013
Blacksburg, VA

Keywords: Fire, Infrared, Ultraviolet, Firefighting, Autonomous

Multi-spectral System for Autonomous Robotic Location of Fires Indoors

Brian Matthew Keller

ABSTRACT

Autonomous firefighting platforms are being developed to support firefighters. One aspect of this is location of a fire inside a structure. A multi-spectral sensor platform and fire location algorithm was developed in this research to locate a fire indoors autonomously.

The multi-spectral sensor platform used a long wavelength infrared (LWIR) camera and ultraviolet (UV) sensor. The LWIR camera was chosen for its ability to see through smoke, while the UV sensor was selected for its ability to discriminate between fires and non-fire hot objects. The fire location algorithm by radiation emission (FLARE) developed in this research used the multi-spectral sensor data to provide the robot heading angle toward the fire.

The system was tested in a large-scale structural fire facility. A series of 20 different scenarios were used to evaluate the robustness of the system including different fuel types, structural features, non-fire hot objects, and potential robot positions within the enclosure. This demonstrated that FLARE could direct a robot towards the fire regardless of these variables.

Directional fire discrimination was added to the platform by limiting the field of view of the UV sensor to that of the LWIR cameras. Three methods were evaluated to limit the field of view of a UV sensor. These included angled plate housing, bulb cover, and slit opening housing methods. The slit opening housing method was recommended for ease of implementation and size required to limit the field of view of the sensor to the desired value.

Dedication

The work contained in this thesis is dedicated to firefighters who serve and protect by putting their lives on the line in hostile environments.

Acknowledgements

I would like to express my gratitude to my savior Jesus Christ and the following persons for their enduring support throughout my completion of this work.

Dr. Brian Y. Lattimer—thank you for serving as my primary advisor and recruiting me to the SAFFiR project. The constant advice, encouragement, and understanding kept me afloat throughout my studies. From the time I took undergraduate Thermodynamics, you have served as a mentor and my favorite professor.

Dr. Alexander Leonessa and Dr. Kevin Kochersberger—thank you for serving on my graduate advisory committee.

Joseph W. Starr—thank you for the never ending Facebook chats and discussions about life, research, faith, and ideologies. Thank you for your time, patience, and unwavering convictions.

Josh McNeil—thank you for your time. You were always being willing to lend your extensive machining and fabrication expertise.

Jonghwan Kim—thank you for your hard work and patience in integrating the localization and obstacle avoidance with my algorithms.

Nathan Cholewa—thank you for your time and assistance with testing unrelated to your work.

Patrick Summers—thank you for always being around to answer questions for anyone who asked.

I would like to thank the Virginia Tech Department of Mechanical Engineering, students from RoMeLa and UPenn who worked on the SAFFiR project, and the rest of the EXTREME lab. In addition, I would like to thank the Naval Research Lab (NRL) and Office of Naval Research (ONR) for funding the SAFFiR project and affording me the opportunity to do the work contained in this thesis.

Finally, I would like to thank all my family, especially my parents, CH (MAJ) William and Lori Keller, for their incredible emotional and financial support to give me the opportunities I have had in life. Thanks go to my most influential high school math teacher, Mrs. Emma Mackay. Thanks go to my strongest extracurricular supporter and advisor, Lynn Nystrom. Finally, thanks go to the brothers of the Beta Theta Pi that have made Blacksburg my home.

Contents

List of Figures

Chapter 1:

Chapter 2:

Chapter 3:

Chapter 4:

Appendix A:

Appendix B:

Appendix C:

List of Tables

Chapter 1

Chapter 3

Chapter 4

List of Abbreviations

FLARE – Fire Location Algorithm by Radiation Emission (FLARE)

FTIR - Fourier Transform Infrared Spectrometers

LWIR – Long Wave Infrared

MWIR – Mid Wave Infrared

SAFFiR – Shipboard Autonomous Firefighting Robot

SWIR - Short Wave Infrared

UV - Ultraviolet

List of Variables

B – Input LWIR image
C – Visibility constant
d - Width of UV sensor
D – LWIR maximum-average difference
I_o – Baseline laser intensity
I – Laser intensity
L – Smoke depth
L_b - Average intensity for IR fire detection
L_{th} - Reference intensity for IR fire detection
M – Infrared camera intensity
n – Noise
P – Distance between sensor and plate join for angled plate opening method
PN-Number of UV peaks per second
R – Horizontal image resolution
t - Time
t_a – Atmospheric transmission coefficient
T_{FD} - IR fire detection threshold
T_{HO} – Experimental FLARE Hot Object threshold
T_{UV} – Experimental FLARE UV analysis threshold
V – Visibility
VSX – Selected vertical step pixel coordinate
VX - Final pixel coordinate
w – Width of housing opening for bulb cover and slit opening methods
X – Original hottest column pixel coordinate
y – Distance between sensor and cover for bulb cover and slit opening methods
Y – Vertical image resolution
α – Plate opening angle for angled plate opening method
β – Final heading angle
$\boldsymbol{\varepsilon}$ – Emissivity
θ - Field of view of UV sensor
σ – Extinction coefficient

Chapter 1: Introduction

1.1 Background and Motivation

When a fire occurs, the initial reaction for a human is to move away from high temperatures or emerging smoke. This can be accomplished by dropping below the height of the smoke layer, to cooler temperatures, or just moving quickly away from the hot area. Firefighting flies in the face of this instinct, with the goal of finding the fire and extinguishing it as quickly as possible. There is a lot of risk for human firefighters who combat high temperatures, toxic levels of combustion product gases, and dangers of failing structures surrounding them. According to FEMA [1], 83 firefighters were killed in the U.S. alone in 2012. Robotic systems are being developed to support firefighters during emergency events in order to reduce injuries and deaths.

Robotic developers have been consistently challenged with developing ways for robots to enter harsh environments on behalf of their human counterparts. Early examples include IED robots being used by the U.S. in the Middle East to disarm explosives. The DARPA Robotics Challenge (DRC) challenges researchers to develop autonomous disaster response robots.

Robotic firefighting is a fairly new field with global attention. There are several commercially available examples. OLE's First INTelligent Extinguisher (FINE) is an autonomous model that can detect combustible gases and extinguish small fires within its field of view. DRB Fatec's Archibot-M is another autonomous firefighting robot that is capable of fire detection and suppression. The Hoya firefighter's assistant from South Korea is a remote controlled robot capable of sending firefighters details about temperatures, gas concentrations, as well as video of the fire environment. Other remote controlled robots that are capable of entering fire environments and fighting the fire include Howe and Howe

Technologies Thermite-RS1-T2, IZ Holding's Firo, and Ryland Research's Firemote. Trinity College hosts an annual autonomous firefighting robot competition.

The Trinity College competition, the DRB Fatec Archibot-M robot, and the FINE robot showcase challenges in the autonomous robotic firefighting research area. The fires these robots seek are often very small like candles or kitchen trash fires, which are not representative of the poor visibility and high temperature conditions a true firefighting robot will have to endure in service. Additionally, the robots search the area and check all rooms until they find the fire, rather than navigating with a purpose.

The shipboard autonomous firefighting robot (SAFFiR) is a humanoid firefighting robot that is being developed to autonomously locate and suppress fires. Autonomous navigation to the fire requires the robot to combine information about the environment with its existing obstacle avoidance and localization algorithms in order to seek and find the fire intelligently. This opens the door for true autonomous firefighting in industrial, residential, and forest fire conditions independent of firefighters entering the environment themselves.

1.2 Literature Review

Robotic firefighting is not a particularly dense topic in the literature. The most closely related well-studied topic to this is fire detection. Fire detection has been attempted based on a variety of methods including visible imaging, infrared (IR) imaging, ultraviolet (UV) sensors, and other methods.

Visible cameras are very low cost systems compared to many fire detection alternatives. There are several different methods for fire detection using visible cameras found in the literature. Celik et al. [2, 3] proposed using the RGB values making up the images to identify a fire based on thresholds. This has many

shortcomings including false alarms caused by other things in the scene the same color as the fire. Beyond using RGB values, luminance and chrominance (Y, Cb, and Cr) are used by Celik et al. [4, 5] to detect fires. For a more robust approach, Celik et al [6] combined the previous method with fuzzy logic. Toreyin et al. [7] presented visible image analysis in the wavelet domain used to detect flame flicker at 10 Hz. Ko et al. [8] combined many of the existing methods by applying background subtraction, color analysis, and flame movement analysis with Bayesian statistical networks to determine the presence of fires. While this method appears to have worked well, it is a passive system, which is not directly applicable to a mobile robot. Most of the above referenced literature note that visible cameras are not ideal for moving in smoke filled high temperature environments.

Combustion product emission has also been used to locate gas emitting bodies with gas concentration sensors. Ishida et al. [9] used a visual camera, gas concentration sensors, and airflow sensors to search for a gas source. Similarly, Marjovi et al. [10] used multiple robots with gas concentration sensors, air flow sensors, and map merging techniques to locate an emission source. These methods had many potential problems. These methods of locating combustion product sources are not always applicable indoors due to small air flow velocities. Gas concentration sensors provide local measurements which make it difficult to get a full perspective of the 3D thermal and emission environment created by a fire within a large-scale structure.

The infrared spectrum has numerous applications that could potentially be applied to detecting and locating a fire. Fourier transform infrared spectrometers (FTIR) can give spectral signatures of combustion products like CO_2, H_2O, CO, N_2O, NO, and SO_2 as shown by Heland et al. [11]. Rego-Barcena et al. [12] have used FTIR to get temperatures for a desired radiation wavelength range. Chaffin et

al. [13] publicized the parameters required for accurate measurements. These parameters present drawbacks for the mobile application of FTIR. Accurate spectral signature information using FTIR requires temperature and composition of the plume, temperature and composition of the background, ambient atmospheric conditions and distance to the plume, temperature dependent spectral characteristics of the plume constituents, and unique response characteristics of the applied sensor. FTIR has the capability to describe the type of fire encountered or the temperatures observed; however, it is clear that this cannot be used with a mobile robot and constant variation of the frame of reference.

Infrared imaging has its own unique advantages and characteristics. Kostrzewa et al. [14] established the challenges faced by thermal imagers including extreme ambient temperatures, dynamic pixel range, temperature gauging, portability, ease of use, protection from harsh environments, and low cost. Many of these challenges have been addressed to some extent in recent years. Amon et al. [15] provided Table 1 listing the different conditions for which human emergency responders use thermal imaging cameras.

Table 1. First responder thermal imaging camera operations [15]

Activity	Description
Size up	Assess hazard, find fire/heat sources, escape points, and vents
Communication	Lead or direct searches, interface with incident command, account for team members
Search	Locate victims, other first responders, fugitives, missing persons in dark and/or smoky environments
Tactics	Direct hose stream, check upper layer temperature, check for changing conditions, detect obstacles, passageways, damaged structural members, judge distances, use in rapid intervention teams
Overhaul	Ensure fire is out, look for hidden smoldering and hot spots
Forensics	Identify source of fire, determine fire spread, record video during fire for later use as evidence
Wildland Fires	Ground and air based search for hot spots and personnel
Hazmat	Determine material levels inside containers, track material movement and spill spread limits
Other	Preventative building maintenance, emergency medical applications, motor vehicle accident investigations

Amon et al. [16] evaluated many thermal-imaging requirements for human firefighting applications. The study found that a selected thermal imager's capabilities are independent of the fuel type. The expected thermal event class determines the specifications required of the selected thermal imager for use by firefighters according to Amon et al. [15]

Thermal imagers used by humans in fire scenarios can be heavily affected by the bit depth or pixel intensity range. Cameras outputting 8 bit data have 255 output pixel values, while 14 bit data has a range of 16383 points. This affects the contrast and the information a human can gauge from an image. Amon et al. [17] tested to find the effective temperature range of several thermal imagers for human interpretation by raising the temperature of one target and keeping another constant while measuring the contrast.

Infrared cameras exist in several different wavelength ranges listed by Vollmer et al [18]. Short wavelength infrared (SWIR) is the 0.9-3 μm range, mid wavelength infrared (MWIR) 3-6 μm, and long wavelength infrared (LWIR) exists in the 7.5-13.5 μm. Most IR cameras used in research are based around an uncooled microbolometer sensor. Amon et al. [16] pointed out two different types of these sensors including vanadium oxide (VO_x) and amorphous silicon (ASi). Radiation at a certain wavelength hits the sensor and heats it, thus changing the electrical resistance. These sensors have been reported to be less sensitive than HgCdTe based photonic infrared detectors by Katayama et al. [19]. The cameras with these sensors can output intensity readings (M) that can be correlated to temperature as in Equation 1,

$$M = t_a \varepsilon \int_{\lambda_1}^{\lambda_2} \lambda T^4 d\lambda \qquad \mathbf{1}$$

where t_a is the atmospheric transmission coefficient, ε is the blackbody emissivity, λ is the wavelength, and T is the temperature.

Some commercial infrared cameras like those provided by FLIR are then proprietarily scaled to output temperature. The temperature ranges for the cameras vary to as high as 2000°C. The image will be saturated when the temperature range of the camera is exceeded. Accurate temperature measurements using IR cameras are faced with the many challenges presented by Vollmer et al. [18]. These problems include knowledge and user input of the emissivity of every material present in the scene and the assumption that that emissivity is spectrally independent. The error of assuming constant emissivity increases with temperature.

Amon et al. [16] showed that infrared (IR) attenuation by smoke decreases as the wavelength range increases, allowing a LWIR camera to see through smoke. Starr et al. [21] described this phenomenon by describing an inverse relationship between the extinction coefficient and wavelength for IR. The relationship between visibility and extinction coefficient is shown with Jin's formula in Equation 2,

$$V = \frac{C}{\sigma} \qquad \mathbf{2}$$

where σ is the extinction coefficient, C is a constant between 2 and 4 for light reflecting objects, and V is the visibility. Visibility is distance that a person could read a sign through a medium. This advocates the use of the LWIR range when selecting a camera robust to testing with varying fire types.

Infrared imaging has been used to detect smoke as well as temperatures. One method of infrared camera smoke detection is the mean cross rate algorithm published by Liu et al. [22]. The mean cross rate determines smoke presence over interference using the changes in intensity readings as smoke enters the scene. For mobile robotic applications this is not particularly helpful, as it requires the robot to be stationary for some period of time to establish a frame of reference. Also, the research on this particular algorithm is far from broad, with testing on small-scale

fires. This type of algorithm is susceptible to false alarms caused by humans entering the scene, or any other type of time variant thermal event other than smoke.

Infrared imaging has also been used to detect fires. Similar to the work with visible cameras, Toreyin et al. [23] focused on detecting the dynamic flicker of the flame in IR images using wavelet analysis. Flame flicker is reported to be at 10 Hz. Simple threshold analysis is more common in the literature. This method refers to checking the intensities located in the frame against a target value representing the lowest possible intensity that can be considered a fire. Owrutsky and Gottuk et al. [24, 25] showed one general method which used Equations 3 and 4,

$$L_{th} = 2\sqrt{L_b} \quad \textbf{3}$$

$$T_{FD} = L_{th} + L_b \quad \textbf{4}$$

where L_{th} is a reference intensity added to the average intensity in the scene, $L_{b,}$ to determine the threshold, T_{FD}. This method is far too general for many applications. This method excludes the possibility of a false alarm caused by the presence of a non-fire hot object distinctly hotter than the rest of the scene. These objects can be things like uncovered lights, steam pipes, or heaters, all of which can be present in residential or industrial locations. If the IR camera outputs temperatures, the threshold method is still not robustly applicable as fire and isolated hot object temperature ranges can overlap. These threshold methods may also detect heated surfaces near the original fire location for some time after the fire is extinguished. This can make it difficult to recognize when the fire is actually suppressed. IR imaging may not be sufficient to discriminate between these non-fire hot objects and fires.

Light emitted from the flame can be used to detect the fire. Docquier et al. [26] described this as discrete emission spectra appearing in the UV-visible spectrum as a result of combustion chemical reactions, which produce electronically excited radicals. Weiser et al. [27] showed the presence of many combustion products within the UV range for RDX/Estane and Nitromethane flames in Figure 1. Nussbaum et al. [28] stated that UV radiation is known to be emitted by gas and oil flames.

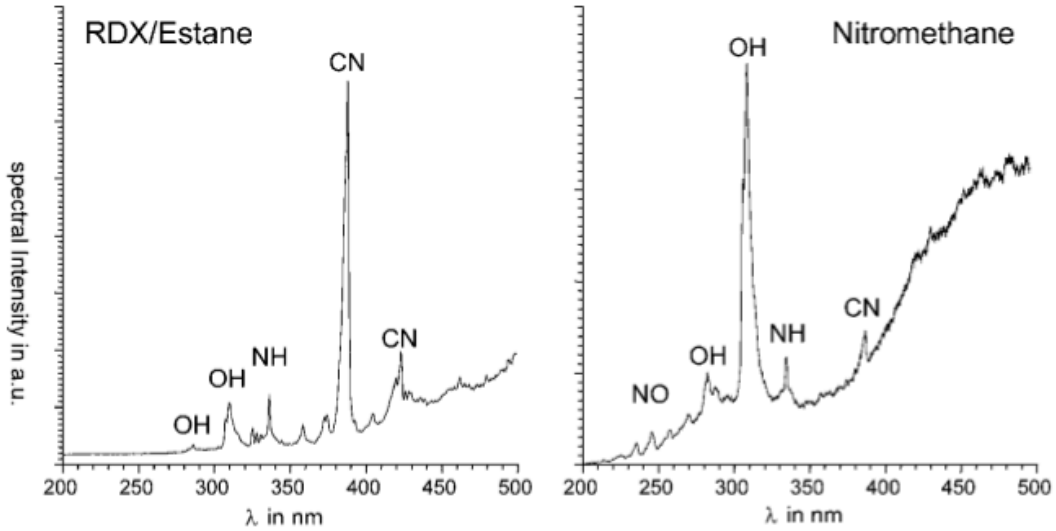

Figure 1. Combustion product spectral intensity peaks in the UV spectrum for RDX propellant and Nitromethane flames [27]

Monroy et al. [29] broke down UV radiation into four different ranges. The far UV is 10-200 nm, UV C is 200-280 nm, UV B is 280-320 nm, and UV A is 320-400 nm. Monroy et al. [29] stated that UV sensors with ranges below 280 nm are safe from sunlight. This in turn means both the UV A and UV B ranges are susceptible to UV from the sun. In addition some lighting can emit UV radiation in the UV A range as shown by the specification sheet image for the Hamamatsu UVTRON R9454 UV sensor in Figure 2. This sensor operates in the far UV, which allows it avoid UV rays from sunlight as well as other various light sources

while remaining sensitive to gas flames. Cote [30] listed the many types of fires UV sensors respond to including hydrocarbons, ammonia, sulfur, hydrogen, hydrazine, and metals like magnesium.

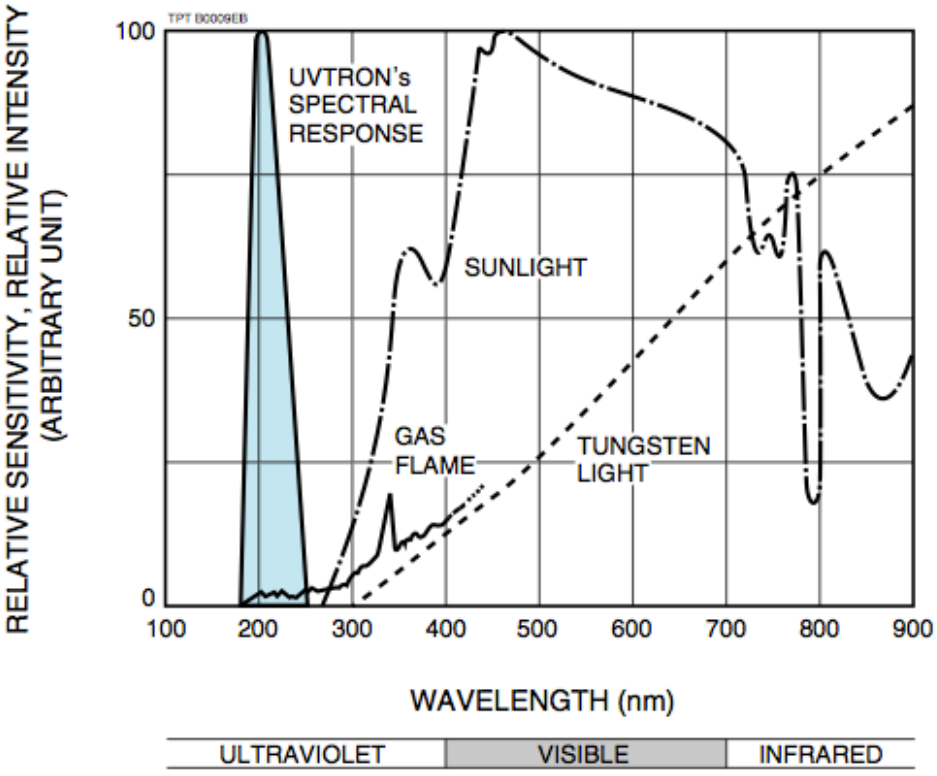

Figure 2. UVTRON R9454 spectral response against light sources, [31], used with the permission of Leo Kohyama, Hamamatsu Corporation, 2013

UV sensors vary by material type, electronic type, distance range, wavelength sensing range, temperature range, charge transfer efficiency, and responsivity. UV sensors can be made with many different types of materials including SiC Diamond, AlGaN, N, GaN, ZnS, and ZnSe. Monroy et al. [32] listed the different UV sensor electronic types including metal-oxide diodes, shottky diodes, charge coupled and particle detector sensors, P-N junction photodiodes, P-I-N junction photodiodes, and photoconductors. Far UV and UV C wavelength range sensors have a few isolated false alarm modes enumerated by

Street et al. [33], caused by arc welding, lightning, electric sparks, halogen, sterilization lamps, and high electric or static fields. Cote et al. [30] and Watkins [34] showed that UV radiation is absorbed by hydrocarbon vapors like acetone, ethanol, ammonia, benzene, or black smoke like that from petroleum. UV sensors have the potential for directional discrimination because the sensor must have an unobstructed view of the flame as stated by Nussbaum et al. [28].

1.3 Research Objectives

The objective of this research was the development of a multi-spectral sensor platform and algorithm that guides an autonomous robot towards a fire inside a structure. Current autonomous firefighting robots do not have a method for seeking and finding the location of a fire outside of view. The algorithm should guide a prospective robot to the location of an indoor fire outside of view. The algorithm should contain a method of stopping the robot when the fire is reached. In addition, the algorithm must be capable of discriminating between non-fire hot objects and the fire.

These objectives were accomplished by identifying the sensors for use on the multi-spectral platform. LWIR cameras were used in order to see in and thermally describe indoor low visibility fire scenarios. A far to mid-C UV sensor was used in order to discriminate between non-fire hot objects and true fires within the field of view of the LWIR camera. The sensors and algorithm logic were then tested at different potential robot positions in a large-scale fire environment enclosure with different fuel types, structural features, and non-fire hot objects. The algorithm was validated using the fire test data.

1.4 Outline of Thesis

This thesis is organized into four chapters in addition to this one. The equipment, lab set up, and conditions used to test the algorithms and sensors are presented in Chapter 2. The fire location algorithm and the results for a different fire types and expected robot positions are provided in Chapter 3. Results of different attempts to use the UV sensors for directional fire discrimination are given in Chapter 4. The result of testing to show the UV sensor's ability to operate in low visibility conditions is also provided in Chapter 4. Chapter 5 contains the conclusions of this research effort and recommendations for future work.

Chapter 2: Experimental Methods

2.1 Sensors

Several sensors were used for the fire location algorithm. This included LWIR cameras and UV sensors. The LWIR cameras were chosen specifically for their ability to see through heavy smoke conditions and provide relative temperature information using black body intensity values [16, 21]. A UV sensor in the far to mid-C UV range was chosen to discriminate between non-fire hot objects and actual fires. [29, 30, 34].

The specific LWIR cameras chosen were the FLIR Tau 2-320 and the FLIR A35 shown in Figure 3. Both cameras use VO_x uncooled microbolometer sensors and have 9 mm lenses. The specified temperature range of the IR cameras is -40°C to 550°C with a wavelength range between 7.5-13.5 μm. The FLIR cameras have many adjustable gain and range settings; however, the raw data was taken in 14-bit form with 324x256 pixel resolution for the FLIR Tau 2-320 and 320x256 resolution for the FLIR A35. The FLIR Tau 2-320 data was analyzed with unsigned integer values and the FLIR A35 data was brought in as signed integer values based on LABVIEW preferences. The FLIR Tau 2-320 was powered using USB and the data was imported using the Imperx Framelink Express VCE-CLEX01 PCI-express card with the FLIR Tau Camera Link Expansion Board. This was not the best type of connection for implementation on a compact robot. The FLIR A35 was powered and data was imported using Ethernet. The operating temperature range of both cameras is -15°C to 50°C. The cameras are also small. The FLIR Tau 2-320 weighs 72 grams and is 0.045 m by 0.045 m by 0.03 m. The FLIR A35 weighs 200 grams and 0.11 m by 0.041 m by 0.043 m.

Figure 3. LWIR cameras used, FLIR A35 (left), FLIR Tau 2-320 (right)

The chosen UV sensor for fire detection was the Hamamatsu UVTRON R9454 with the corresponding C10423 driving circuit. This sensor operates in the far to mid-C UV range from 185-260 nm. The operating temperature range is -10°C to 50°C. The UV sensor is a metal oxide diode with Ni as the metal material. The bulb is made of glass. The bulb is approximately 0.012 m in diameter at the widest point and 0.056 m tall. The C10423 circuit is 0.05 m by 0.036 m by 0.016 m. A picture of the UV sensor connected to the driving circuit is shown below in Figure 4. The vertical and horizontal fields of view of the UVTRON R9454 sensor are shown in Figure 5 provided by Hamamatsu. Both the LWIR cameras and the UV sensors are shown with their ranges in the electromagnetic spectrum in Figure 6.

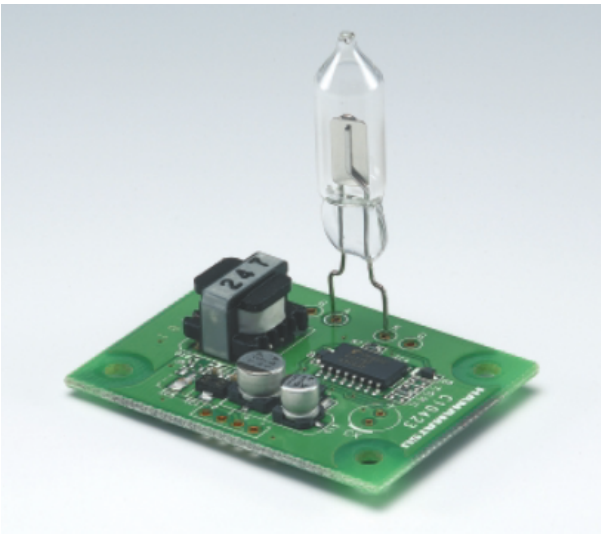

Figure 4. UVTRON R9454 and C10423 driving circuit, [35], used with the permission of Leo Kohyama, Hamamatsu Corporation, 2013

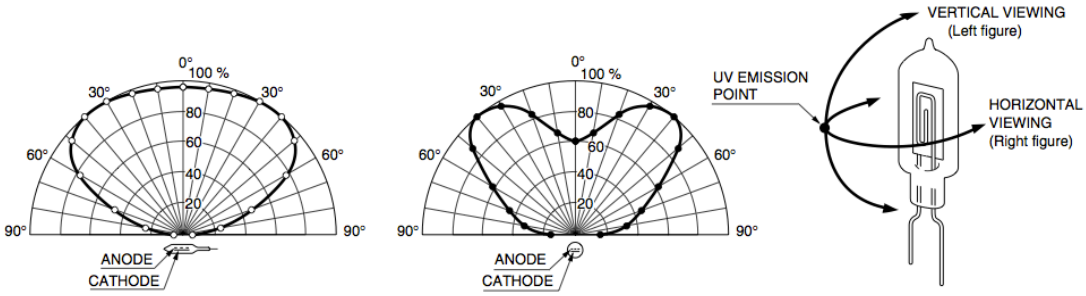

Figure 5. Field of view of UVTRON R9454 bulb, [31], used with the permission of Leo Kohyama, Hamamatsu Corporation, 2013

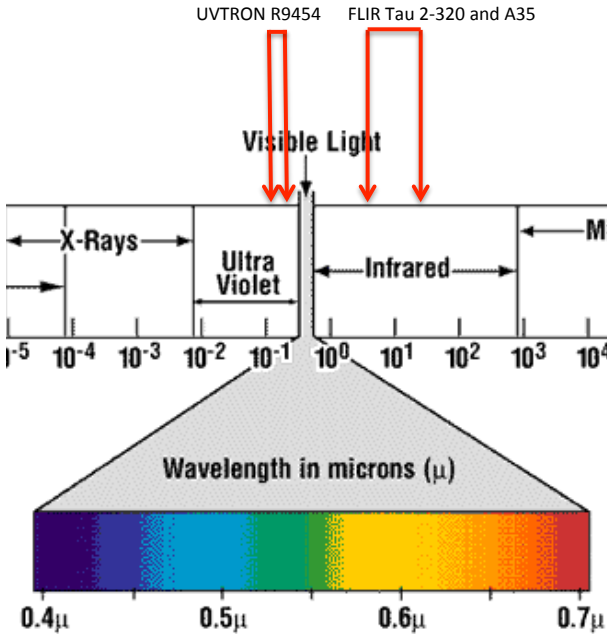

Figure 6. Location of sensors selected in the electromagnetic spectrum

The strength of the UV signal seen by the UVTRON R9454 is determined by the pulse width. This classification between weak (green), normal (yellow), and strong (red) UV radiation is shown below in Figure 7 by a diagram provided by Hamamatsu. The fire was not considered located until a pulse width less than 0.2 seconds occurred. A 0.2 second pulse width corresponds to five 5 V peaks in one second.

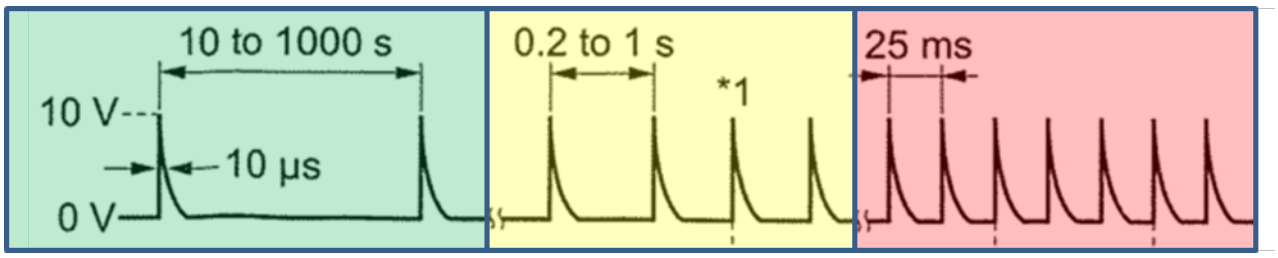

Figure 7. UVTRON R9454 strength of radiation based on pulse width, [36], used with the permission of Leo Kohyama, Hamamatsu Corporation, 2013

2.2. Experimental Set Up

Large-scale indoor fire tests were performed using the fire test facility shown in Figure 8. The facility contains a multi-room/hallway fire environment enclosure to generate fire conditions that may occur inside a structure during a fire. Smoke flows out of the end of the hallway up into an exhaust hood to remove products from the laboratory. The top 0.70 m of the end of the hallway beneath the hood is blocked to create a smoke layer 0.70 m deep within the fire environment enclosure. The facility was equipped with a ventilation system that can exhaust gas at flow rates up to 2.36 (m^3/s). A red X designates fire locations used in this research.

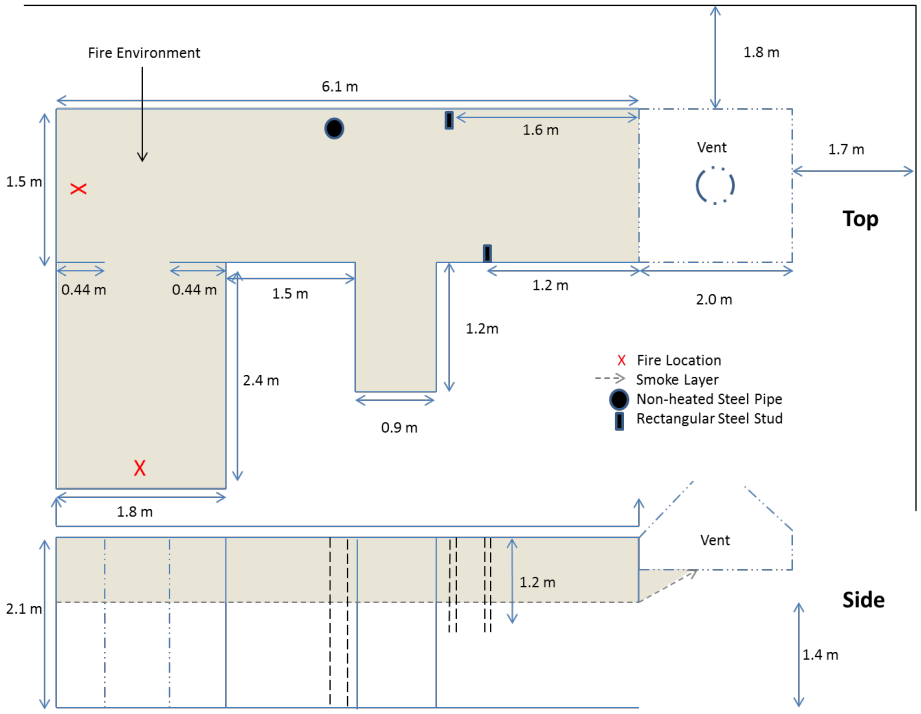

Figure 8. Multi-room/hallway indoor fire environment enclosure with dimensions and possible fire locations

Some of the algorithm testing in this research required a non-fire hot object that was hotter than the rest of the scene. Tempco screw in ceramic E-Mitter enclosure heaters were used for this purpose. These heaters can reach temperatures

above 100°C. The heater was allowed to heat up for at least five minutes before each test began. For tests where the heater was used to heat a steel column simulating a heated pipe, the heater was allowed to heat up for thirty minutes prior to testing.

Gas temperatures were measured throughout the room/hallway enclosure in order to quantify the thermal environment for each test. Temperature was measured with bare bead, 24 gauge wire, Type K thermocouples. Vertical gas temperature distributions were measured 0.01 m off of the wall in the hallway at three locations, denoted as A, B, and C in Figure 9. These thermocouples were placed at 0.15 m, 0.45 m, 0.81 m, 1.00 m, and 1.52 m measured from the ceiling. Gas temperatures were also measured 0.01 m off of the ceiling throughout the enclosure as shown in Figure 9. These thermocouples were placed 0.89 m, 1.93 m, 2.83 m, 3.74 m, 4.69 m, and 5.57 m from the closed end of the enclosure. Two thermocouples were located 0.89 m and 1.88 m from the far closed wall in the rear chamber of the enclosure as shown in Figure 9.

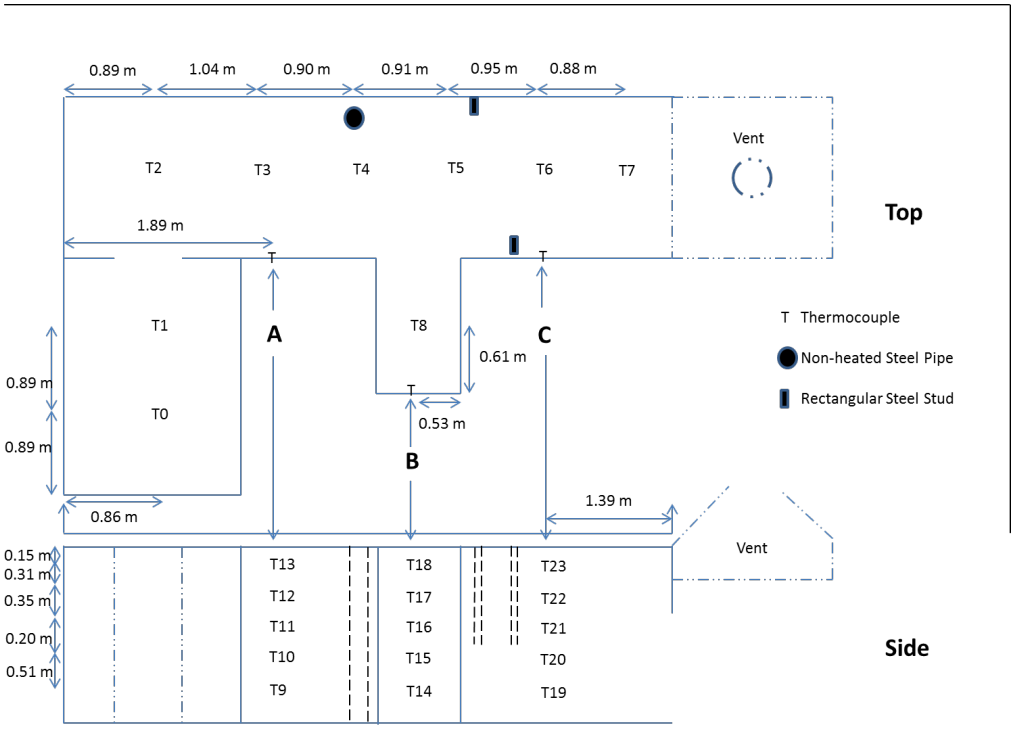

Figure 9. Thermocouple placement within the indoor enclosure

The visibility through the smoke was quantified through laser obscuration measurements with a laser shining across the width of hallway. This is similar to the smoke obscuration measurements recommended for other small and large-scale fire tests in ASTM E1354 [37] and ISO 9705 [38]. Two JDS 1108P red HeNe 0.5 mW lasers were used and the light intensity was measured with PDA36A Si photodiodes from Thorlabs. The photodiodes were set to a gain of 30 for all tests. Smoke obscuration measurements were performed at two locations along the hallway at an elevation of 1.49 m as shown in Figure 10.

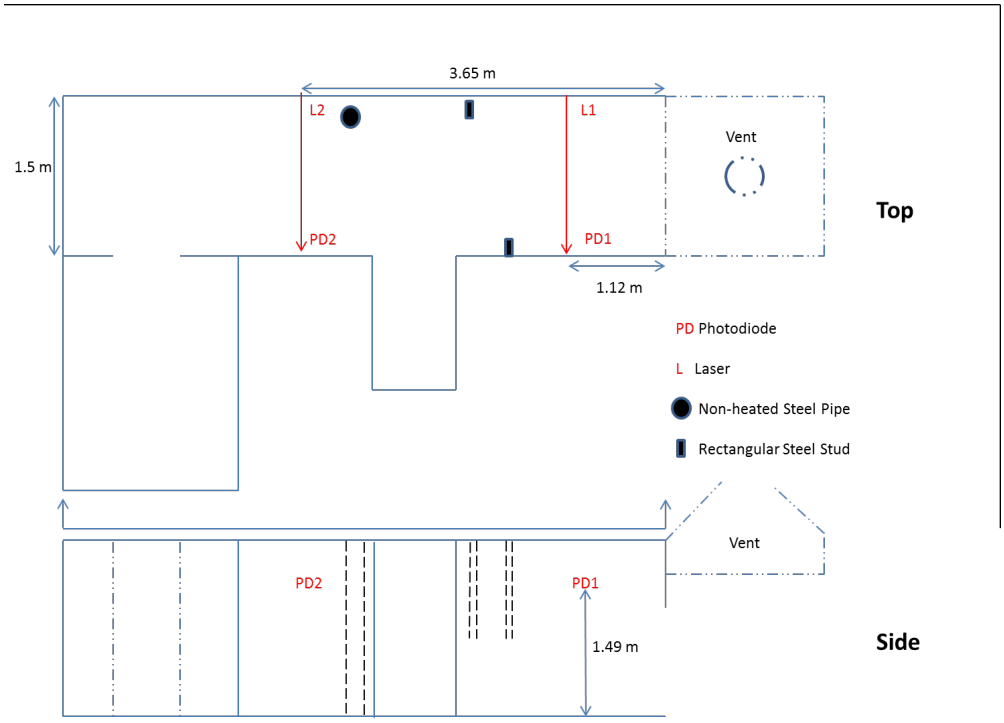

Figure 10. Laser and photodiode placement within the indoor enclosure for smoke obscuration measurements

Visibility through smoke by the human eye was determined by Equation 2 shown again below for convenience

$$V = \frac{C}{\sigma} \qquad \mathbf{2}$$

where V is visibility (m), C is an empirical constant, and σ is the extinction coefficient (1/m). According to the work done by Jin [39], the constant, C, should be 2-4 for light reflecting objects (i.e., walls). In this work, a constant of C=3 was used. The extinction coefficient was calculated using the values from the laser obscuration measurement in Equation 5 [39],

$$\sigma = \frac{1}{L}\ln\left(\frac{I_o}{I}\right) \qquad \mathbf{5}$$

where σ is the extinction coefficient (1/m), L is the smoke attenuated path length between the laser and photodiode (L=1.5 m), I_o is the baseline intensity of the laser

measured by the photodiode with no smoke (V), and I is the intensity of the laser measured by the photodiode with smoke at a specific time (V). The voltage measured when the photodiode was blocked was subtracted from both the baseline voltage and the measured voltage for a particular moment in time to find the appropriate intensity value.

Noise from the fan and blower used to ventilate the enclosure as well as the purge air used to keep the photodiodes clean from soot during each test was present at 17 Hz shown in Appendix A with FFT analysis of the intensity signal from the photodiodes. A low pass filter at 5 Hz and a moving average over every 5 seconds was placed on the data. An image of the impact of different moving average time steps on the visibility calculation is shown in Appendix A. There was low frequency noise present in the laser obscuration measurements from the photodiodes measuring the laser intensity and surrounding electronics in the test facility. Noise remaining in the system had a greater impact when I approached I_o due to the logarithmic nature of Equation 5.

The data from both the thermocouples and the photodiodes was acquired at 1 kHz using National Instruments LABVIEW and a National Instruments myDAQ using 9205 and 9213 boards with 16 bit resolution.

The final algorithm was intended for integration onto a humanoid robotic platform, but this was not available for testing. Therefore, sensors were mounted onto the stand shown in Figure 11 that could be placed within the test facility and indoor enclosure at fixed locations during a fire test. The stand was located at different positions along the expected robot navigation path to support fire location algorithm development and decision-making. Cameras were mounted below the smoke layer at 0.76 m above ground to prevent overheating and smoke accumulation on the cameras during testing. The UV sensors were also mounted onto the stand; however, their vertical position was varied to evaluate their

performance in low visibility smoke. As a result, UV sensors were mounted below the smoke layer (0.76 m) and immersed in the smoke layer (1.5 m).

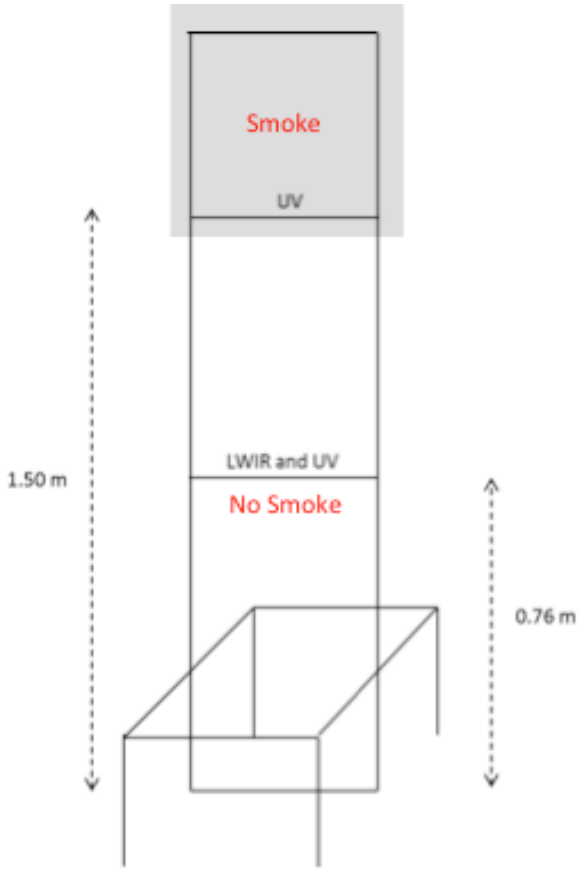

Figure 11. Sensor stand for algorithm development

2.3. Fire Conditions

There were two types of fuel used for the full scale fire testing. Each of these fuels created different temperature and visibility conditions in the enclosure. Latex foam was used as a low visibility fire type. Each latex foam fuel sample had a 0.27 m by 0.20 m rectangular cross section. The latex foam fuel sample was 0.18 m at the thickest point. The latex foam fire was allowed to burn until the smoke from the fire cleared. A 60 kW propane flame was used as a high visibility fire type. The propane fire was allowed to reach steady temperature before any position testing was performed. All LWIR images were taken at 100 seconds into the test

simulating a fully developed fire condition. Each propane flame was produced using a 0.30 m by 0.30 m sand burner. These two different types of fuels are shown in Figures 12 and 13, respectively. The position of the fire for each algorithm development test is shown below in Figure 14.

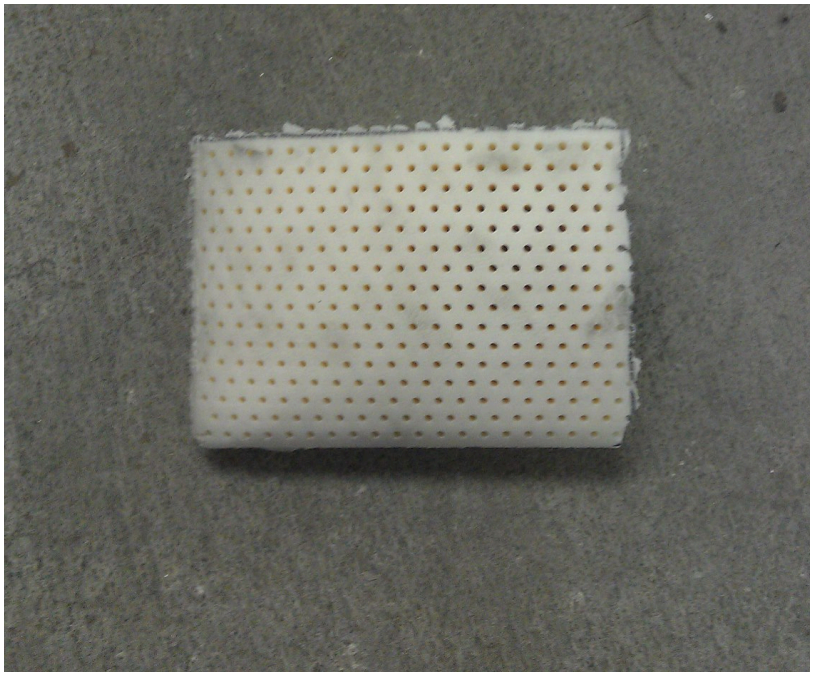

Figure 12. Image of latex foam fuel

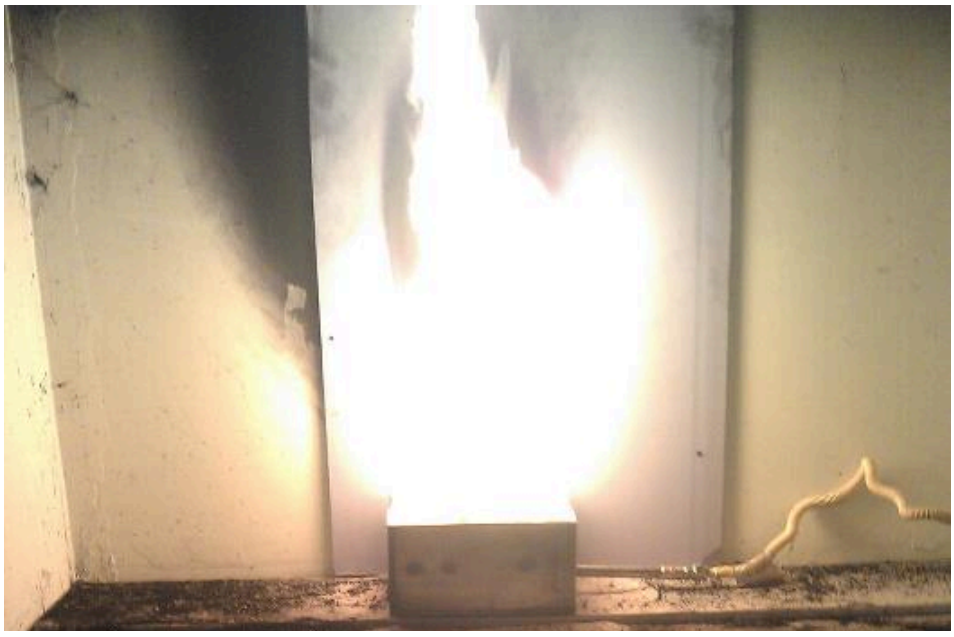

Figure 13. Propane flame and sand burner

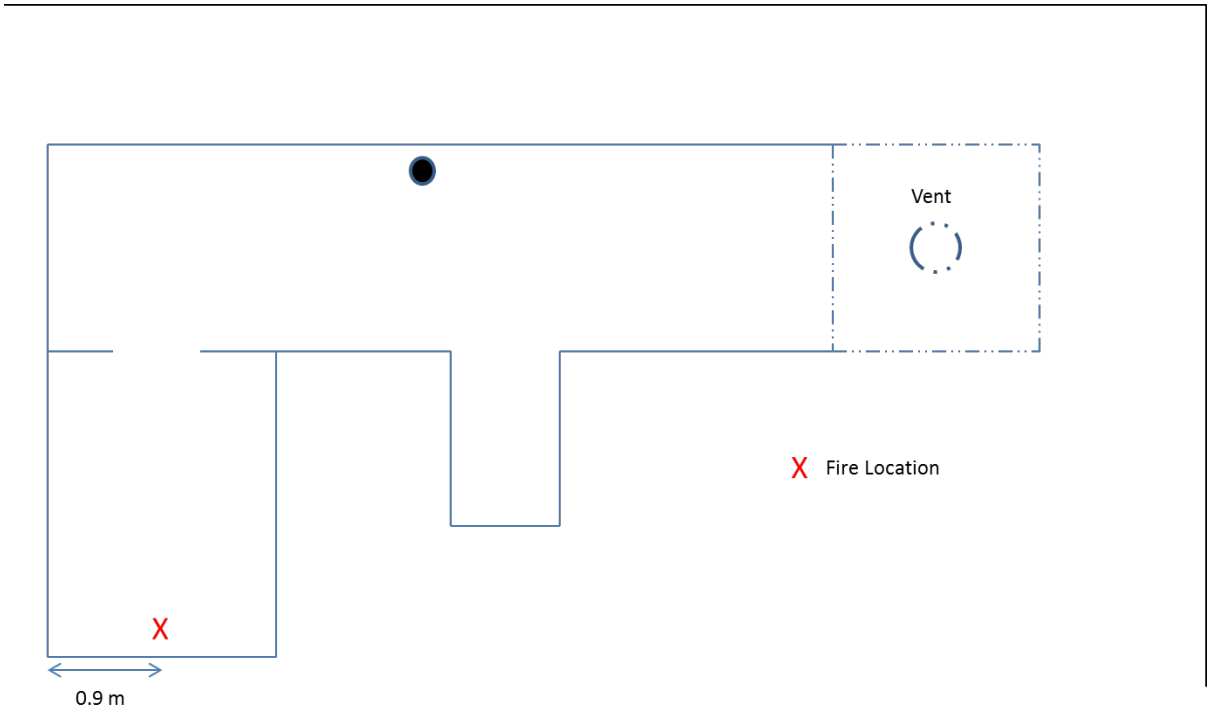

Figure 14. Example of fire location for algorithm testing

The gas temperature data for a latex foam fire is shown in Figure 15. The gas temperature data corresponds to the thermocouple placements shown in Figure 9. The temperature reached 160°C after 87 seconds at the ceiling thermocouple nearest to the fire. Higher gas temperatures at the ceiling correspond to those thermocouple locations closer to the room containing the fire. Similarly, higher gas temperatures along the wall correspond to those locations closer to the ceiling.

The visibility data for a latex foam fire is shown in Figure 16. The intensity values used to calculate the respective visibilities at each obscuration measurement location were processed with a 5 Hz low pass filter and a 5 second moving average. The visibility reaches a minimum value of 0.0 m at 85 seconds into the test.

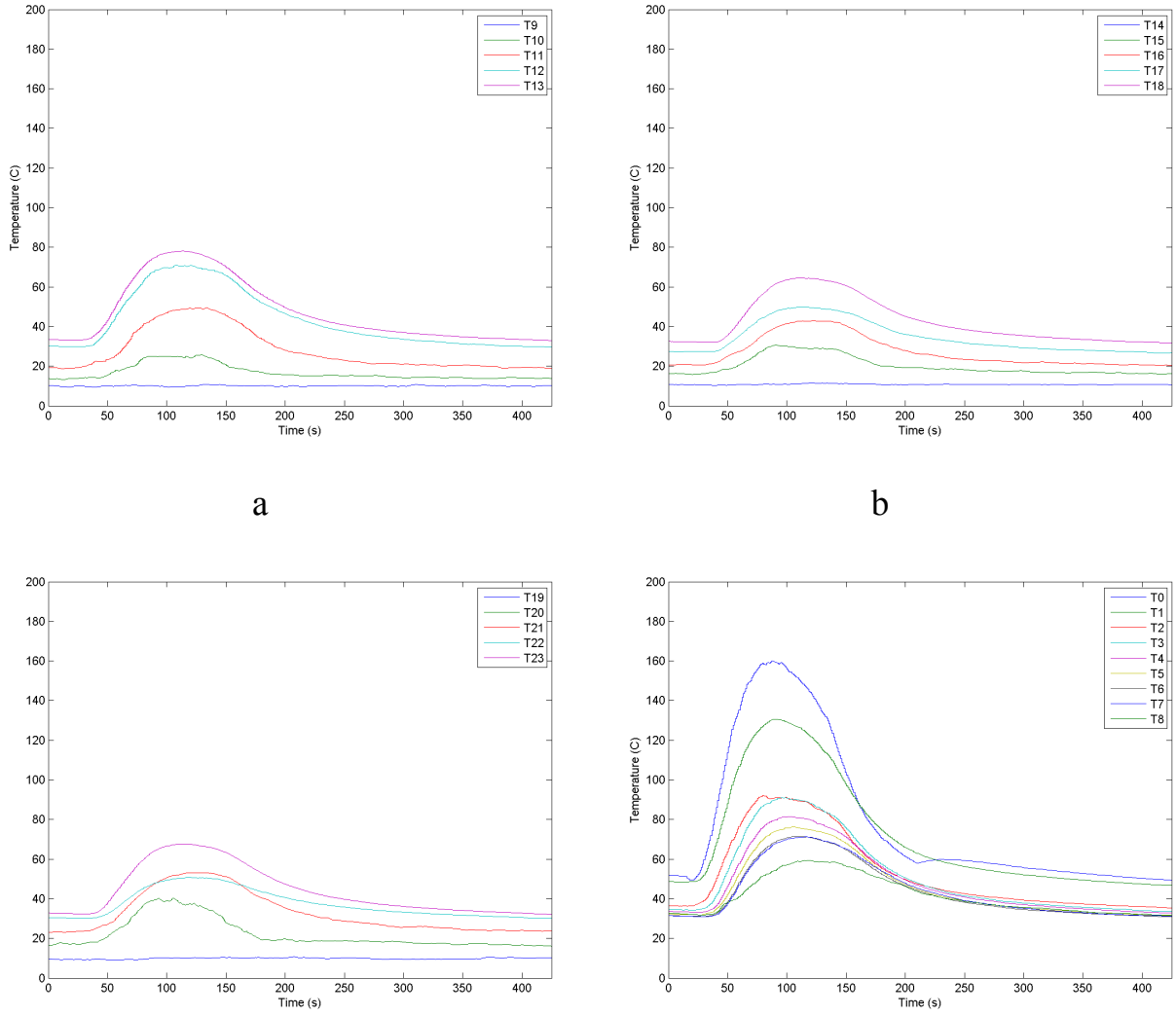

Figure 15. Gas temperatures during a latex foam fire. (a) Location A (b) Location B (c) Location C (d) along the ceiling

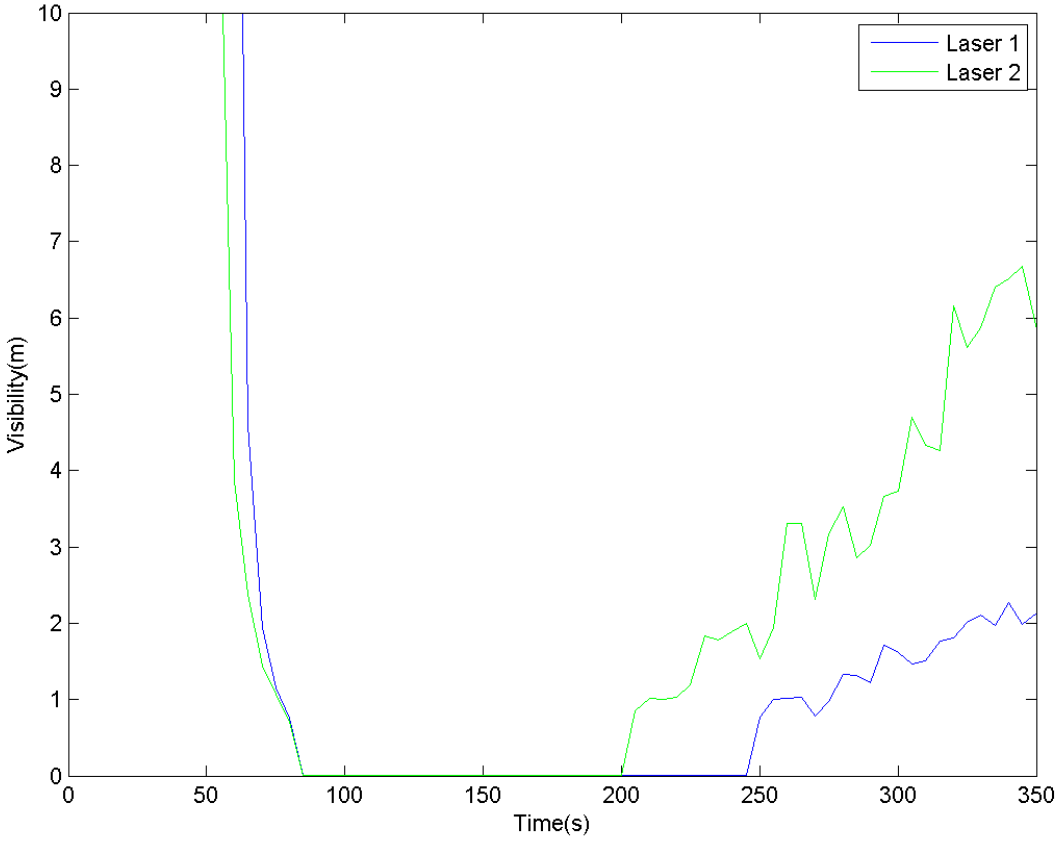

Figure 16. Visibility measurements during a latex foam fire test.

The gas temperature data for a 60 kW propane fire is shown in Figure 17. The maximum temperature reached was 178°C. The visibility throughout the propane test is shown in Figure 18. The visibility for a propane fire test remains above 30 m for all time for both obscuration measurement locations. The disparity between the two visibility levels corresponding to the two different obscuration measurement locations is in part attributed to the large impact of small noise values based on the logarithmic function used to calculate the extinction coefficient when I approached I_o.

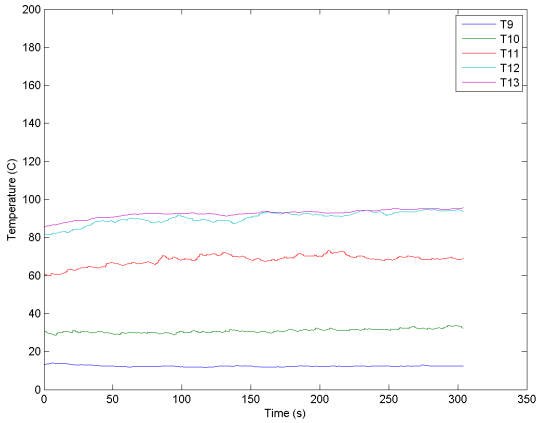

a

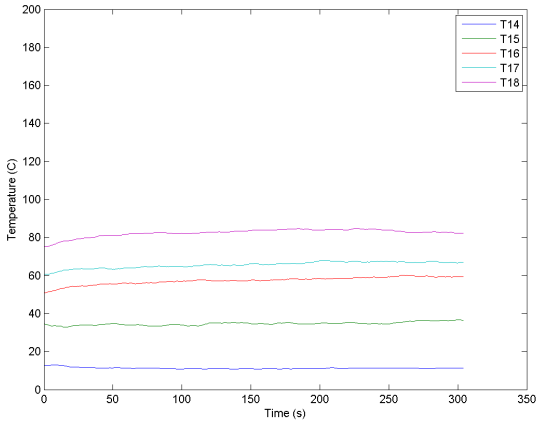

b

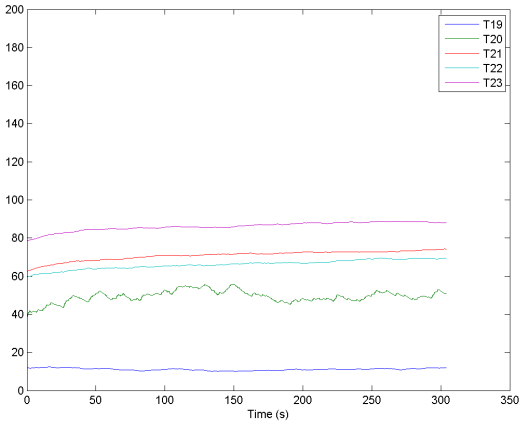

c

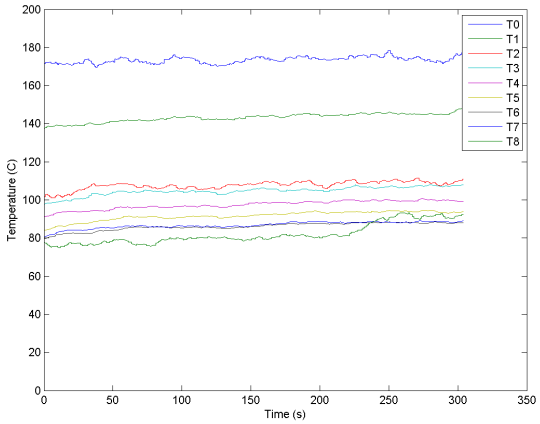

d

Figure 17. Gas temperatures during a 60 kW propane fire. (a) Location A (b) Location B (c) Location C (d) along the ceiling

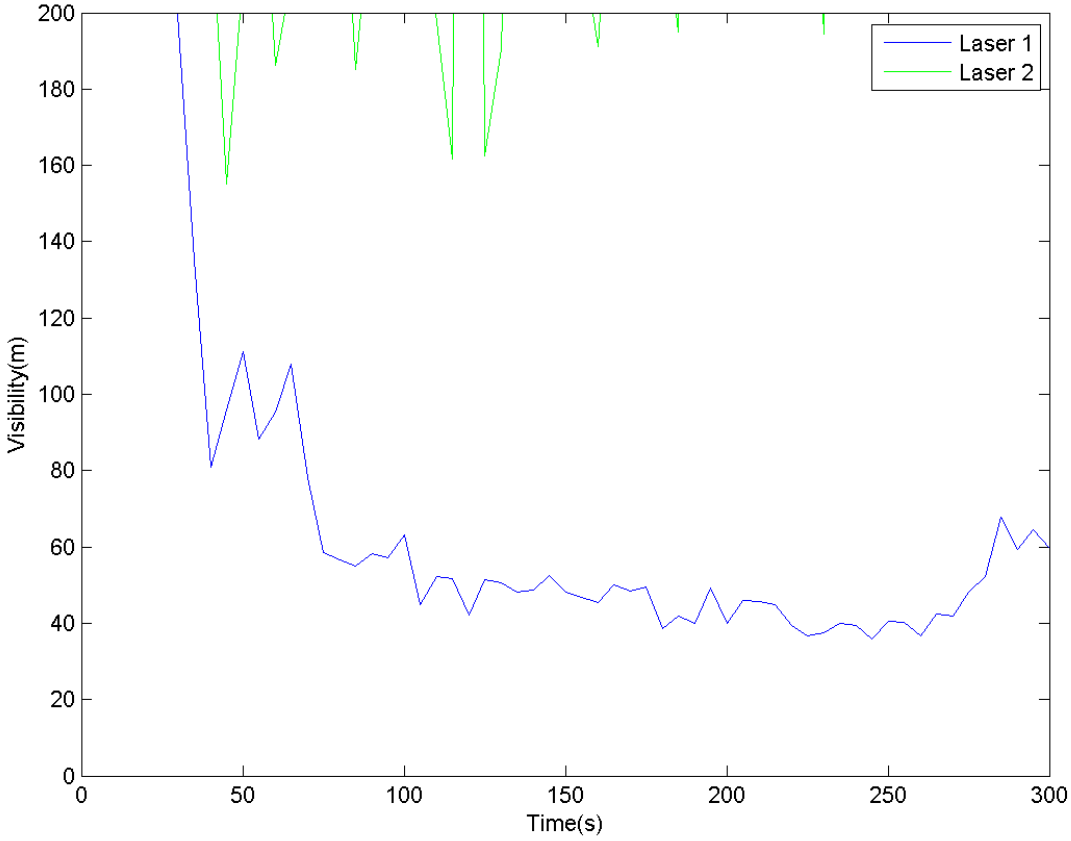

Figure 18. Visibility measurements during a 60 kW propane fire.

Chapter 3: Fire Location Algorithm by Radiation Emission (FLARE)

3.1 FLARE Overview

Radiation emission from the enclosure and the fire were determined to be the most effective way to guide the robot to the fire. A fire location algorithm by radiation emission (FLARE) was developed to use data from LWIR and UV sensors to make decisions on which direction to navigate and to discriminate between non-fire hot objects and fires. FLARE is shown in flowchart form below in Figure 19.

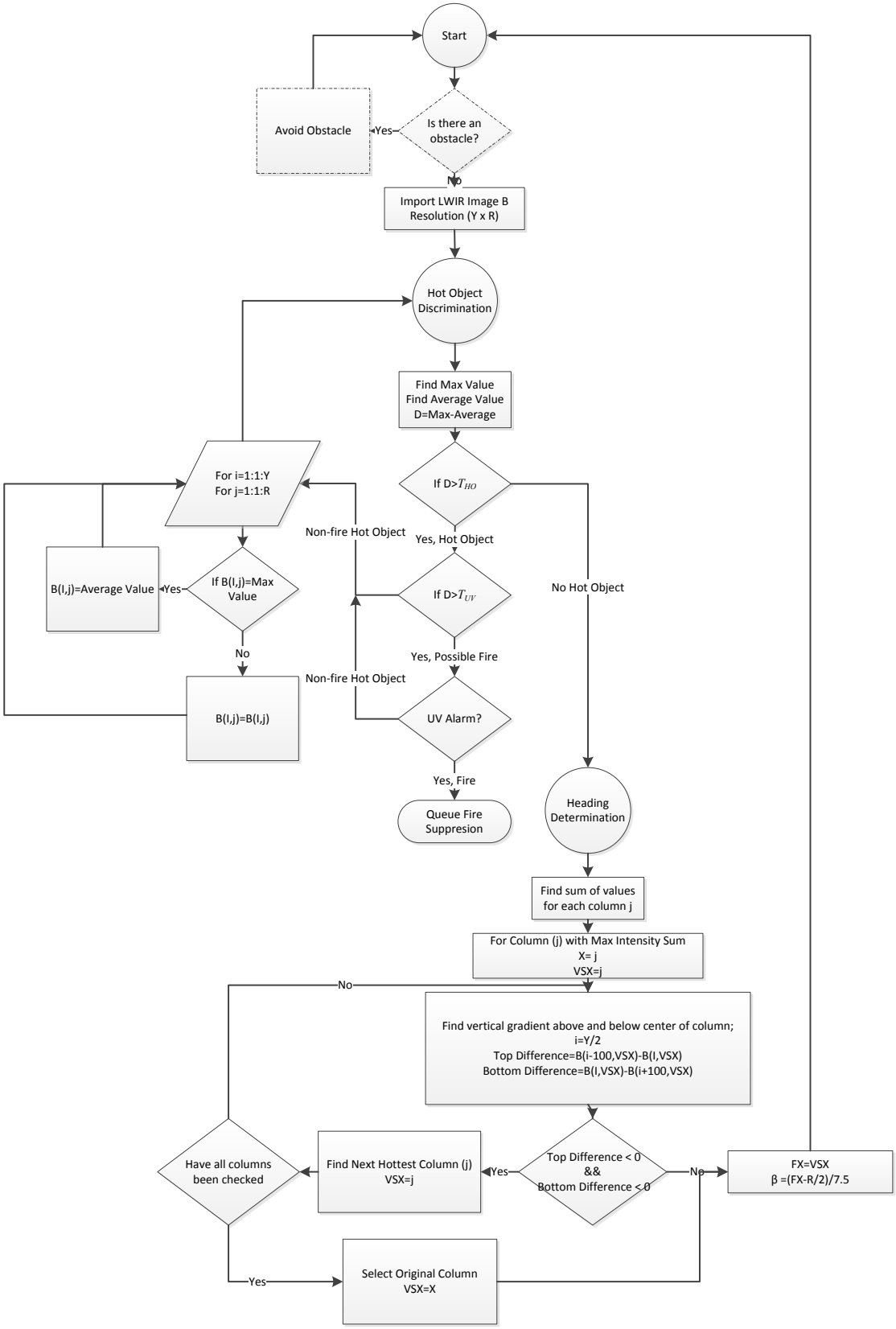

Figure 19. FLARE flowchart

FLARE takes LWIR images as an input and outputs a preferred heading angle for the robot to follow in order to reach the fire. FLARE is secondary to the obstacle avoidance and localization algorithms that are assumed components of an autonomous robot. FLARE does not begin until any obstacles that are present are avoided. Obstacle avoidance and localization methods are not addressed in this research. This portion of the algorithm is shown in Figure 20.

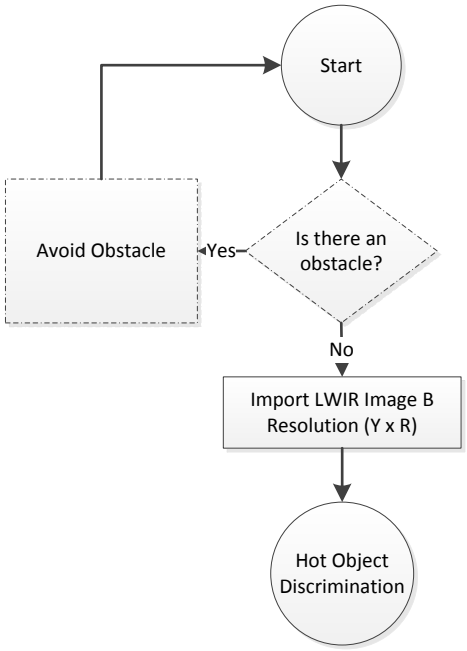

Figure 20. Initial steps of FLARE

After a LWIR image, B, is imported, the maximum and average values of the 14 bit raw intensities are calculated. Two thresholds, T_{HO} and T_{UV}, are experimentally set thresholds determined through different test scenarios for each LWIR camera type. The values of these thresholds used in these tests are shown in Table 2. The reason that the T_{UV} values differ between the two LWIR camera types is due to the dynamic range used by the camera to describe each respective scene. The FLIR A35 uses a larger range of intensity values to describe a given scene than the FLIR Tau 2-320. This is discussed further in Section 3.3.4.

Table 2. FLARE Thresholds

	FLIR Tau 2-320	**FLIR A35**
T_{HO}	650	650
T_{UV}	6900	10000

If the difference, D, between the maximum and the average intensity is greater than T_{HO} the LWIR camera field of view is believed to contain a hot object. If the difference is greater than T_{UV}, the UV sensor response is analyzed to check for an actual fire. Fire suppression is queued when a fire is detected.

A non-fire hot object is believed to be in the scene if the difference between the maximum and average intensities for the scene is greater than T_{HO} but less than T_{UV} or if the difference is greater than T_{UV} but no fire is detected with the UV sensor. Different test cases were created with non-fire hot objects placed off of the correct path to test the robustness of the algorithm.

FLARE ignores non-fire hot objects in order to provide a correct heading leading towards the fire location. These objects present a challenge to the FLARE algorithm if the fire is out of the field of view of the LWIR camera and UV sensor. FLARE directs towards the hottest coordinate as judged by LWIR intensities, and a non-fire hot object can misdirect the robot using this method depending on the object's size and location relative to the robot. Non-fire hot objects could be any variety of objects including but not limited to heated pipes, uncovered lights, or heaters. If a non-fire hot object is located in the field of view, it is excluded from the heading determination by replacing each pixel that has the maximum intensity value with the average intensity value. This allows FLARE to ignore the impact of the non-fire hot object, without completely ignoring that portion of the scene. This method also maintains the average LWIR intensity of the scene. This process is iteratively performed until the difference between the new maximum intensity and average intensity falls below T_{HO} discussed previously. An example of how non-

fire hot object discrimination using this method changes the LWIR scene considered by FLARE is shown in Appendix B. The non-fire hot object discrimination portion of FLARE is shown below in Figure 21.

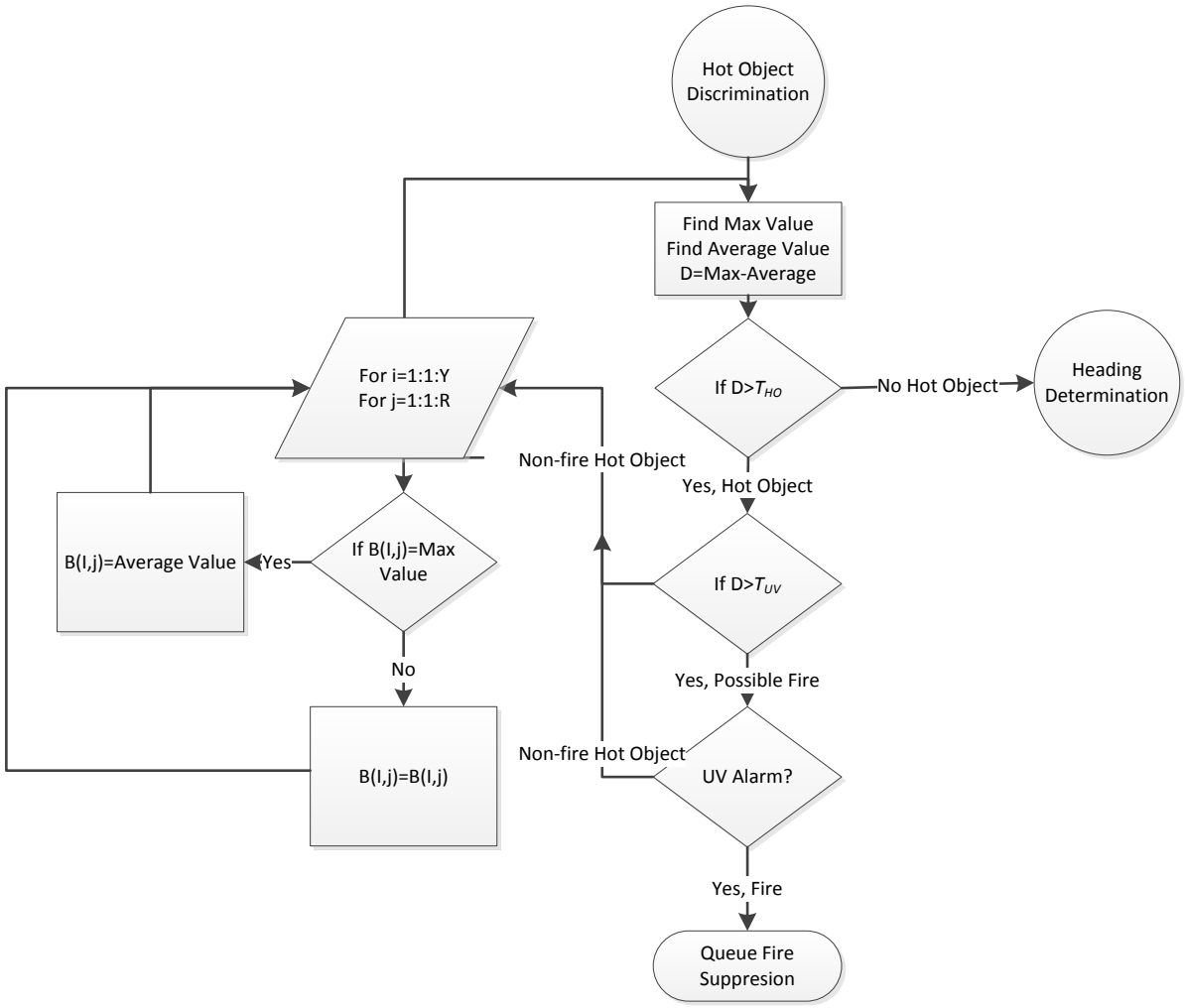

Figure 21. Non-fire hot object discrimination portion of FLARE

UV response is the definitive check as to whether or not a fire is in the scene provided that the difference between the maximum and average relative intensities in the LWIR image is greater than $T_{UV.}$ As mentioned in Chapter 1, UV sensors in the Far UV and UV C wavelength ranges like the UVTRON R9454 have few false alarms. UV reflections off the walls of an indoor enclosure can cause the fire to be detected prematurely. This would stop the robot and queue suppression before the fire is in view.

A test was designed to show the impact of the UV reflection problem for different fire sizes. The test set up within the facility is shown below in Figure 22. A propane flame was started in the position designated by the red X. The flame was started at 25 kW and after 30 seconds increased to 60 kW. The UV sensor was placed 1.83 m from the opening to the chamber where the fire was located out of view.

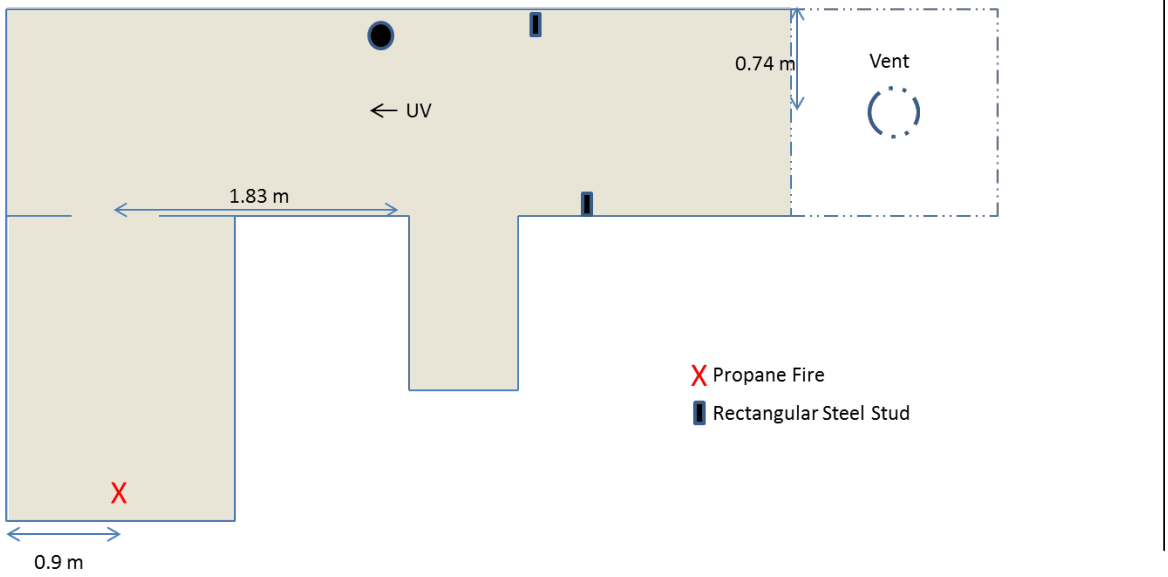

Figure 22. Test set up for UV reflection test

The results in Figure 23 show that UV reflections off of walls within an indoor enclosure can be detected as a fire for larger flames like a 60 kW propane fire from at least 1.8 m away. The maximum number of peaks in a second corresponding to the maximum UV radiation strength during this test was 13 peaks in one second at 101 seconds into the test. This value is well above the 5 peaks a second threshold which alarms FLARE to the presence of a fire. The strength of UV reflections depends on the size of the fire as well as the color and texture of the wall surfaces within the enclosure.

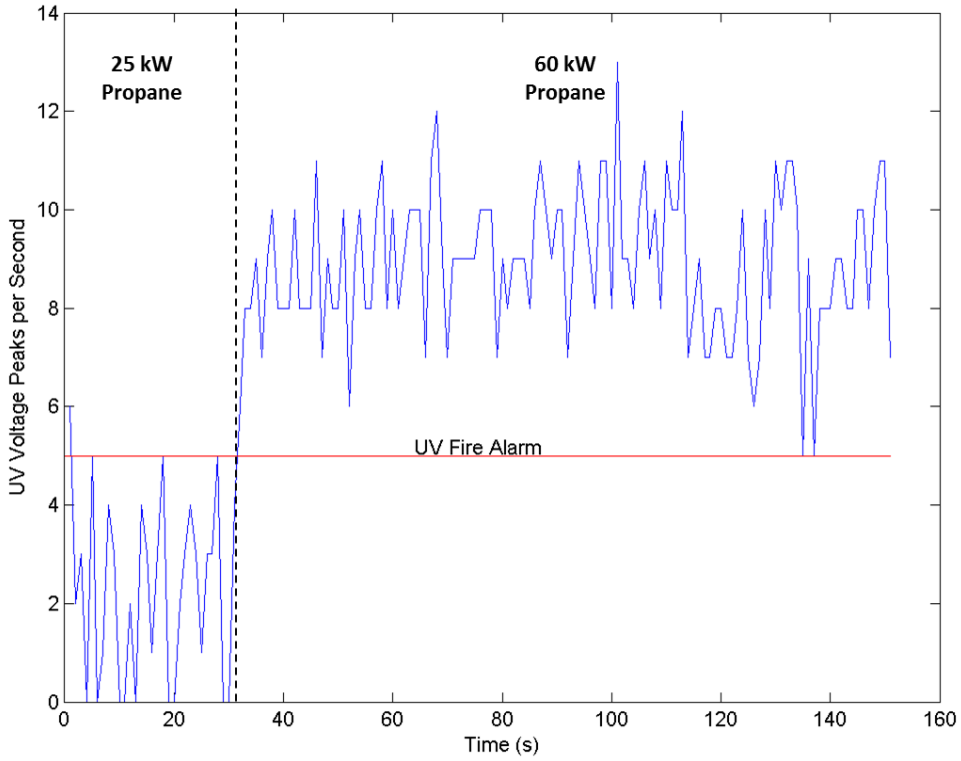

Figure 23. UV peaks per second observed during UV reflection test

FLARE avoids the potential error of stopping due to UV reflections by checking the UV after first examining the LWIR image to determine whether a fire is expected in the field of view. The UV alarm logic that is referenced in the discussion above and Figure 21 is shown in Figure 24 below.

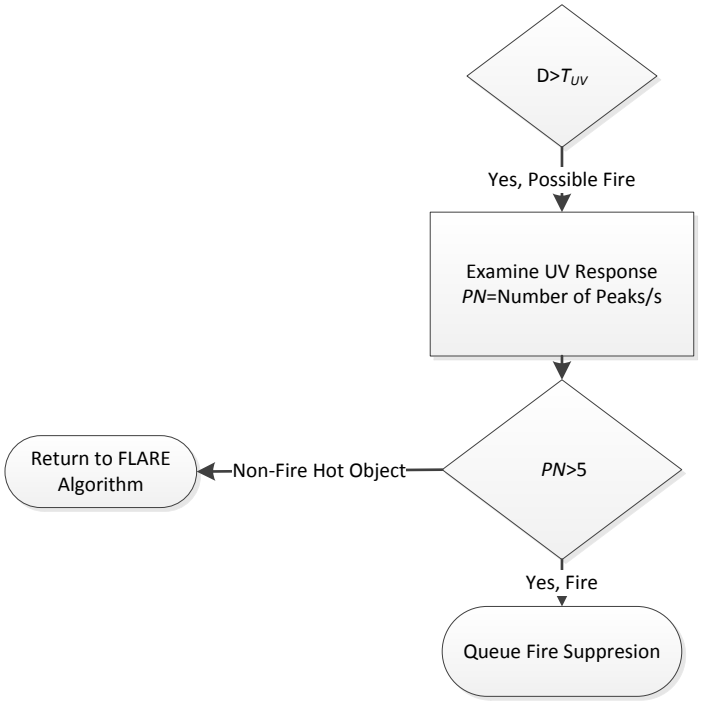

Figure 24. UV alarm component of FLARE

After the scene is examined for potential hot objects of interest, each column of intensities for the image is summed. Temperatures naturally increase as the distance to the fire location decreases. As a first approximation, FLARE chooses the hottest direction as a heading, which corresponds to the horizontal pixel column with the highest intensity sum.

Combustion product gases that result from a fire naturally rise to the ceiling. This produces a temperature gradient which increases with height. The original coordinate corresponding to the highest column sum is checked for acceptable vertical thermal behavior. The middle pixel of the chosen column is used as starting location. The middle pixel can be found by dividing the vertical component of the LWIR camera resolution by 2. The intensity difference from subtracting the middle pixel intensity from an intensity 100 pixels above the middle pixel for the chosen column should be greater than 0 if temperatures are decreasing from the ceiling to the floor. Similarly subtracting an intensity 100

pixels below the middle pixel from the middle intensity value for the column should be greater than 0 if the natural temperature behavior discussed previously is observed. The coordinate is accepted if the two conditions are met. Otherwise, the coordinate is rejected and the original search for a new coordinate corresponding to the next hottest column is performed after discarding the coordinate previously checked from consideration. If all the columns are rejected and do not obey the natural vertical temperature behavior, the original coordinate corresponding to the original hottest column is chosen as the target coordinate.

The final pixel coordinate (FX) is found after a hot column with an acceptable vertical profile was discovered. This coordinate is then converted to a heading angle for the robot with Equation 6,

$$\beta = \frac{FX - \frac{R}{2}}{7.5} \qquad \textbf{6}$$

where β is the heading angle, R is the horizontal resolution of the LWIR camera, and 7.5 is a constant derived because of the 48° field of view of the LWIR cameras. FLARE continues to iterate until the fire is located. This heading determination portion of FLARE is shown below in Figure 25.

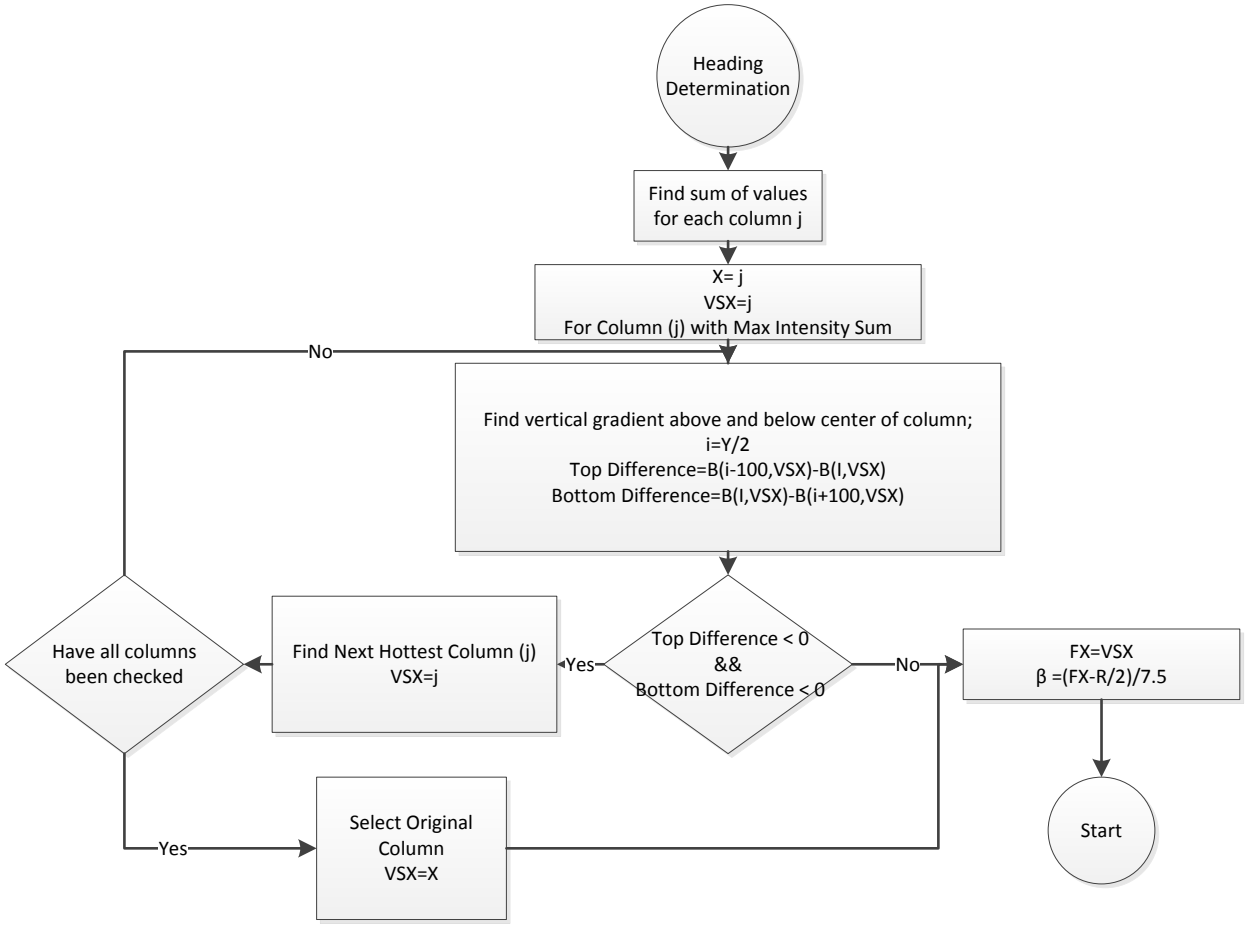

Figure 25. Heading determination portion of FLARE

3.2. FLARE Testing

FLARE should be used at any time when an autonomous firefighting robot is alarmed to a potential fire scenario. FLARE was tested with challenging navigation scenarios including multiple fire types, non-fire hot objects, and different potential robot positions. The first scenario contained a fire outside of the view of the robot. The second scenario was a fire outside of the view of the robot with non-fire hot objects located in various locations between the robot and the fire source. The enclosure contained both steel stud columns and drywall. All scenarios were tested using propane and latex foam fuel types. The sensors were placed in different positions within the test facility designated by A, B, C, D, and E

in Figure 26. The images from Positions A, B, C, D, and E with no fire in the enclosure are shown below in Figure 27.

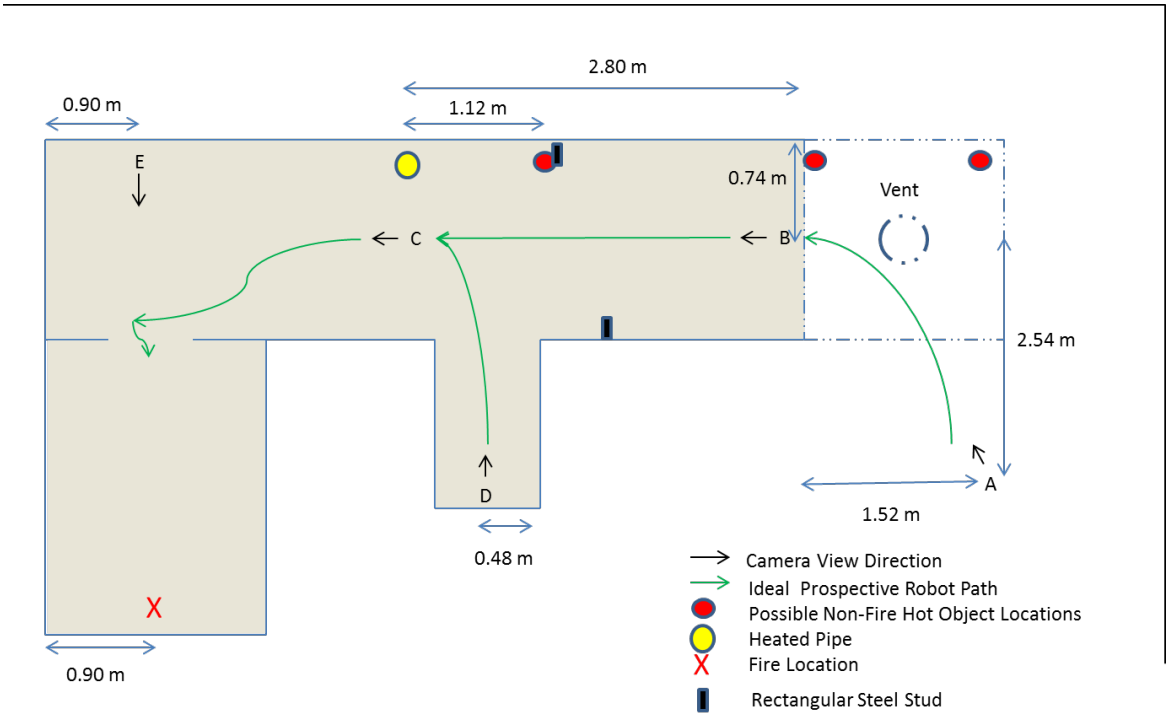

Figure 26. LWIR camera positions and test layout for FLARE testing

A

B

C

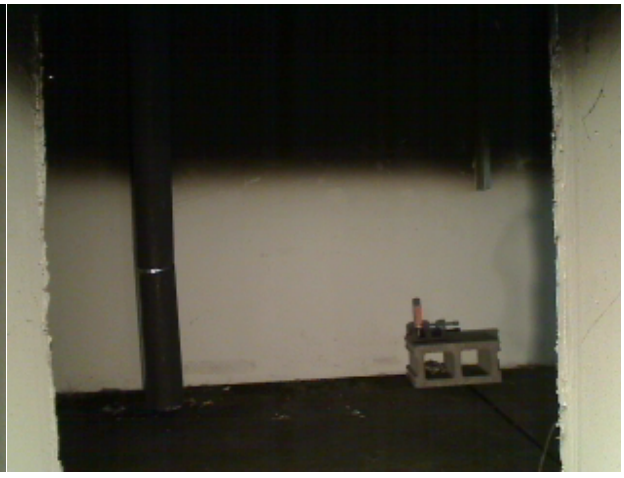

D

E

Figure 27. Visible images from LWIR camera Positions A, B, C, D, and E.

A LWIR camera image for both the FLIR Tau 2-320 and FLIR A35 LWIR cameras was taken 100 seconds into the burn. This allowed the thermal environment to become fully developed. These LWIR images were used to evaluate the algorithm for each test. While this data represents the conditions of a fully developed fire scenario, inspection showed that the FLARE output heading remains relatively constant with only minor fluctuation throughout the burn for both fuel types and all test scenarios as shown in Appendix C for the FLIR A35. The FLIR A35 images were chosen to display the results for each tested scenario. The FLIR A35 was favored as the LWIR camera for integration onto a potential robot platform because it could transfer data over an Ethernet connection and the larger dynamic pixel range it used to describe the test scenes. The data which shows the dynamic range used to describe each test scenario is shown in Section 3.3.4.

3.3 FLARE Testing Results

3.3.1. Fire Not In View

The first FLARE test used the basic example of a fire outside direct view within the indoor enclosure. The test layout for this scenario is shown in Figure 28. The green arrow designates the intended path for the robot to follow through the enclosure to locate the fire.

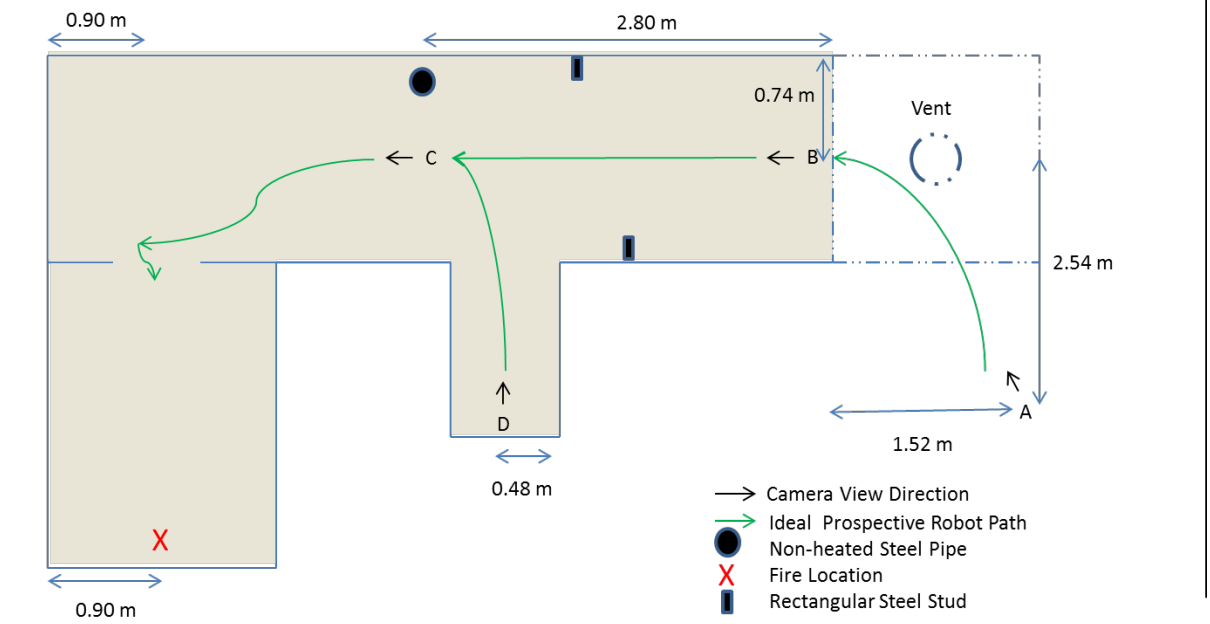

Figure 28: Test layout for basic fire not in view FLARE scenario

The LWIR cameras were first placed in Position A. The steel pipe located in this scenario was not heated. The results for Position A are shown in Figure 29 for the latex foam and propane fuel types using the FLIR A35 result image. The red line in each result image designates the output coordinate from FLARE. The orange arrow in each result image designates the direction to the fire. It was clear that the chosen coordinate led into the entrance to the enclosure, which was the direction towards the fire.

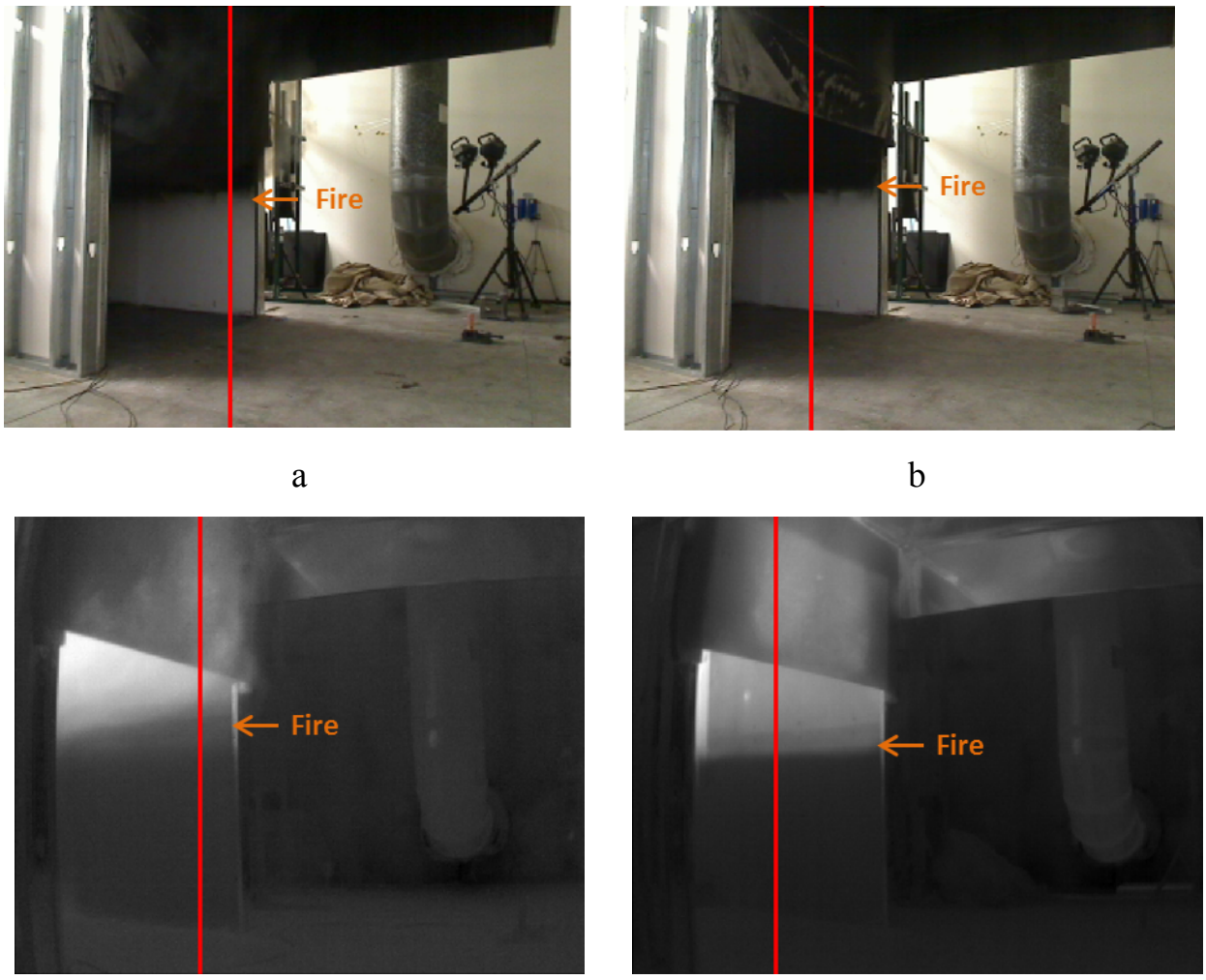

a b

c d

Figure 29. FLARE basic scenario Position A results. Results shown for (a) visible camera during latex foam test, (b) visible camera during propane test, (c) FLIR A35 during latex foam test, and (d) FLIR A35 during propane test

The results for this basic scenario are shown for Position B in Figure 30 below using the FLIR A35 result image. A small error is shown in Figure 30d for Position B during the propane test. FLARE's conclusion to choose the target coordinate as the right corner in the back of the hallway across from the chamber containing the fire shown in Figure 30d was a minor error. This was a result of combustion product that impinged on the upper part of the wall across from the

chamber as they exited the doorway and recirculated into the hallway. This thermal behavior caused the intensities to be higher on the wall across from the doorway than on the area surrounding the doorway. This type of error is not a problem for FLARE. As a robot would move from Position B through C towards E, more of the chamber containing the fire would become visible and the heading plan would change accordingly. The coordinate chosen for the latex foam test displayed in Figure 30a and Figure 30c is correct and leads toward the fire. This conclusion is supported by the results from Position C shown in Figure 31.

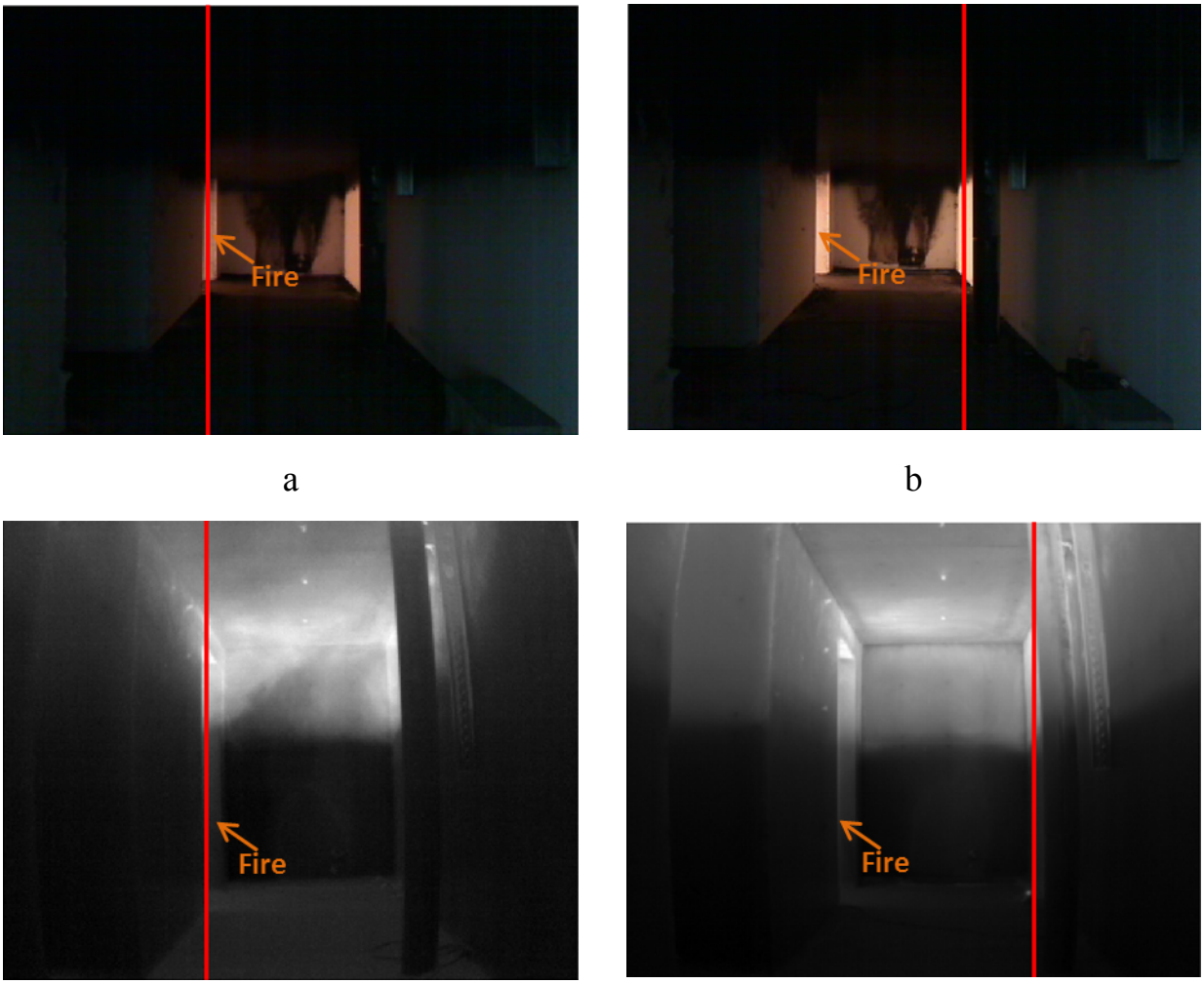

a b

c d

Figure 30. FLARE basic scenario Position B results. Results shown for (a) visible camera during latex foam test, (b) visible camera during propane test, (c) FLIR A35 during latex foam test, and (d) FLIR A35 during propane test

The FLARE coordinate results shown for the FLIR A35 in LWIR camera Position C in Figure 31 are correct and lead toward the fire. The results in Figure 31 show that as a robot moves towards the chamber containing the fire, minor errors like that shown in Figure 30d become inconsequential for the basic scenario described in Figure 28.

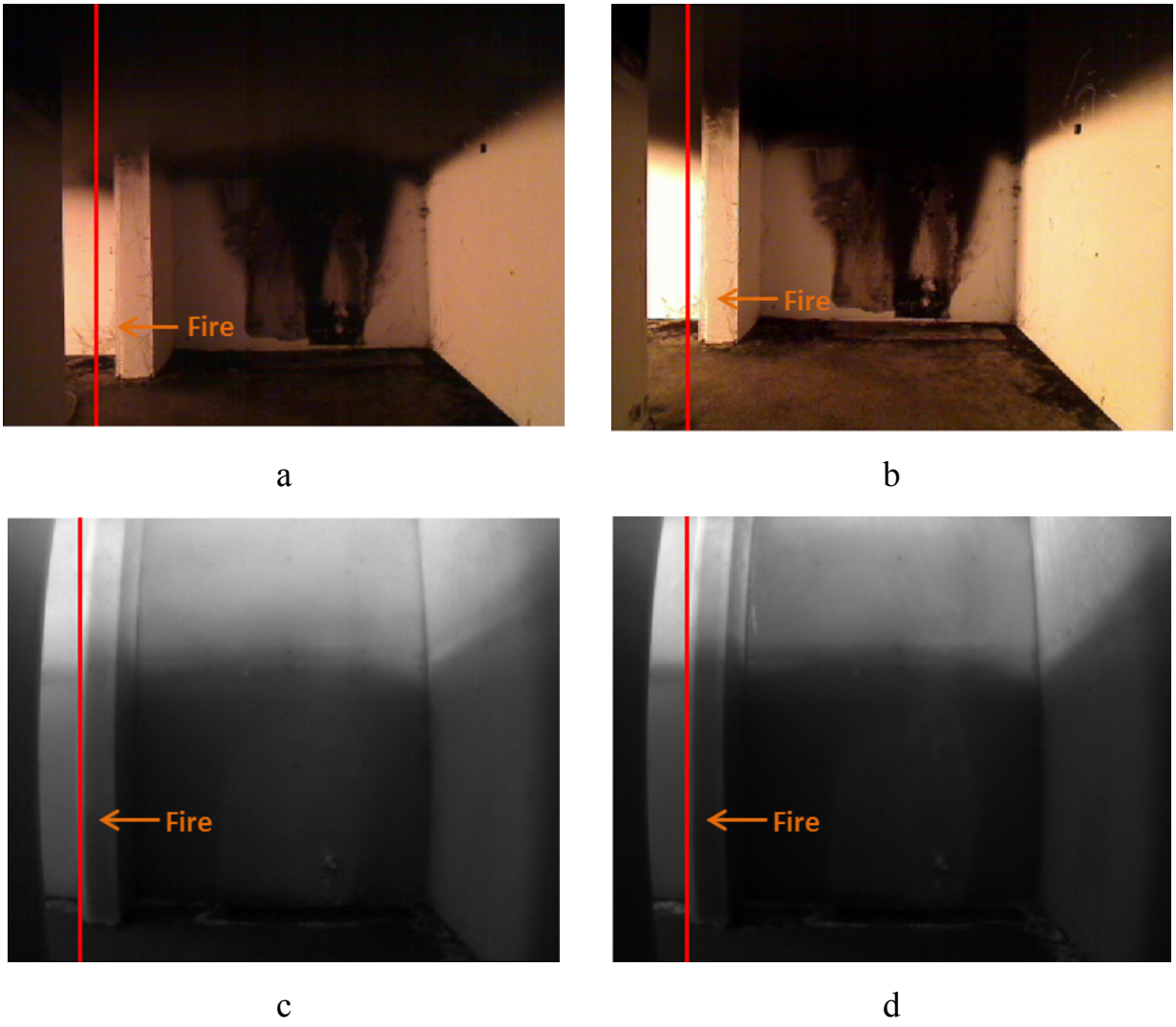

a b

c d

Figure 31. FLARE basic scenario Position C results. Results shown for (a) visible camera during latex foam test, (b) visible camera during propane test, (c) FLIR A35 during latex foam test, and (d) FLIR A35 during propane test

LWIR Position D was also tested for this scenario. This placed the prospective robot start location in the fire enclosure at Position D, as opposed to Position A located outside of the fire environment. The results for this test at Position D are shown below in Figure 32 using the FLIR A35 image. The results of the FLARE algorithm for Position D during the basic fire scenario shown in

Figure 32 are correct. All FLARE output coordinates shown provide a heading to the left of the center of the image frame looking out from Position D. This would result in the robot exiting the area containing Position D and turning left towards the chamber containing the fire.

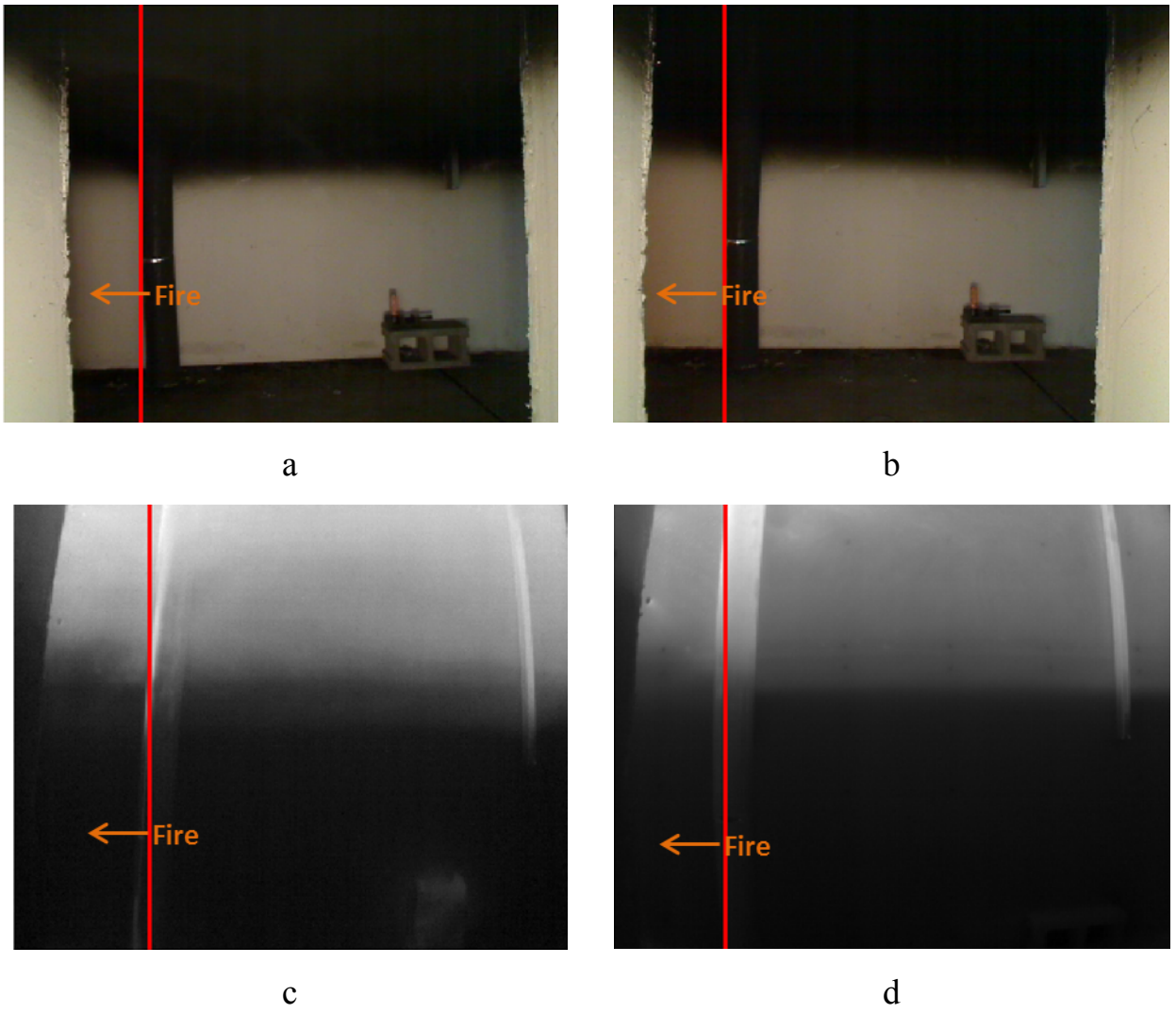

a b

c d

Figure 32. FLARE basic scenario Position D results. Results shown for (a) visible camera during latex foam test, (b) visible camera during propane test, (c) FLIR A35 during latex foam test, and (d) FLIR A35 during propane test

3.3.2 Non-fire Hot Object Discrimination-Heated Pipe

FLARE provided the correct heading for all FLIR A35 camera positions in the basic scenario with a fire placed outside of the camera field of view. A more complicated series of scenarios were introduced to test the robustness of FLARE. The fire location remained the same for all the tests. Both latex foam and propane fuels were used. Non-fire hot objects at a higher temperature than the rest of the scene were introduced by heating a steel pipe. Non-fire hot objects are denoted in the results with a yellow arrow. The direction to the fire is designated with an orange arrow. The first non-fire hot object test used a heated steel pipe in the view of LWIR camera Positions B and D. This test layout is shown in Figure 33.

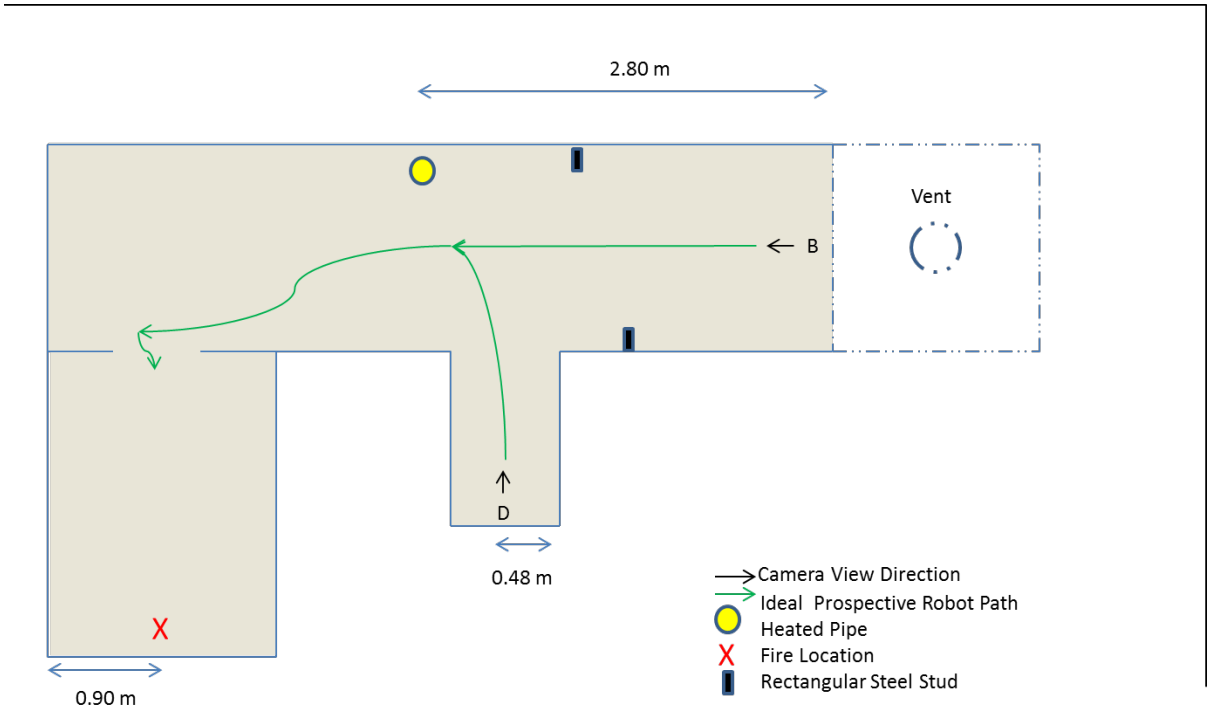

Figure 33. Heated pipe FLARE non-fire hot object discrimination test layout

The FLARE results for the FLIR A35 camera in Position B looking down the hallway with the heated steel pipe in the scene are shown in Figure 34. The heated pipe is not as obvious in Figure 34d compared to Figure 34c because the temperatures for the propane test are higher relative to that of latex foam. The

heated pipe did not stand out as much thermally for the propane test as shown by the drop in contrast between the two FLIR A35 LWIR images. The FLARE output coordinate shown in Figure 34 for both the latex foam and propane fuel types was correct because it selected the entrance of the chamber containing the fire.

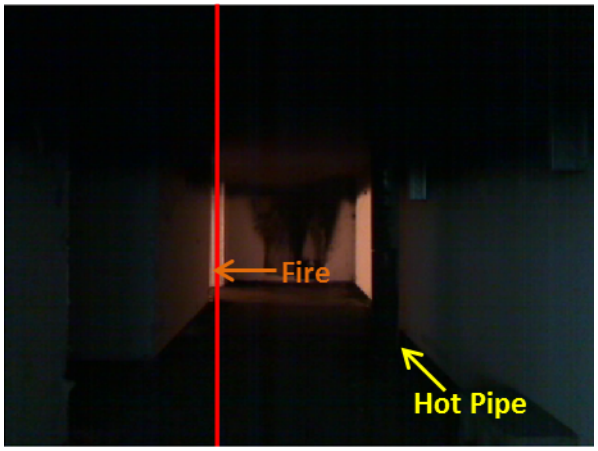

a

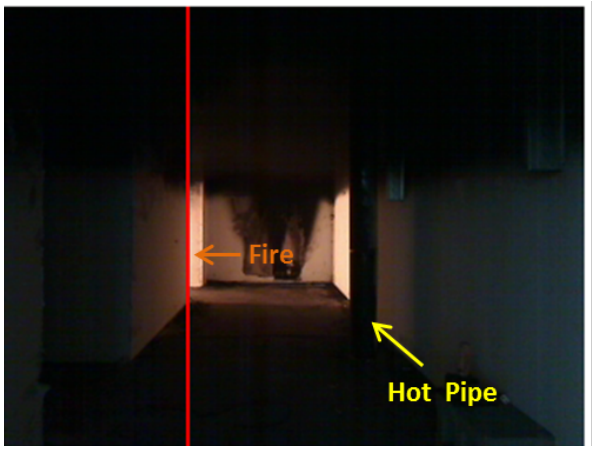

b

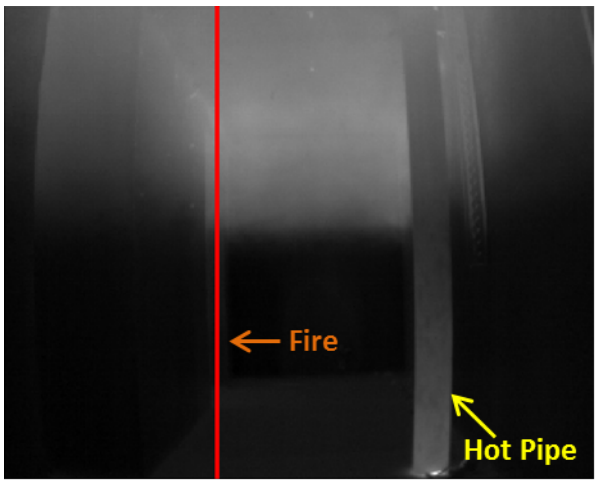

c

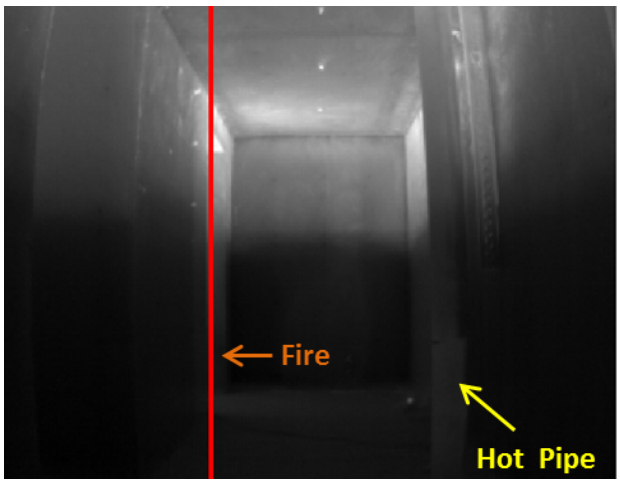

d

Figure 34. LWIR camera Position B for FLARE non-fire hot object scenario with heated pipe; results shown for (a) visible camera during latex foam test, (b) visible camera during propane test, (c) FLIR A35 during latex foam test, and (d) FLIR A35 during propane test

Figure 35 contains the same heated pipe non-fire hot object but with results from Position D with the FLIR A35 test images from each fuel type scenario. Any FLARE output heading to the left of the center of the image was considered successful. The results for LWIR camera Position D with a heated hot pipe located in the view of the robot were correct. FLARE selected a heading that would allow a robot to exit Position D and turn left into the hallway towards the fire location.

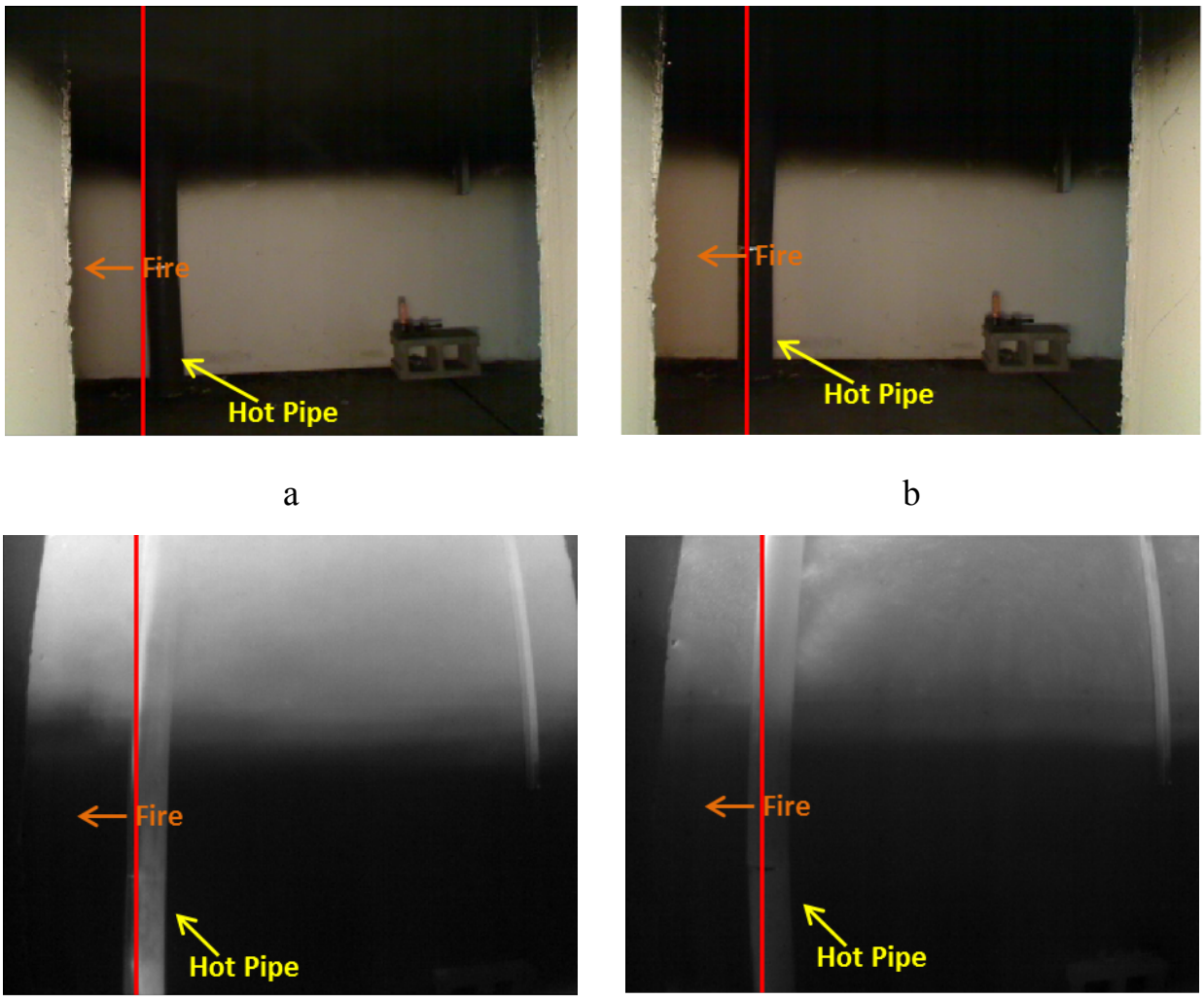

Figure 35. LWIR camera Position D for FLARE non-fire hot object scenario with heated pipe; results shown for (a) visible camera during latex foam test, (b) visible camera during propane test, (c) FLIR A35 during latex foam test, and (d) FLIR A35 during propane test

3.3.3 Non-Fire Hot Object Discrimination-Heater

A small enclosure heater that reached temperatures over 100°C was used in different locations to further test the robustness of FLARE. The first heater scenario test layout is shown in Figure 36. The heater is placed within the field of view of LWIR camera Position A off of the correct heading. An example of the potential robot path from Position A into the enclosure is designated by the green arrow in Figure 36.

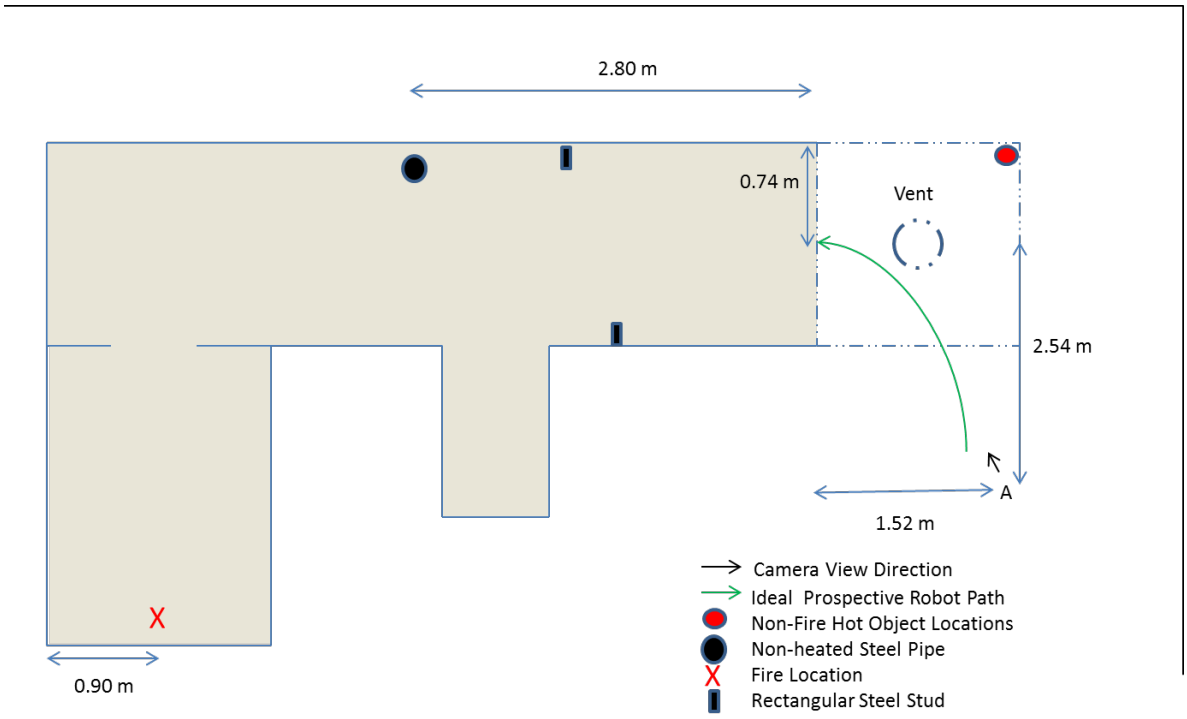

Figure 36. FLARE non-fire hot object discrimination with heater in view of LWIR camera Position A test layout

The results for LWIR camera Position A with the heater in view are shown below in Figure 37 using the FLIR A35 images. This result showed that FLARE can properly discriminate against non-fire hot objects significantly hotter than the rest of the scene. The correct heading coordinates for LWIR camera Position A were between 35 and 148 for the FLIR A35 based on the results for the basic scenario given in Figure 28. This is also supported by the visible camera images

shown in Figure 37a and Figure 37b for latex foam and propane tests respectively. The FLARE output coordinates using the FLIR A35 were 84 for the latex foam test and 83 for the propane test respectively. The contrast of LWIR image is very low because of the relative intensity of the heater in comparison to the rest of the scene for the FLIR A35.

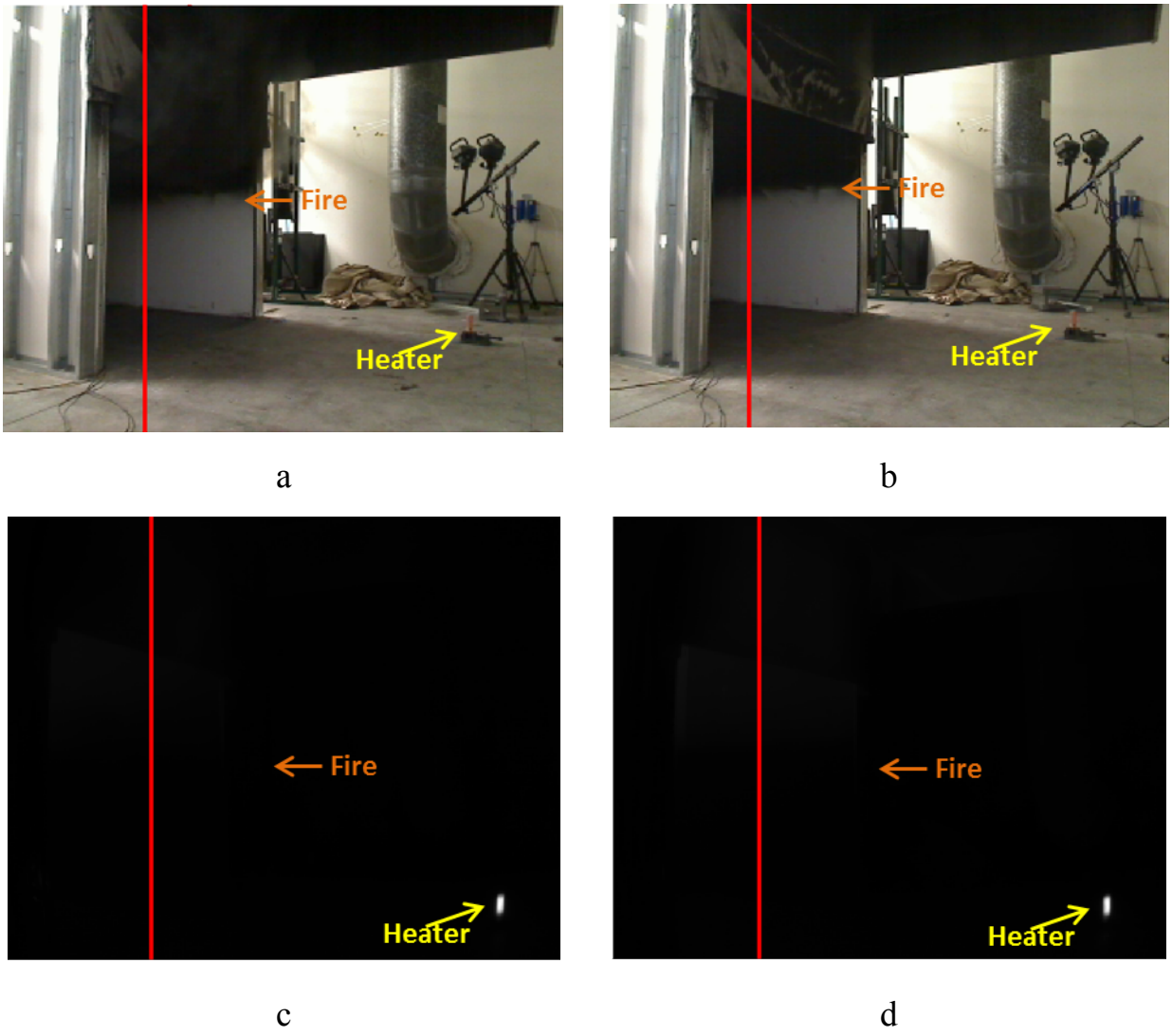

Figure 37. LWIR camera Position A for FLARE non-fire hot object scenario with heater; results shown for (a) visible camera during latex foam test, (b) visible camera during propane test, (c) FLIR A35 during latex foam test, and (d) FLIR A35 during propane test

The next scenario was tested by moving the heater closer to the entrance to the enclosure. The scene was observed from LWIR camera Position A. This test served to prove that non-fire hot object discrimination would not cause FLARE to miss the intended heading. The layout for this test is shown in Figure 38.

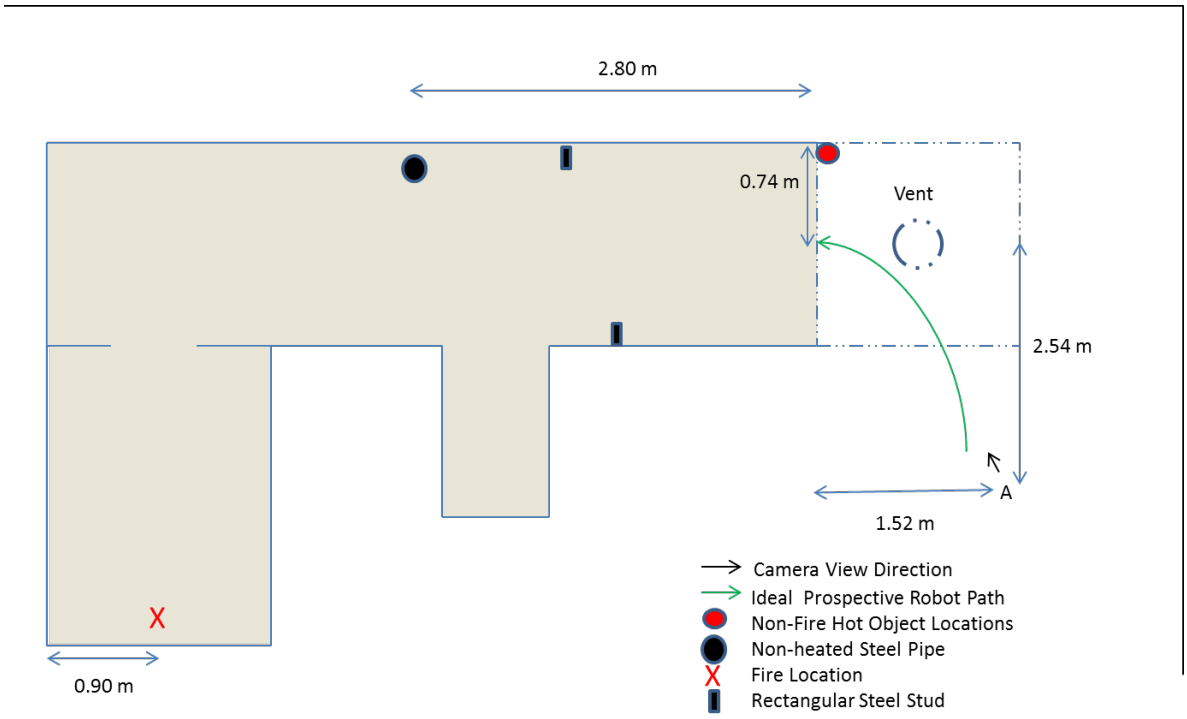

Figure 38. FLARE non-fire hot object discrimination with heater near heading at LWIR camera Position A test layout

The results from the FLIR A35 for this scenario are shown in Figure 39. Similar to the previous test, the correct coordinates were shown to be between 35 and 148. The FLARE output coordinates for the FLIR A35 shown in Figure 39 were 84 and 86 for latex foam and propane respectively. The FLARE results at LWIR camera Position A all led into the hallway entrance towards the location of the fire regardless of the heater.

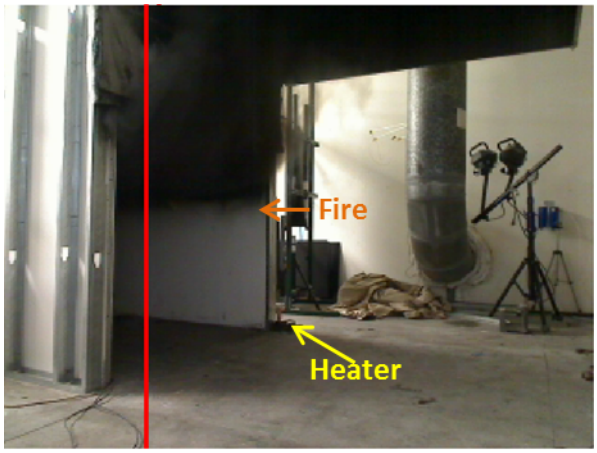

a

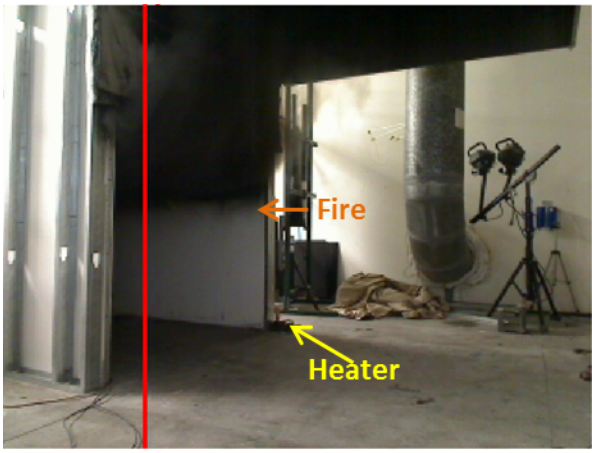

b

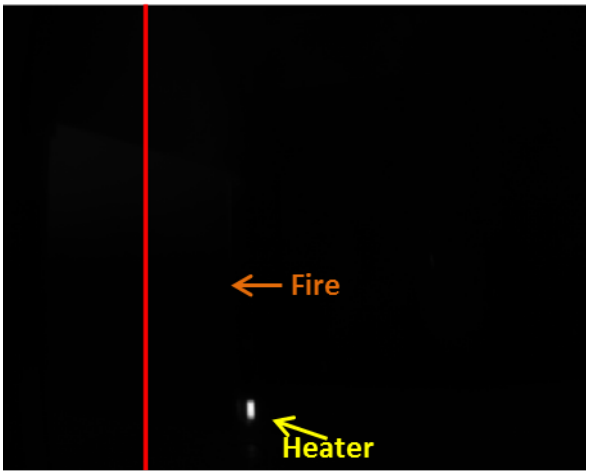

c

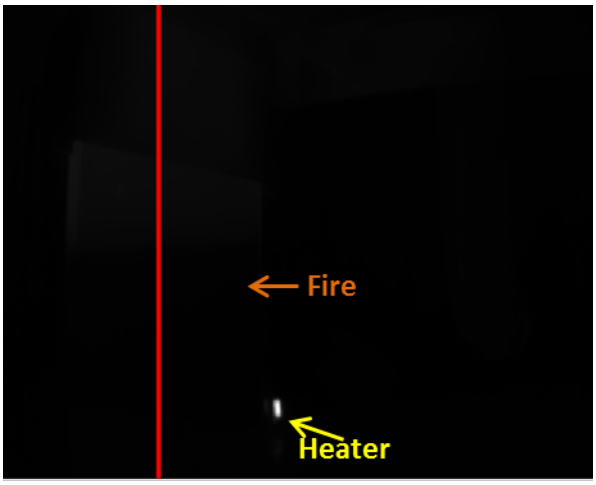

d

Figure 39. LWIR camera Position A for FLARE non-fire hot object scenario with heater near heading; results shown for (a) visible camera during latex foam test, (b) visible camera during propane test, (c) FLIR A35 during latex foam test, and (d) FLIR A35 during propane test

The heater was also used to test non-fire hot object discrimination at LWIR camera Position D. The heater was placed near the floor for the first scenario at this position. The test layout for this scenario is shown in Figure 40.

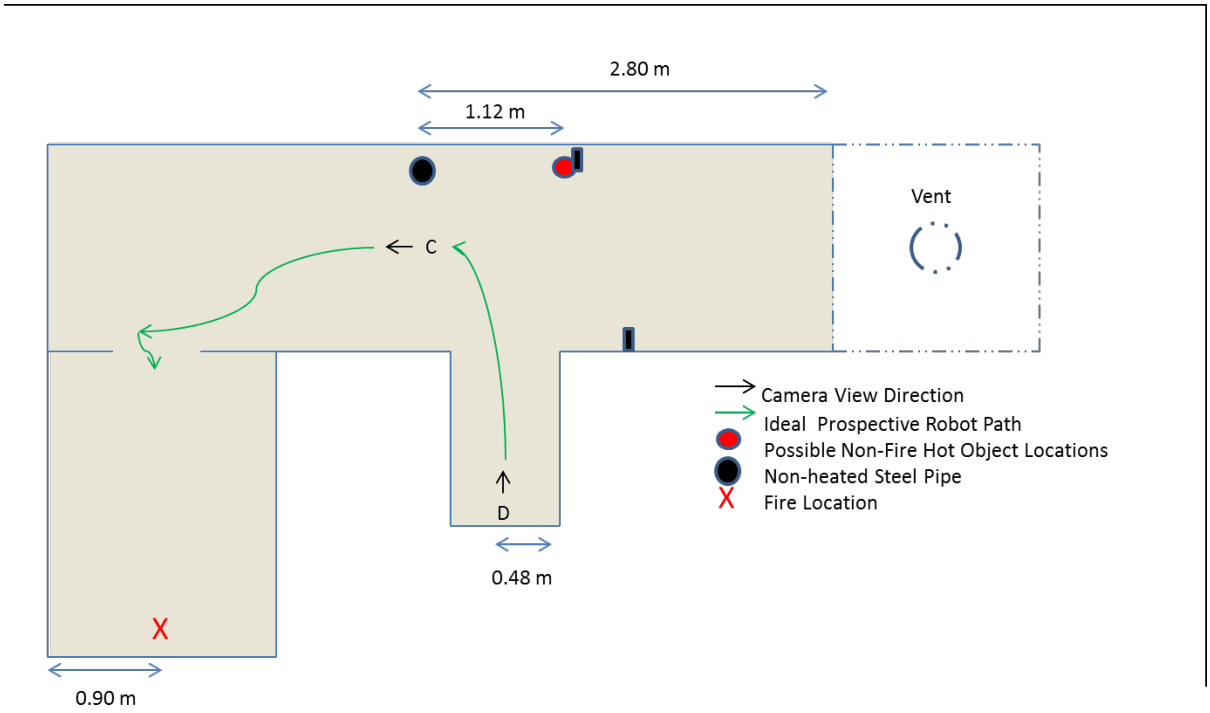

Figure 40. FLARE non-fire hot object discrimination with heater in view of LWIR camera Position D test scenario layout

The FLIR A35 results of the scenario described by Figure 40 are shown in Figure 41 for both the latex foam and propane fuel tests. A desired FLARE output coordinate for LWIR camera Position D was any that is located in the left half of the image. This corresponded to a heading that would lead a robot out from Position D into the hallway to the left in order to continue towards the chamber where the fire was located. All of the coordinates chosen by FLARE are correct for the scenario shown in Figure 40. These results are shown in Figure 41 for the FLIR A35.

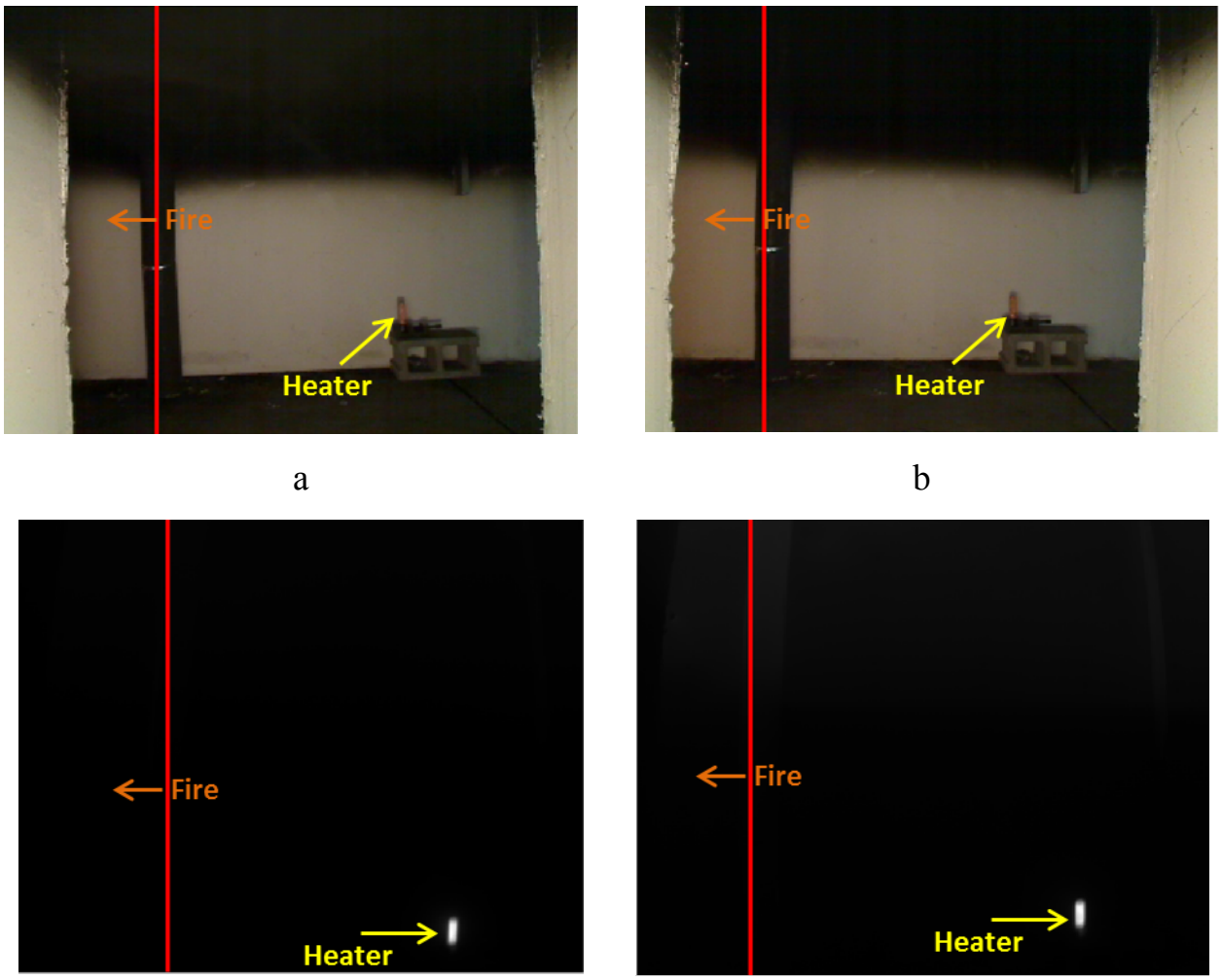

Figure 41. LWIR camera Position D for FLARE non-fire hot object scenario with a heater on the floor; results shown for (a) visible camera during latex foam test, (b) visible camera during propane test, (c) FLIR A35 during latex foam test, and (d) FLIR A35 during propane test

The last scenario has the same layout described in Figure 40. The heater is now located on the ceiling touching the steel stud in view of LWIR camera Position D. The heater was positioned to touch and heat the steel stud because the ceiling is not fully in the field of view of the LWIR cameras at the 0.76 m test height. The results of this scenario are shown in Figure 42 for the FLIR A35. The

FLARE coordinates shown in Figure 42 for the FLIR A35 are correct. The success of the test is determined by the final heading directing the prospective robot to the left towards the chamber containing the fire after exiting from LWIR camera Position D.

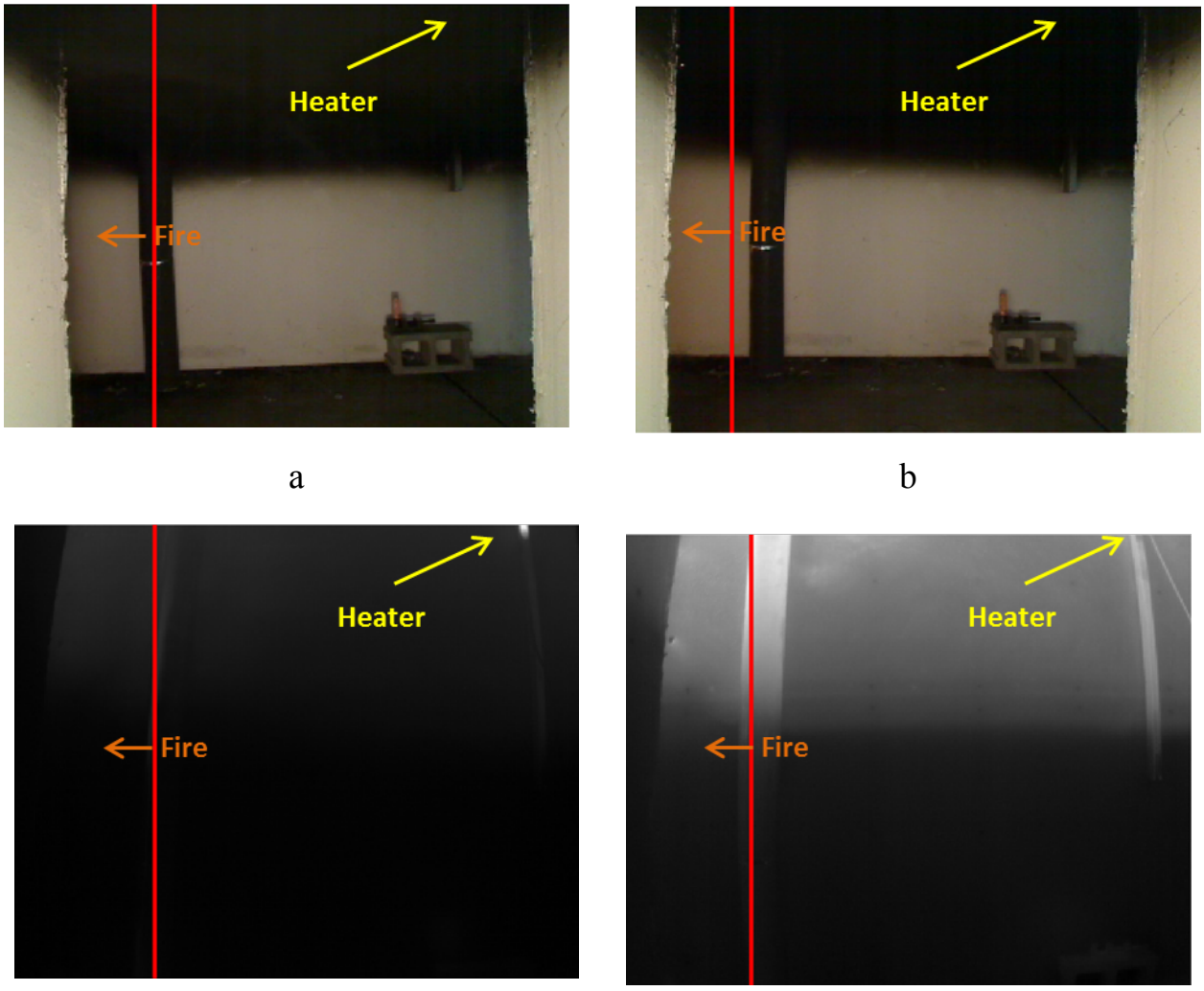

a b

c d

Figure 42. LWIR camera Position D for FLARE non-fire hot object scenario with a heater on the ceiling; results shown for (a) visible camera during latex foam test, (b) visible camera during propane test, (c) FLIR A35 during latex foam test, and (d) FLIR A35 during propane test

3.3.4 FLARE FLIR Tau 2-320 Errors

The results shown previously used the FLIR A35 for FLARE's input LWIR images. The same testing was also performed using the FLIR Tau 2-320 for the same scenarios and same LWIR camera positions. The results and output FLARE coordinates were consistent for nearly every case. The two test cases that differed were both latex foam tests where the camera was looking out from Position D. The first was the basic scenario with no non-fire hot object. The test layout for this case was shown in Figure 28. The error is shown in the result in Figure 43. The second error had a heater as a non-fire hot object on the floor off of the correct heading. The test layout for this case is shown in Figure 40. The second error is shown in Figure 44. In both cases, FLARE gave the same faulty final pixel coordinate to the right of the center of the image, when the correct heading was to the left. There were several potential reasons for this failure. The faulty pixel was located on a steel stud located within the enclosure for both cases. This steel stud is exposed to the combustion products circulating through the hallway of the enclosure as they exit the fire environment causing it to heat differently than the drywall surrounding it. The FLIR Tau 2-320 used fewer intensity values and therefore less of a dynamic range than the FLIR A35 to describe a given scene. FLIR A35 did not similarly fail for these cases because of the larger range used. The data from each test scenario including the dynamic pixel intensity range used by each camera for each scenario is shown in Table 3.

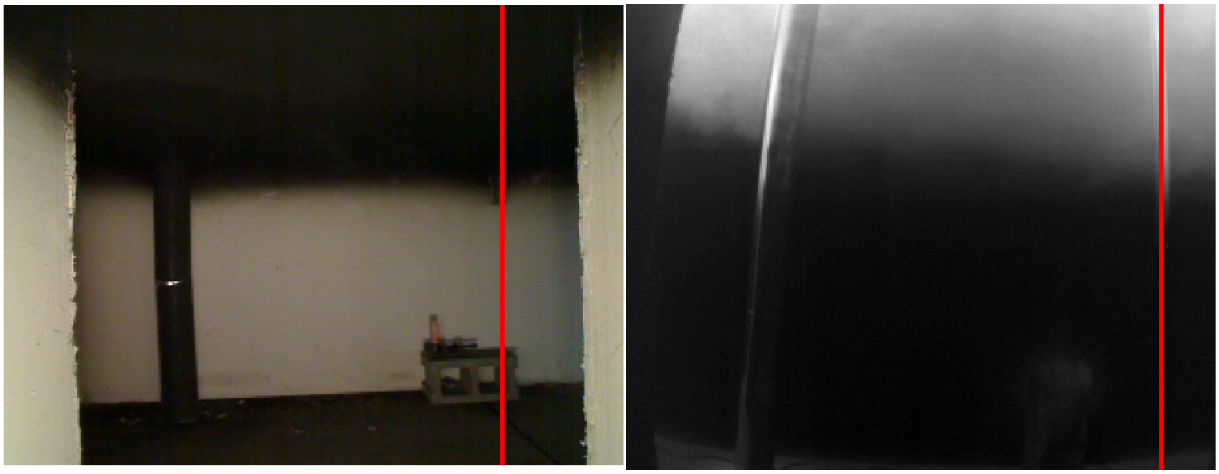

Figure 43. Visible camera (left) and FLIR Tau 2-320 (right) view from Position D for a latex foam test

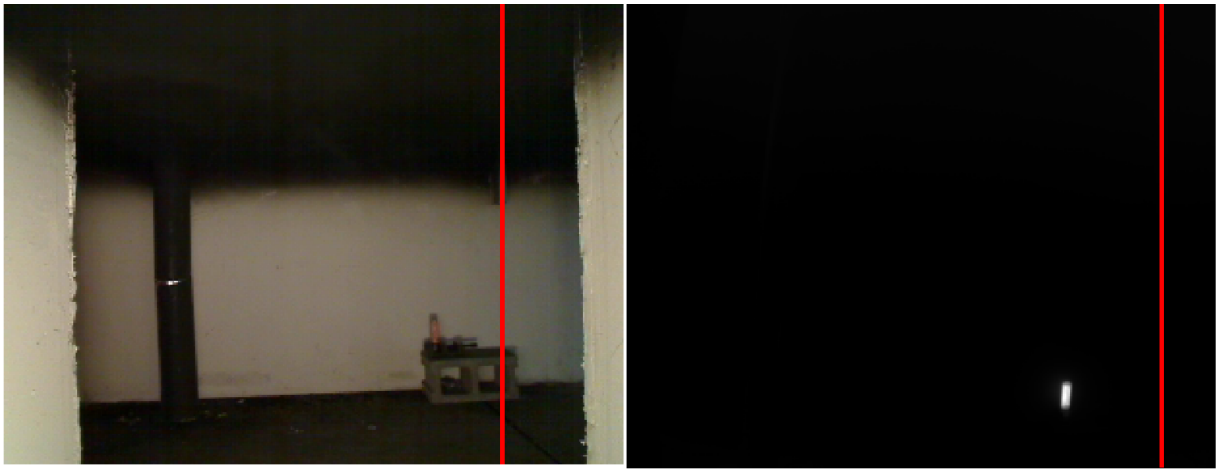

Figure 44. Visible camera (left) and FLIR Tau 2-320 view (right) from Position D with a heater on the floor for a latex foam test

Table 3. Data from each FLARE test scenario

		Tau-320				A35			
Position	Fuel	Max	Average	D	Dynamic Range	Max	Average	D	Dynamic Range
Basic Environment Scenario									
Position A	Latex Foam	6641	6436.8	204.2	259	-15018	-15268	250	323
Position B	Latex Foam	6456	6414.4	416	65	-15026	-15261	235	295
Position C	Latex Foam	6962	6600	362	466	-14736	-15122	386.5	542
Position D	Latex Foam	6604	6431.9	172.1	216	-15069	-15262	193	269
Position A	Propane	6731	6468	262.1	323	-14823	-15241	418	515
Position B	Propane	7009	6560.1	448.9	563	-14495	-15124	629	817
Position C	Propane	6906	6566	339.6	423	-14512	-15101	589	759
Position D	Propane	6923	6541.8	381.2	472	-14576	-15162	586	750
Non-Fire Hot Objects									
Position B with Heated Pipe	Latex Foam	6764	6429.3	334.7	391	-14781	-15228	447	552
Positon D with Heater Ceiling	Latex Foam	6483	6403	800	98	-14158	-15267	1109	1171
Position D with Heater Floor	Latex Foam	12906	6441	6465	6512	-6320	-15269	8949	9007
Position D with Heated Pipe	Latex Foam	7076	6436	639.7	685	-14931	-15213	282	392
Position A with Heater off Path	Latex Foam	12374	6421	5953	6008	-7164	-15284	8120	8186
Position A with Heater on Path	Latex Foam	12344	6420	5924	5972	-6914	-15286	8372	8438
Position B with Heated Pipe	Propane	6895	6476.1	418.9	508	-14601	-15175	574	727
Positon D with Heater Ceiling	Propane	6839	6490.4	348.6	440	-14573	-15153	580	742
Position D with Heater Floor	Propane	11960	6574	5386	5496	-7133	-15113	7980	8183
Position D with Heated Pipe	Propane	6583	6427.9	155.1	202	-14872	-15229	357	451
Position A with Heater off Path	Propane	11777	6452	5325	5380	-7753	-15255	7502	7589
Position A with Heater on Path	Propane	11948	6465	5483	5547	-7577	-15248	7671	7769
Fire									
Position E with Fire	Latex Foam	14054	7057	6996	7496	-1121	-14596	13475	14105
Position E with Fire	Propane	13945	6922.8	7022	7450	-1	-14339	14388	15238

3.4 Summary

The results of the tests for FLARE are summarized in Table 4 below. Each case was represented with green for a correct coordinate, yellow for a minor error with no consequence due to obstacle avoidance or the natural behavior within the enclosure, and red for a failure. The algorithm was successful based on the large-scale fire tests and lab fire environment it was tested in. The thresholds met by the difference (D) between the maximum and average relative intensity value for each test scenario image are also shown in Table 4. FLARE avoids non-fire hot objects of variable sizes and temperatures. FLARE consistently picked the correct heading leading to the fire's location regardless of the non-fire hot object's location in

relation to the correct heading. The two failures observed were caused primarily by the lower dynamic range used by the FLIR Tau 2-320 in comparison to the FLIR A35.

Table 4. FLARE testing results

Position	Fuel	Test Layout	FLIR A35 Results	FLIR Tau 2-320	FLIR A35	Thresholds
Basic Environment Scenario						
Position A	Latex Foam	Fig. 26	Fig. 27	Pass	Pass	$D<T_{HO}$
Position B	Latex Foam	Fig. 26	Fig. 28	Pass	Pass	$D<T_{HO}$
Position C	Latex Foam	Fig. 26	Fig. 29	Pass	Pass	$D<T_{HO}$
Position D	Latex Foam	Fig. 26	Fig. 30	Fail	Pass	$D<T_{HO}$
Position A	Propane	Fig. 26	Fig. 27	Pass	Pass	$D<T_{HO}$
Position B	Propane	Fig. 26	Fig. 28	Pass	Pass	$D<T_{HO}$
Position C	Propane	Fig. 26	Fig. 29	Pass	Pass	$D<T_{HO}$
Position D	Propane	Fig. 26	Fig. 30	Pass	Pass	$D<T_{HO}$
Non-Fire Hot Objects						
Position B with Heated Pipe	Latex Foam	Fig. 31	Fig. 32	Pass	Pass	$D<T_{HO}$
Positon D with Heater Ceiling	Latex Foam	Fig. 38	Fig. 40	Pass	Pass	$T_{HO}<D<T_{UV}$
Position D with Heater Floor	Latex Foam	Fig. 38	Fig. 39	Fail	Pass	$T_{HO}<D<T_{UV}$
Position D with Heated Pipe	Latex Foam	Fig. 31	Fig. 33	Pass	Pass	$D<T_{HO}$
Position A with Heater off Path	Latex Foam	Fig. 33	Fig. 35	Pass	Pass	$T_{HO}<D<T_{UV}$
Position A with Heater on Path	Latex Foam	Fig. 36	Fig. 37	Pass	Pass	$T_{HO}<D<T_{UV}$
Position B with Heated Pipe	Propane	Fig. 31	Fig. 32	Pass	Pass	$D<T_{HO}$
Positon D with Heater Ceiling	Propane	Fig. 38	Fig. 40	Pass	Pass	$D<T_{HO}$
Position D with Heater Floor	Propane	Fig. 38	Fig. 39	Pass	Pass	$D<T_{HO}$
Position D with Heated Pipe	Propane	Fig. 31	Fig. 33	Pass	Pass	$D<T_{HO}$
Position A with Heater off Path	Propane	Fig. 33	Fig. 35	Pass	Pass	$T_{HO}<D<T_{UV}$
Position A with Heater on Path	Propane	Fig. 36	Fig. 37	Pass	Pass	$T_{HO}<D<T_{UV}$
Fire Present in Scene						
Position E with Fire	Latex Foam	N/A	N/A	N/A	N/A	$D>T_{UV}$
Position E with Fire	Propane	N/A	N/A	N/A	N/A	$D>T_{UV}$

Chapter 4: UV Fire and Direction Discrimination

4.1 Introduction

Locating the fire is a significant challenge for FLARE; however, a definitive method to stop when the fire is within view of the LWIR camera was also needed. A method of recognizing when the fire location is reached is a fundamental design requirement for a fire location algorithm. After the fire is located and the alarm goes off, suppression can be queued in real life autonomous robotic firefighting applications. The Hamamatsu UVTRON R9454 sensor was selected to compliment the LWIR cameras to accomplish this goal. The large field of view (FOV) and high sensitivities allow this sensor to be alarmed to normal UV radiation from a lighter at a distance greater than 5 m.

The work presented in this chapter provides the experimental evaluation of the UV sensor for fire identification on the robot as a crucial part of FLARE. This included experiments to limit the field of view of the UV sensor to that of the LWIR cameras and quantify the ability of the UV sensor to operate in low visibility conditions.

4.2 Field of View Adjustment

Information about the fire location can be gained in addition to determining the presence of a fire by limiting the field of view of the UV sensor. The field of view of an unblocked UV sensor was tested using the platform shown in Figure 45. The field of view was tested by rotating the platform clockwise in 10° intervals with a propane torch lit 3 m away from the sensor as shown in Figure 46. The 10° step size used to test the field of views makes the experimental field of views obtained an approximate proof of concept value for each test. Both the sensor and the top of the flame were positioned 0.76 m off the ground for testing. The voltage

response from the UV sensor was taken for 3 seconds at each angle step. This data is used to create a polar plot of peaks per second.

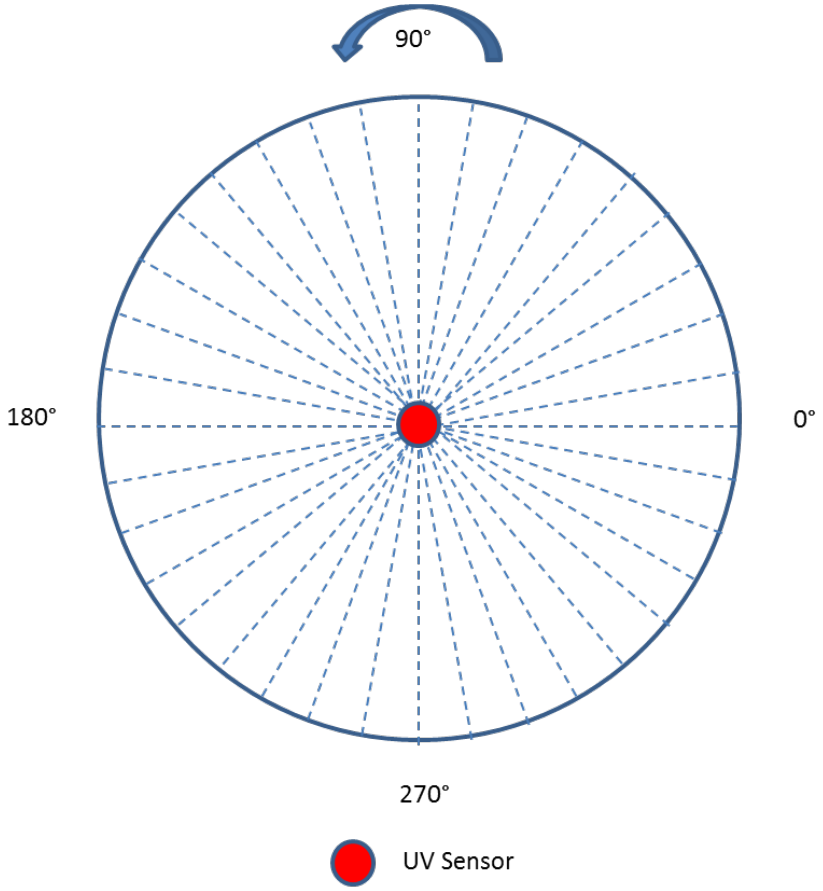

Figure 45. UV sensor field of view test platform

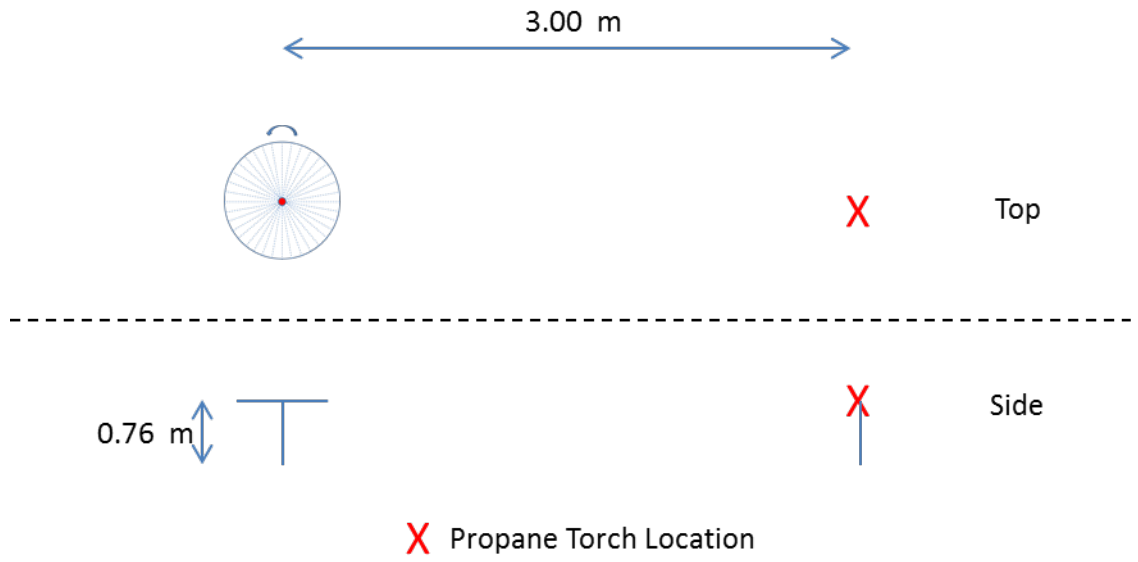

Figure 46. UV sensor field of view test layout

This test was used to determine the field of view of an isolated UV sensor. Each angle location was plotted in polar coordinates with its corresponding peaks per second value as shown in Figure 47 below. Only normal and strong radiation levels were considered to determine the experimentally observed field of view. Weak UV radiation is ignored by FLARE in real fire scenarios to limit false positives caused by reflections. Significant UV radiation is designated as values greater than the red line on the polar plot corresponding to 5 voltage peaks per second.

An unblocked UV sensor classified the propane torch as normal strength UV radiation between 0° and 200°. This means that the UV sensor has a much larger field of view than the 120° specified by Hamamatsu previously in Figure 5. It also recognized weak radiation for values between 200° and 360°. The UVTRON R9454 sensor can detect UV radiation even when it is not facing the radiation source.

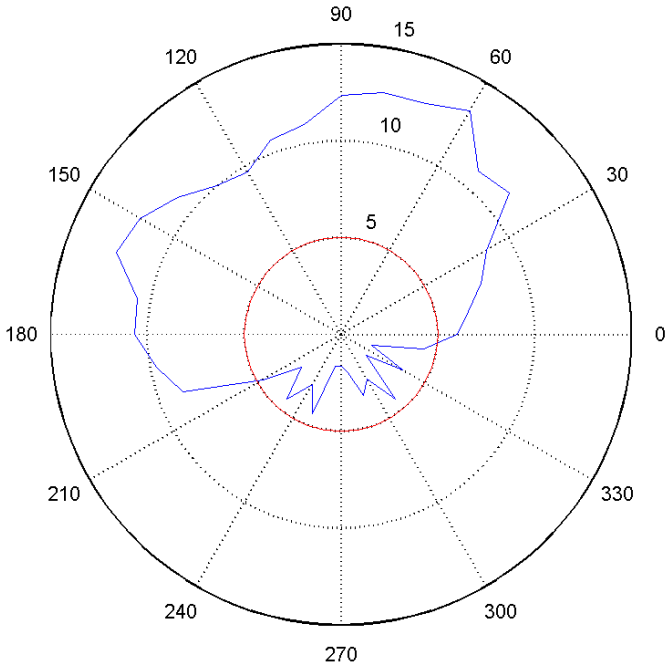

Figure 47. Field of view of unblocked UVTRON R9454

Three different methods were evaluated to limit the field of view and gain UV directional fire discrimination. These included an angled plate housing, bulb cover, and slit opening housing. The methods and their effectiveness are discussed in detail in the following sections.

4.2.1 Angled Plate Housing

The first method varied the UV sensor field of view using two plates oriented in a triangle to block the incoming radiation. A top view of this theoretical angled plate housing method with important dimensions is shown below in Figure 48.

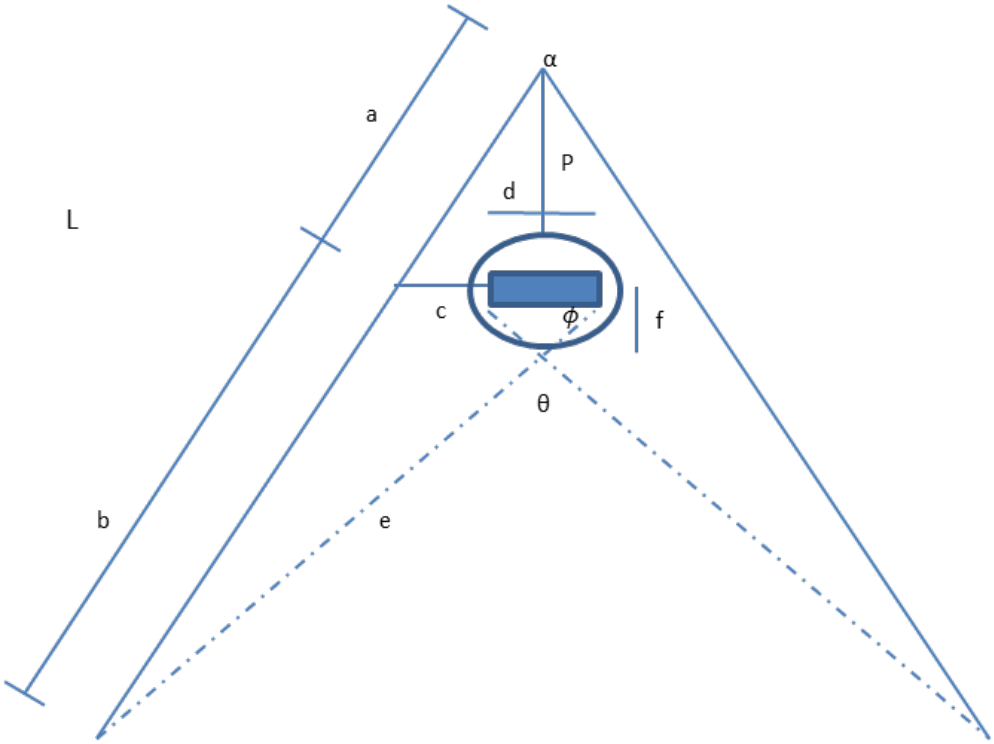

Figure 48. Angled plate housing field of view adjustment concept

Equations 7 and 8 show several geometric relationships used to calculate the necessary dimensions to find the theoretical field of view,

$$a = \frac{p}{\sin\left(90 - \frac{\alpha}{2}\right)} \quad \textbf{7}$$

$$c = P\tan\left(\frac{\alpha}{2}\right) \quad \textbf{8}$$

where a, c, and P are shown in Figure 45 and α is the opening angle between the two plates forming the triangle. P and α user defined inputs to the design of the angled plate housing. Equations 9 and 10 show the cosine and sine law applied to this design,

$$e = \sqrt{\left(c + \frac{d}{2}\right)^2 + b^2 - 2b\left(c + \frac{d}{2}\right)\cos\left(90 + \frac{\alpha}{2}\right)} \quad \textbf{9}$$

$$\phi = \sin^{-1}\left(\frac{b}{e}\sin\left(90+\frac{\alpha}{2}\right)\right) \qquad \textbf{10}$$

where d is the width of the UV sensor and ϕ is an angle used to calculate the theoretical expected field of view θ from,

$$\theta = 2(90-\phi) \qquad \textbf{11}$$

Variables b, c, and e are all shown in Figure 48. The width of the UV sensor plate, d, is approximately 0.006 m.

The opening angle (α), side length (L), and the placement of UV sensor within the triangle (P) determine the expected theoretical field of view (θ) of the UV sensor. The expected field of view (θ) for each opening angle scenario tested is shown below in Table 5. If the length is increased the expected field of view will decrease for a given opening angle.

Table 5. Expected fields of view for tested angled plate housings

		L (m)	P (m)	d (m)		
		0.076	0.025	0.006		
α	a(m)	b(m)	c(m)	e(m)	ϕ	θ
50	0.03	0.05	0.01	0.06	51	78
70	0.03	0.04	0.02	0.06	38	104
90	0.04	0.04	0.03	0.06	26	127
120	0.05	0.03	0.04	0.07	10	159

The width of the sensor itself affects the minimum field of view theoretically possible. The sensor, including the bulb, is 0.012 m at the widest location limiting P and c dimensions as shown in Figure 48. The lowest field of view obtainable theoretically for a plate length of 0.076 m is 44° with an opening angle of 19° and a distance P of 0.036 m. The lowest field of view theoretically possible for different plate lengths is plotted below in Figure 49. The red line corresponds to the 48° field of view of the LWIR camera. The minimum plate length to limit the field of view of the UV sensor to that of the LWIR cameras is approximately 0.07 m as shown in Figure 49.

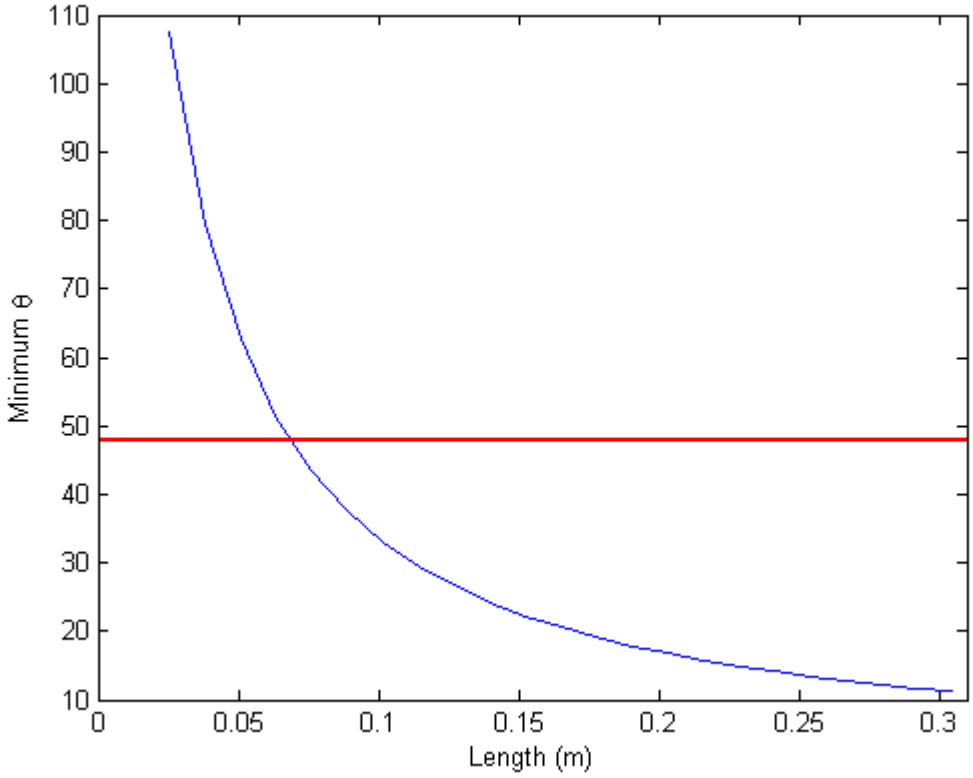

Figure 49. Minimum theoretical field of view for varied plate lengths for the angled plate housing method

The angled plate housing method was tested using the platform and propane torch shown in Figures 45 and 46. A series of tests were performed as a proof of concept by varying opening angles with 0.076 m plates and placing the sensor at P=0.0254 m. Opening angles tested include 50°, 70°, 90°, and 120° shown in Table 5. The plates were painted with high heat Rustoleum flat black spray paint to limit possible error from reflections.

The angled plate housing limited the field of view of the UV sensor. The experimental field of view increased with opening angle as expected. The experimental values appeared much closer to the opening angles than the theoretically calculated field of views. Despite the success of the angled plate housing method, this method required housing with a minimum plate length of

0.07 m to pair the sensor with the field of view of the LWIR cameras. This large size was not preferred for mobile robotic applications with strict design requirements for weight and sensor placement. The results are shown for the angled plate housing method in Figure 50 and Table 6 for each opening angle case.

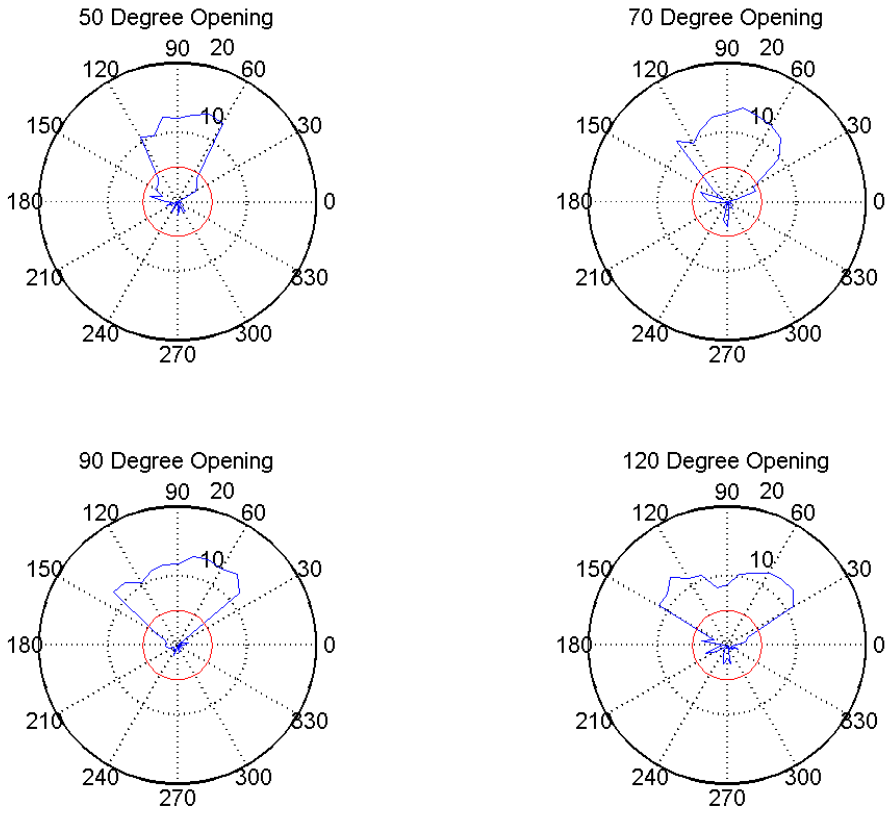

Figure 50. Experimental field of view results for angled plate housing method

Table 6. Experimental and theoretical fields of view for angled plate housings with different opening angles

L (m)	P (m)	d (m)
0.076	0.025	0.006
α	Theoretical θ	Experimental θ
50	78	60
70	103	80
90	127	100
120	159	120

4.2.2 Bulb Cover

A simple alternative method was covering the UV sensor bulb itself. A top view of the theoretical representation of this type of cover is shown below in Figure 51. The black outline represents the cover in Figure 51.

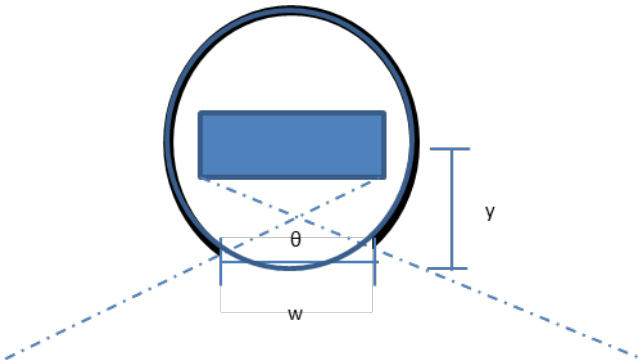

Figure 51. Bulb cover field of view adjustment concept

The bulb has a cylindrical body and can be easily wrapped with electrical tape for certain percentages of the circumference. This method was tested by covering 50% of the bulb by simply covering the back. The remaining visible surface area of the bulb was then iteratively cut in half for successive tests. The bulb covering percentages applied and tested were approximately 50%, 75%, 88%, and 94%. The theoretical field of views expected can be calculated using Equation 12,

$$\theta = 2\tan^{-1}\left(\frac{\frac{w}{2}+\frac{d}{2}}{y}\right) \quad \textbf{12}$$

where θ is the field of view calculated using the cover opening width w, the sensor plate width d which is equal to 0.006 m and y, which is the distance between the cover and the sensor. For the bulb cover method y is 0.005 m corresponding to the radius of the UV sensor bulb. The theoretical field of view expected for different percentages of the bulb covered are shown in Table 7.

Table 7. Expected fields of view for various bulb coverage percentages

% Covered	d(m)	w(m)	y(m)	θ
50	0.006	0.015	0.005	131
75	0.006	0.007	0.005	110
88	0.006	0.004	0.005	90
94	0.006	0.002	0.005	79

This field of view adjustment design was tested in the same way as the angled plate housing method. The results of the test are shown for each percentage of the UV sensor that was covered in Figure 52 and Table 8. The field of view was lowered to less than 40° by covering 94% of the UVTRON bulb as shown in Figure 52 and Table 8. That being said, this method requires a lot of precision to be useful for dependable implementation on to a robotic platform.

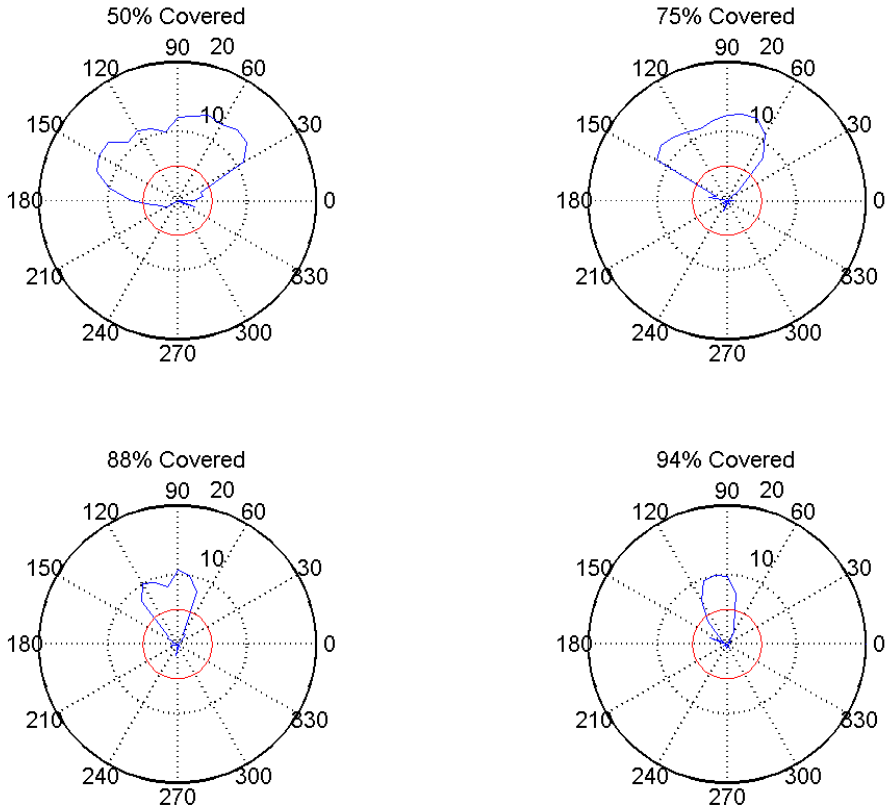

Figure 52. Experimental field of view results for bulb covering method

Table 8. Experimental and theoretical fields of view for different bulb coverage percentages

d (m)		y (m)
0.01		0.005
% Covered	Theoretical θ	Experimental θ
50	131	150
75	110	100
88	90	60
94	79	40

This method is susceptible to human error, as the distances being covered are very small. This made them difficult to properly cover by hand. Errors of this type can affect the center of the field of view of the sensor if the cover is shifted to

the right or left. The sensor could easily be covered too much and keep UV radiation from the sensor entirely.

4.2.3 Slit Opening Housing

The final method used to limit the field of view of the UVTRON R9454 sensor was the slit opening housing method. A top view of the theoretical slit opening housing method is shown below in Figure 53.

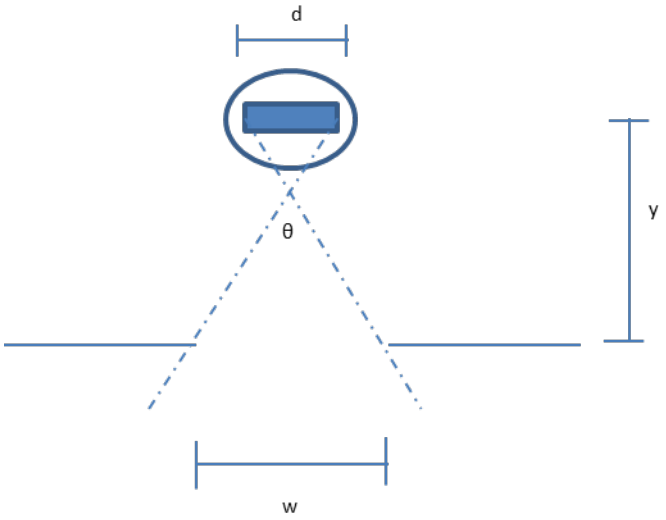

Figure 53. Theoretical slit opening housing field of view adjustment concept

Using simple geometric relationships the expected field of view (θ) is found using Equation 12 repeated here for convenience,

$$\theta = 2\tan^{-1}\left(\frac{\frac{w}{2}+\frac{d}{2}}{y}\right) \qquad \textbf{12}$$

where θ is the field of view, y is the distance between the slit opening, d is the metal sensor width, and w is the slit width. The y distance was set to 0.02 m in order to giving plenty of space for the UV sensor within the housing. A table of tested slit widths and expected field of views can be found in Table 9 below.

Table 9. Expected fields of view for chosen slit opening widths

d(m)	w(m)	y(m)	θ
0.006	0.006	0.02	35
0.006	0.013	0.02	50
0.006	0.019	0.02	65
0.006	0.025	0.02	77

The slit opening housing method for limiting the field of view of the UV sensor was tested similar to the previous methods using the rotating platform and propane torch shown in Figure 45 and Figure 46. The slit opening was constructed using two 0.15 m by 0.1 m aluminum plates. The plates were spray painted with flat black high heat Rustoleum paint similar to those used to test the angled plate housing method.

The results for the slit opening housing method are shown for each slit width in Figure 54 and Table 10. Each experimental field of view was shown to be less than those theoretically calculated similar to the angled plate housing method. This method showed the least variation between experimentally determined and theoretically calculated fields of view.

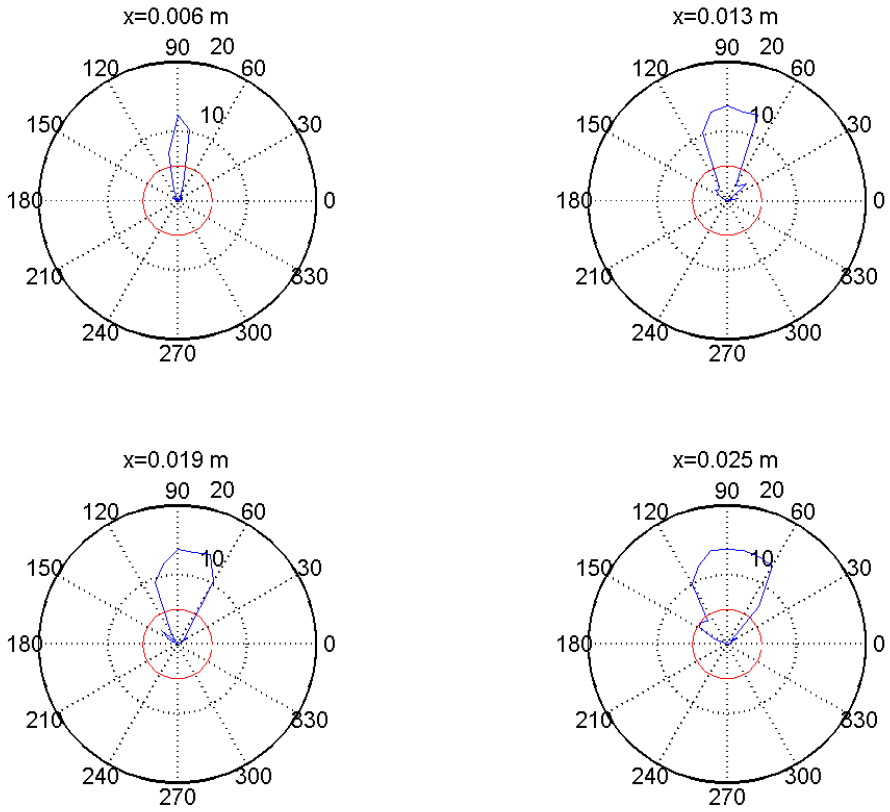

Figure 54. Experimental field of view results for slit opening housing method

Table 10. Theoretical and experimental fields of view for attempted slit opening housing methods

d (m)		y (m)
0.01		0.01
w(m)	**Theoretical θ**	**Experimental θ**
0.006	35	20
0.013	50	40
0.019	65	50
0.025	77	70

The slit opening housing method could be more easily implemented in a housing that holds the UV sensor than the angled plate housing. A slit opening housing would be much smaller than the smallest possible angled plate housing for

a field of view that would correspond to the LWIR cameras. The slit opening housing method was shown to be the most suitable option in terms of ease of implementation and size. The field of view should be between 40° and 50° similar to that of the LWIR camera. This field of view corresponds to a slit width of approximately 0.013 m. The LWIR camera and the UV sensor should be aligned when the system is integrated on the robot.

4.3 Visibility Experiment

The UV sensor was rendered useless in low visibility test conditions. This is to be expected applying the same logic that justifies the use of LWIR cameras for low visibility fire scenarios. The visibility increases with wavelength because of the inverse relationship between extinction coefficient and wavelength. [19]. The Hamamatsu UVTRON R9454 operates in the 185 to 260 nm wavelength range which is much lower than the 7.5 to 13.5 μm range of the LWIR cameras.

To demonstrate this behavior, one UV sensor is placed in the smoke layer, 1.5 m above ground, directly opposite a constant 25 kW propane fire at the end of the hallway. A latex foam fire was started outside the view of the sensor inside of the room. A latex foam fire produces smoke; however, it is a smaller flame which burns out after approximately 200 s. A constant propane flame is brighter and a better test of whether or not the UV sensor could be alarmed through the smoke. This test layout is shown in Figure 55. The UV sensor's number of voltage peaks per second for different visibility levels reached during the test is shown in Figure 56.

Figure 56 shows that the UV response voltage peaks per second and therefore the strength of the UV signal observed increased as visibility increased. This also shows that the sensor is not capable of recognizing the fire at visibility levels less than 3 m for these test conditions. This test advocated the placement of

UV sensors below the smoke layer, close to the ground, for any real world robotic application of FLARE.

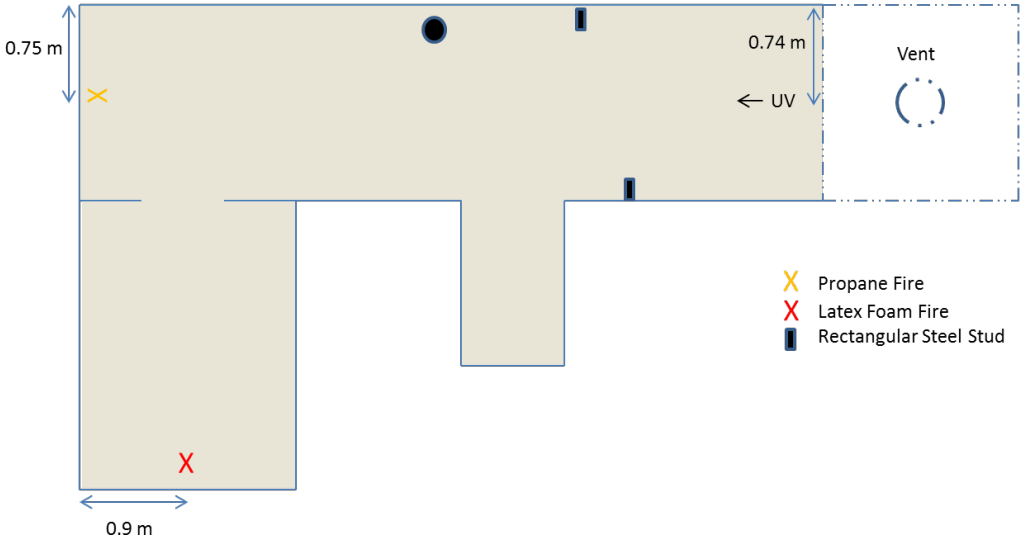

Figure 55. UV sensor visibility test layout

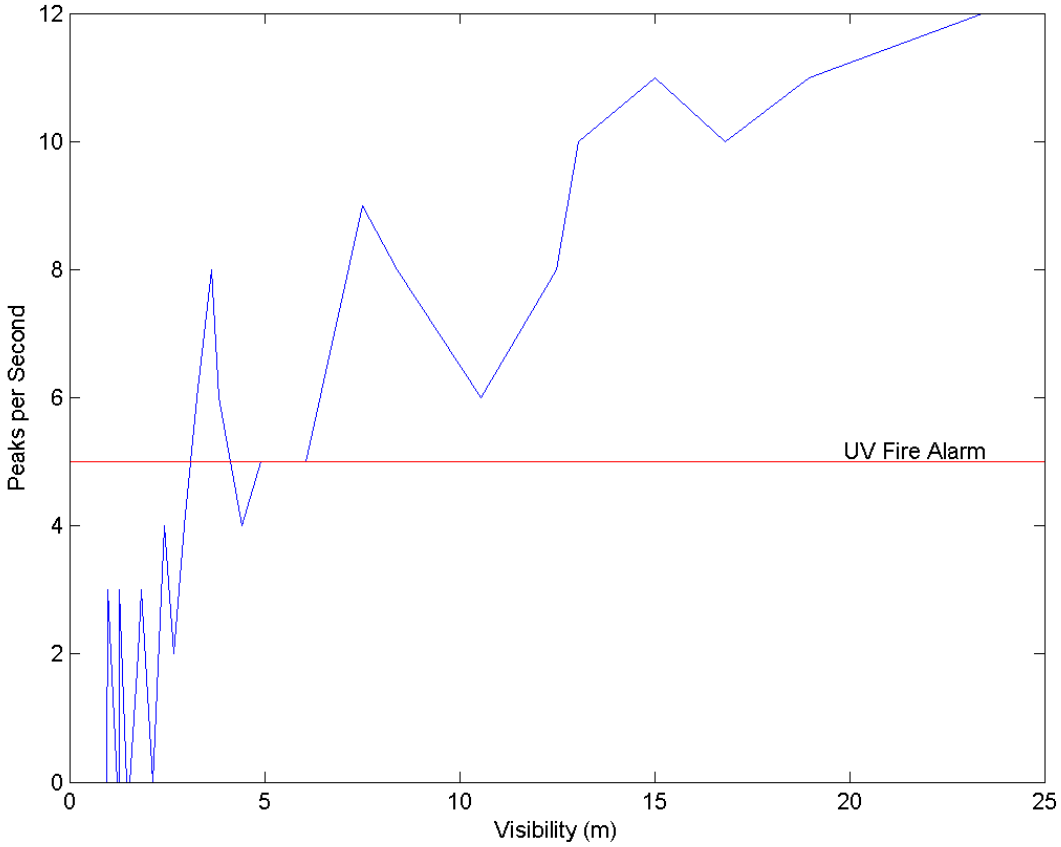

Figure 56. UV peaks per second for different smoke visibility levels

Chapter 5: Conclusions and Recommendations

5.1. Conclusions

A multi-spectral system was developed in this work to provide heading determination for an autonomous robot to locate fires inside structures. The system includes a LWIR camera and UV sensor to collect information about the fire environment. A LWIR camera was chosen for its ability to see through smoke in thermal environments. The UVTRON R9454 UV sensor is chosen for its particular wavelength range and ability to discriminate between fires and non-fire hot objects.

The UV sensors should be paired with the LWIR camera and the FLARE algorithm to avoid potential errors caused by UV reflections within the indoor structure. Larger fires correspond to higher UV response due to reflections that can trigger false alarms based on testing with 25 kW and 60 kW propane fires.

FLARE was shown successful for many scenarios. FLARE gave correct headings for multiple LWIR camera positions throughout the indoor test facility with a fire outside of direct view. FLARE was also successful in discriminating between non-fire hot objects and actual fires using the multi-spectral approach. FLARE provided correct heading results in tests that used a large heated steel pipe and a small heater over 100°C regardless of the object's location in the scene or the LWIR camera position within the test facility. The FLARE algorithm works better with the FLIR A35 camera. This is because the FLIR A35 uses a larger dynamic pixel range to describe any given scene.

UV sensors have a unique ability to detect fires with very few sources of false alarms. UV signal strength can be determined by analyzing for the number of voltage peaks in a second. UV sensors have very large fields of view. Hamamatsu claimed that the field of view of an unblocked UVTRON R9454 sensor was 120°;

however, experimental data shows that it is closer to 200° with some response in all directions. Several different methods were shown to limit the field of view of the UV sensors so that it can be paired with the LWIR cameras. These methods were angled plate housings, bulb coverings, and slit opening housings.

The angled plate housing theoretically requires a minimum plate length of approximately 0.07 m to achieve a field of view corresponding to that of the LWIR camera. This is not preferred for mobile robotic application with design constraints on size and weight. The bulb cover method required a high level of precision while being susceptible to human error and the possibility of unintentionally blocking the sensor. The slit opening housing method was recommended for ease of implementation and size required to limit the field of view of the sensor to that of the LWIR cameras.

The UV sensor should be mounted below the smoke layer on the robotic platform. The UV sensor is unable to detect UV radiation from a 25 kW propane flame at visibility levels of less than 3 m.

5.2. Recommendations

Further testing is required to build on the success of this research project. The algorithm developed here should be shown to work in other complex fire scenarios with larger fire types to demonstrate the algorithm is general and robust.

FLARE was tested here in one indoor enclosure with two different fire fuel types. FLARE should be tested in different indoor enclosures with varying geometric layouts. The tests should include larger fires in order push the limits of the algorithm. The fire's location outside of view should also be varied to produce different wall surface temperature and intensity profiles. Industrial and residential locations with more material types present could provide more insight into the

impact of reflections and demonstrate this challenge has been solved with the current multi-spectral approach.

Each individual component used to create the UV alarm component of FLARE has been tested. This should be tested further as a system in more large-scale fire scenarios. The mobile robotic test platform and the SAFFiR humanoid platform should be used to further test the integration of FLARE with obstacle avoidance, localization, multi-spectral platform, and the autonomous suppression system in development. These robotic platforms should be used for any further algorithm development. A gravity sensor should be used to determine the orientation of the LWIR camera when mounted to a mobile robotic platform.

FLARE should be developed further using image region grouping and image filtering techniques. The 14 bit raw intensity data from the FLIR A35 should be correlated to temperature. The temperatures and size information may help classify and further discriminate against non-fire hot objects. The temperature correlation could also be used for casualty and human identification.

References

1. USFA, "2012 Firefighter Fatality Statistics", (1/7/2013) Retrieved from: www.usfa.fema.gov, Last Accessed 4/17/2013
2. Celik, and Demirel, "Fire detection in video sequences using a generic color model," *Fire Safety Journal* Vol. 44, Issue 2, pp. 147-158, 2009
3. Celik, Demirel, Ozkaramanli, Uyguroglu, "Fire detection using statistical color model in video sequences, "*Journal of Visual Communication and Image Representation,* Vol. 18, Issue 2, pp. 176-185, 2007
4. Celik, Ma, "Computer vision based fire detection in color images," *Proceedings IEEE Conference on Soft Computing in Industrial Applications,* 25-27 June 2008, pp. 258-263
5. Celik, Ozkaramanh, and Demirel, "Fire and Smoke Detection Without Sensors: Image Processing Based Approach," *15th European Signal Processing Conference,* 2007
6. Celik, Ozkaramanh, Demirel, "Fire pixel classification using fuzzy logic and statistical color model," *IEEE International Conference on Acoustics, Speech and Signal Processing,* 15-20 April 2007, Vol. 1, pp. 1205-1208
7. Toreyin, Dedeoglu, Gudukbay, Cetin, "Computer Vision Based method for real-time fire and flame detection," *Pattern Recognition Letters,* Vol. 27, Issue 1, pp. 49-58, 1 January 2006
8. Ko, Cheong, Nam, "Early fire detection algorithm based on irregular patterns of flames and hierarchical Bayesian Networks," *Fire Safety Journal*, Vol. 45, Issue 4, pp. 262-270, 2010
9. Ishida, Tanaka, Taniguchi, Moriizumi, "Mobile robot navigation using vision and olfaction to search for a gas/odor source," *Autonomous Robots,* Vol. 20, Issue 3, pp 231-238, 2006.

10. Marjovi, Marques, “Multi-robot olfactory search in structured environments,” *Robotics and Autonomous Systems,* Vol 59., Issue 11, pp. 867-881, 2011.

11. Heland, Schaefer, and R. Haus, “Investigations of hot exhaust gases with passive FTIR emission spectroscopy.” *International Society of Optics and Photonics (SPIE),* SPIE Vol. 3493, pp. 2-10, 1998

12. Rego-Barcena, Saari, Mani, El-Batroukh, and M. Thomson, “Real time, non intrusive measurement of particle emmisivitiy and gas temperature in coal-fired power plants, “ *Measurement Science and Technology,* Vol. 18, No. 11, pp. 3479-3488, 2007

13. Chaffin, Marshall, Combs, Knapp, Kroutil, Fateley, R.M. Hammaker, “Passive fourier transform infrared monitoring of SO_2 in smokestack plumes: A comparison of remote passive spectra of an actual hot plume with emission spectra collected with a heatable cell,” *Proceedings Optical Sensing for Environmental and Process Monitoring SPIE,* pp. 302-313, 31 May 1995

14. Kostrzewa, Meyer, Poe, Terre, Salapow, Raimondi, “Addressing the challenges of thermal imaging for firefighting applications,” *Proceedings SPIE* Vol. 5074, pp. 564-574, 2003

15. Amon, Hamins, Bryner, and Rowe, “Meaningful performance evaluation conditions for fire service thermal imaging cameras,” *Fire Safety Journal*, Vol. 43, Issue 8, pp. 541-550, 2008.

16. Amon, Hamins, and Rowe, “First responder thermal imaging cameras: establishment of representative performance testing conditions.” *Proceedings SPIE* Vol. 6205, pp. 293-304, April 18, 2006

17. F. Amon and N. Bryner, “Measurement of effective temperature range of fire service thermal imaging cameras.” *Proceedings of SPIE,* Vol. 6941, Issue 1, 2008.

18. Vollmer and Möllmann, “Infrared Thermal Imaging: Fundamentals, Research, and Applications” 593p, 2010.

19. Katayama, Naitoh, Suganuma, Harada, Okamura, Tange, and K. Nakau, “Development of the Compact InfraRed Camera (CIRC) for wildfire detection,” *Proceedings of SPIE*, Vol. 7458, 2009.

20. Yan, Weisheng, Xudong, Yi, and X. Qi, “Research on infrared thermal imaging systems for field temperature measurement.” *Proceedings of SPIE,* Vol. 7383, 2009.

21. Joseph Starr, Brian Lattimer, “Evaluation of navigation sensors in smoke environments,” 2011

22. Liu, Yu, and Y. Zhang, “Nighttime video smoke detection based on active infrared video image, “ *Proceedings International Conference on Electrical and Control Engineering*, pp. 1359-1362, 25-27 June 2010

23. Toreyin, Cinbis, Dedeoglu, Cetin, “Fire detection in infrared video using wavelet analysis,” *Optical Engineering*, Vol. 46, Issue 6, 2007

24. Owrutsky, Steinhurst, Minor, Rose-Pehrsson, Williams, Gottuk, “Long wavelength video detection of fire in ship compartments,” *Fire Safety Journal*, Vol. 41, Issue 4, pp. 315-320, 2006

25. Gottuk, Lynch, Rose-Pehrsson, Owrutsky, Williams, “Video Image Fire Detection for Shipboard Use,” *Fire Safety Journal,* Vol. 41, Issue 4, pp. 321-326, 2006

26. N. Docquier and S. Candel, “Combustion control and sensors: a review,” *Progress in Energy and Combustion* Science, Vol. 28, Issue 2, pp. 107-150, 2001

27. Weiser and N. Eisenreich, “Fast emission spectroscopy for a better understanding of pyrotechnic combustion behavior,” *Propellants Explosives Pyrotechnics,* Vol. 30, Issue 1, pp. 67-78, 2005

28. Nussbaum, Liptak, and S. Pate, “Instrument Engineers’ Handbook: Process Measurement and Analysis” Fourth Edition, Vol. I, 1914p, 2003

29. Monroy, Munoz, Omnes, and Jean-Luc Reverchon, “Wide bandgap UV photodetectors: A short review of devices and applications”, *Proceedings SPIE,* Vol. 6473, 2007

30. Arthur E. Cote, “Operation of Fire Protection Systems”, *National Fire Protection Association*, pp. 26, 2003

31. http://www.hamamatsu.com/resources/pdf/etd/R9454_R9533_TPT1019E05.pdf

32. Monroy, Omnes, and F. Calle, “Wide-bandgap semiconductor ultraviolet photodetectors,” *Semiconductor Science and Technology,* Vol. 18, No. 4, pp R33-R51, 2003

33. Street, and F. W. Williams, “The implementation and demonstration of flame detection and wireless communications in a consumer appliance to improve fire detection capabilities,”, *Naval Research Laboratory,* pp. 1-21, 2007

34. Garth Watkins “The Selection and Placement of Flame Detectors for Maximum Availability of the Detection System.” *Onshore and Offshore (Papers presented at the Third International Conference on Management and Engineering of Fire Safety and Loss Prevention*, 295p, 18-20 February 1991

35. http://www.hamamatsu.com/resources/pdf/etd/C10423_TPT1023E02.pdf

36. http://www.hamamatsu.com/resources/pdf/etd/C10423.pdf

37. ASTM 1354-11b, “Standard Test Method for Heat and Visible Smoke Release Rates for Materials and Products Using an Oxygen Consumption Calorimeter”

38. International Standards Organization (ISO) 9705:1993(E), International Standard for Fire Tests—Full Scale Room Test for Surface Products, *International Organization for Standardization (ISO)*, Geneva, Switzerland, 1993

39. *The Society of Fire Protection Engineers*, 2008. SFPE Handbook of Fire Protection Engineering, 4th Edition.

Appendix A: Noise Analysis for Visibility Calculation

FFT of laser intensity signal

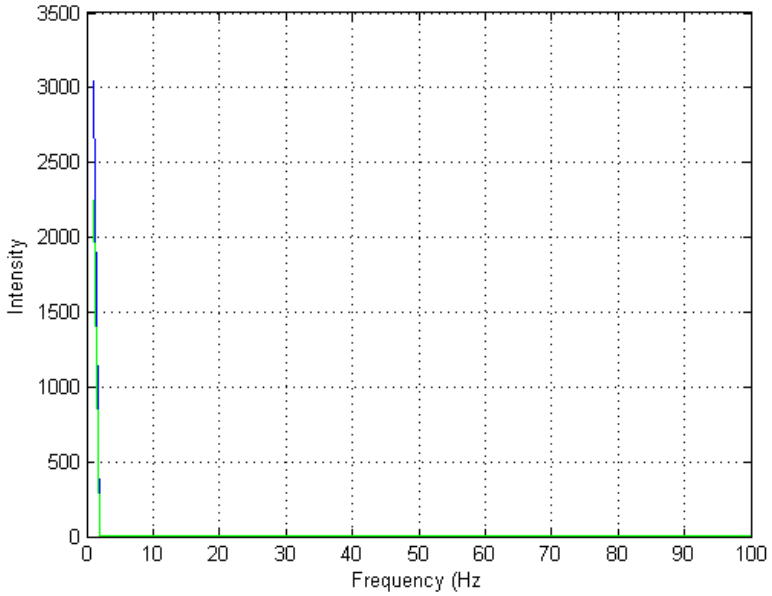

Figure A-1. FFT of photodiode intensity with ventilation blower, fan, and photodiode purge air turned off

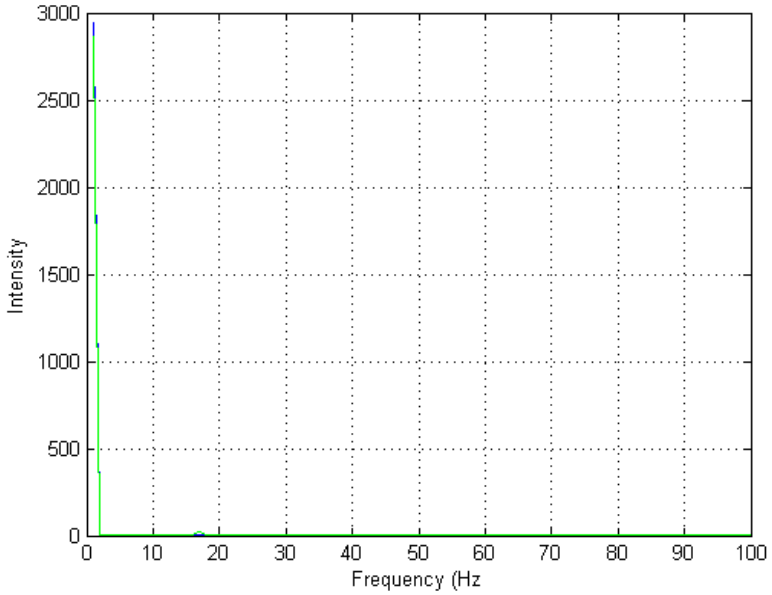

Figure A-2. FFT of photodiode intensity with ventilation blower, fan, and photodiode purge air turned on

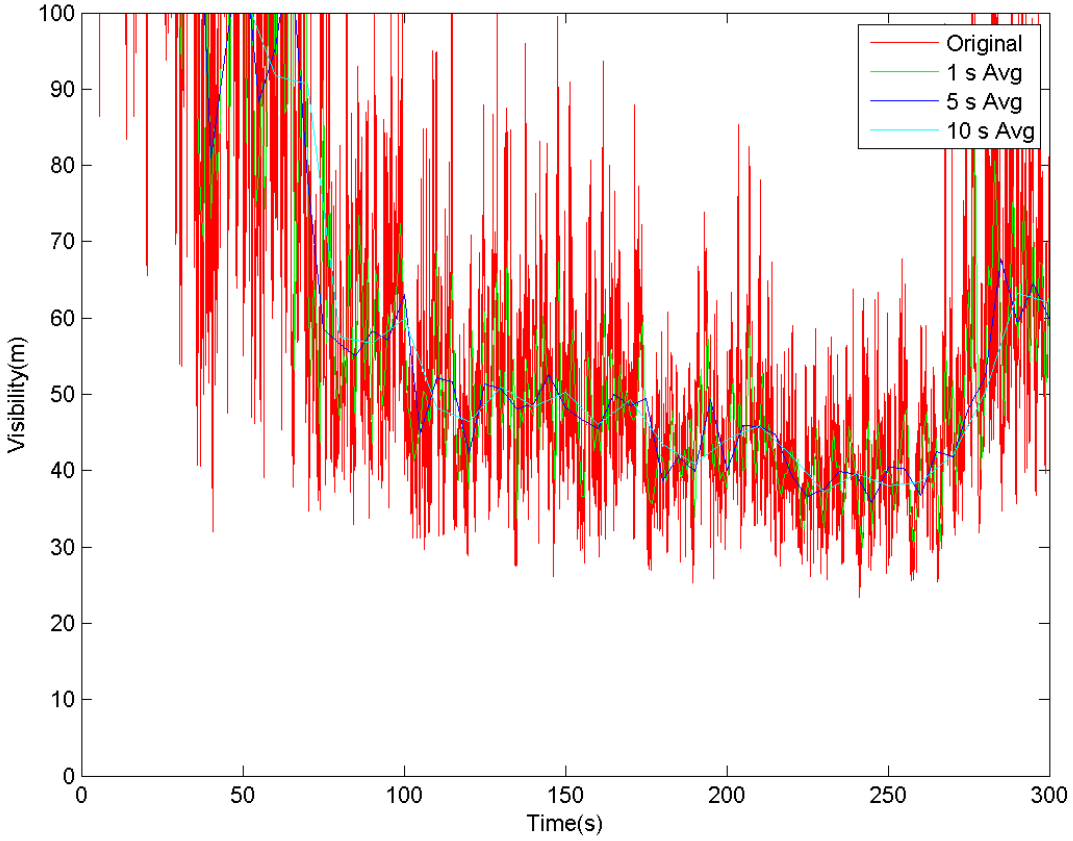

Figure A-3. Impact of moving average smoothing on low frequency noise present for propane test Laser 1 intensities

Appendix B: Impact of Non-Fire Hot Object Discrimination

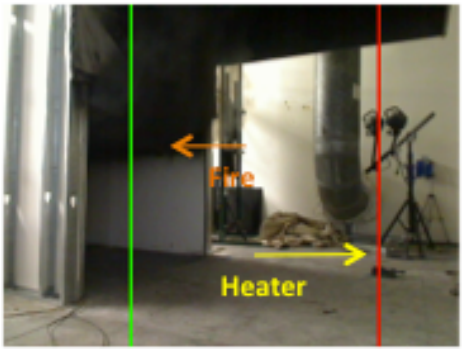

a

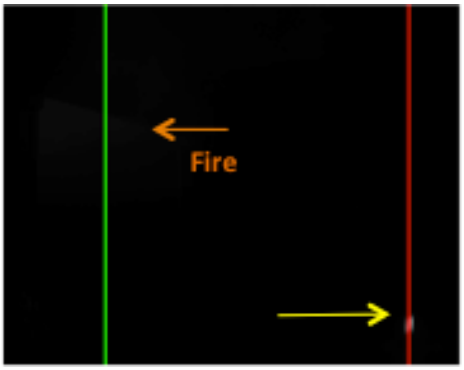

b

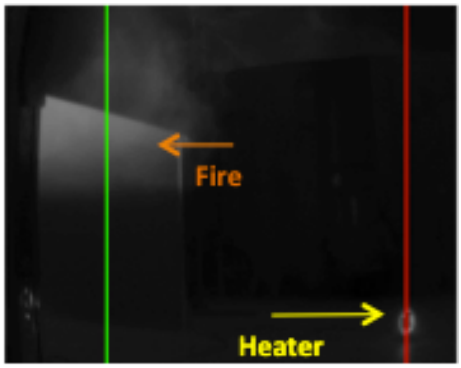

c

Figure B-1. Effect of non-fire hot object discrimination on FLARE output heading. (red without, green with), Results with red as the heading with out discrimination and green as the heading with discrimination in (a) visible reference image from non-fire hot object in view of LWIR camera Position A, (b) FLIR A35 output prior to non-fire hot object discrimination portion of FLARE shown in Figure 21, and (c) FLIR A35 output after non-fire hot object discrimination part of FLARE shown in Figure 21.

Appendix C: FLARE Result Variation Analysis

The variation in FLARE output coordinate over burn time for the latex foam and propane test scenarios is shown below in Figures C-1 through C-10 for the FLIR A35. The green line boundary refers to the boundary of correct coordinate values. The yellow line boundary shown on images from Position B and C correspond to coordinates that were considered minor error. The results are shown for 50 to 250 seconds into the test allowing for a 50 second baseline. This is verified by the temperature data shown in Figures 14 and 16 in Chapter 2 for latex foam and propane tests respectively.

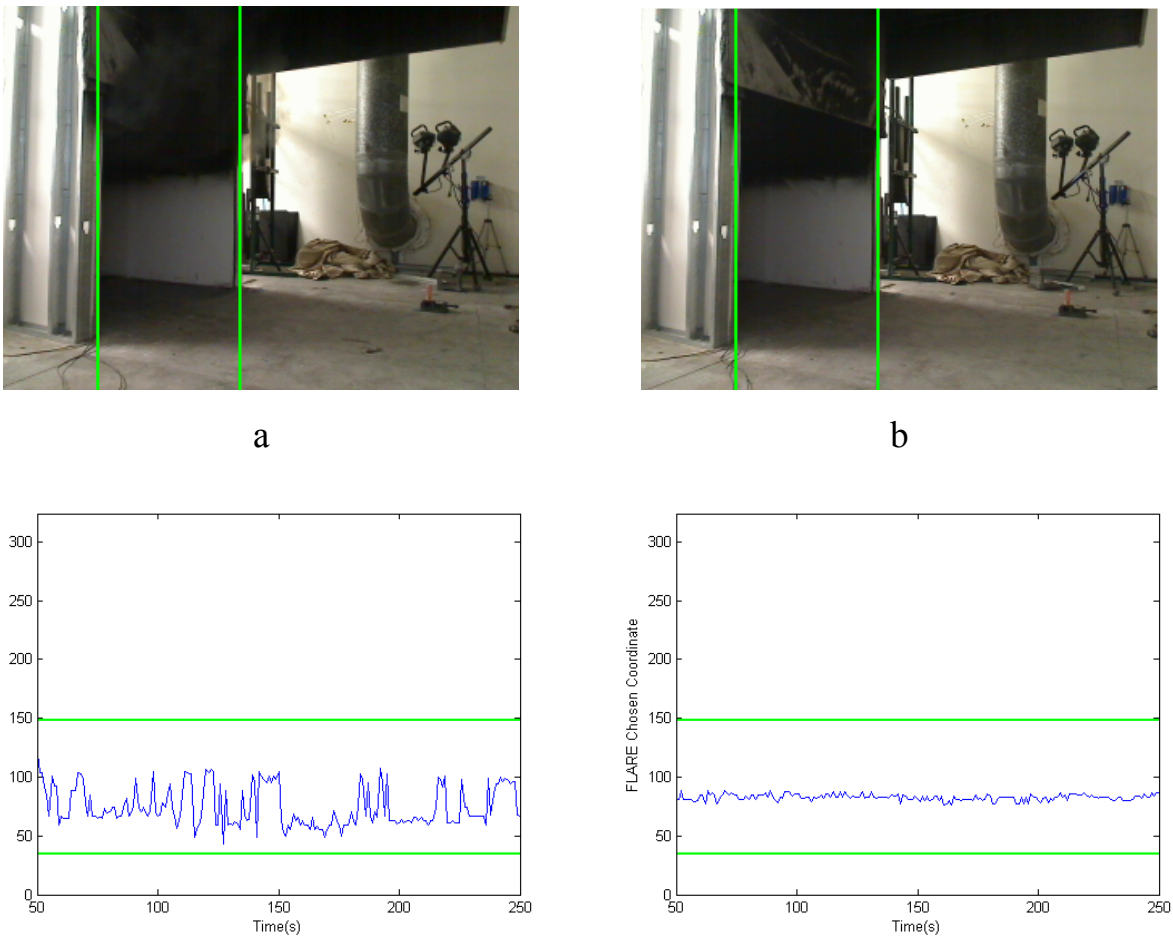

Figure C-1. Position A during basic FLARE test scenario. Results with (a) acceptable coordinate ranges shown in visible image for latex foam test, (b) acceptable coordinate ranges shown in visible image for propane test, (c) FLARE result pixel variation FLIR A35 during latex foam test, and (d) FLARE result pixel variation for FLIR A35 during 60 kW propane test

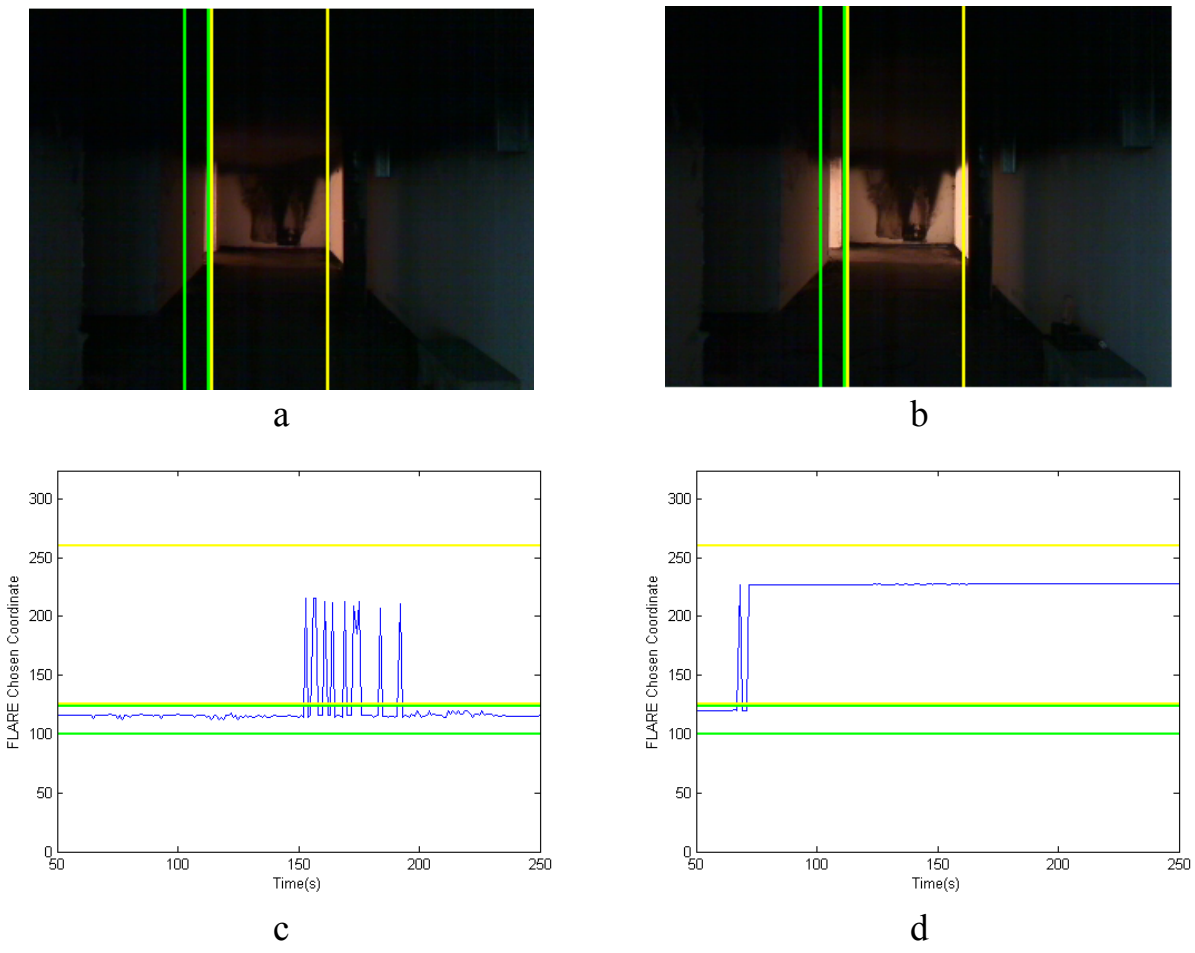

Figure C-2. Position B during basic FLARE test scenario. Results with (a) acceptable coordinate ranges shown in visible image for latex foam test, (b) acceptable coordinate ranges shown in visible image for propane test, (c) FLARE result pixel variation FLIR A35 during latex foam test, and (d) FLARE result pixel variation for FLIR A35 during 60 kW propane test

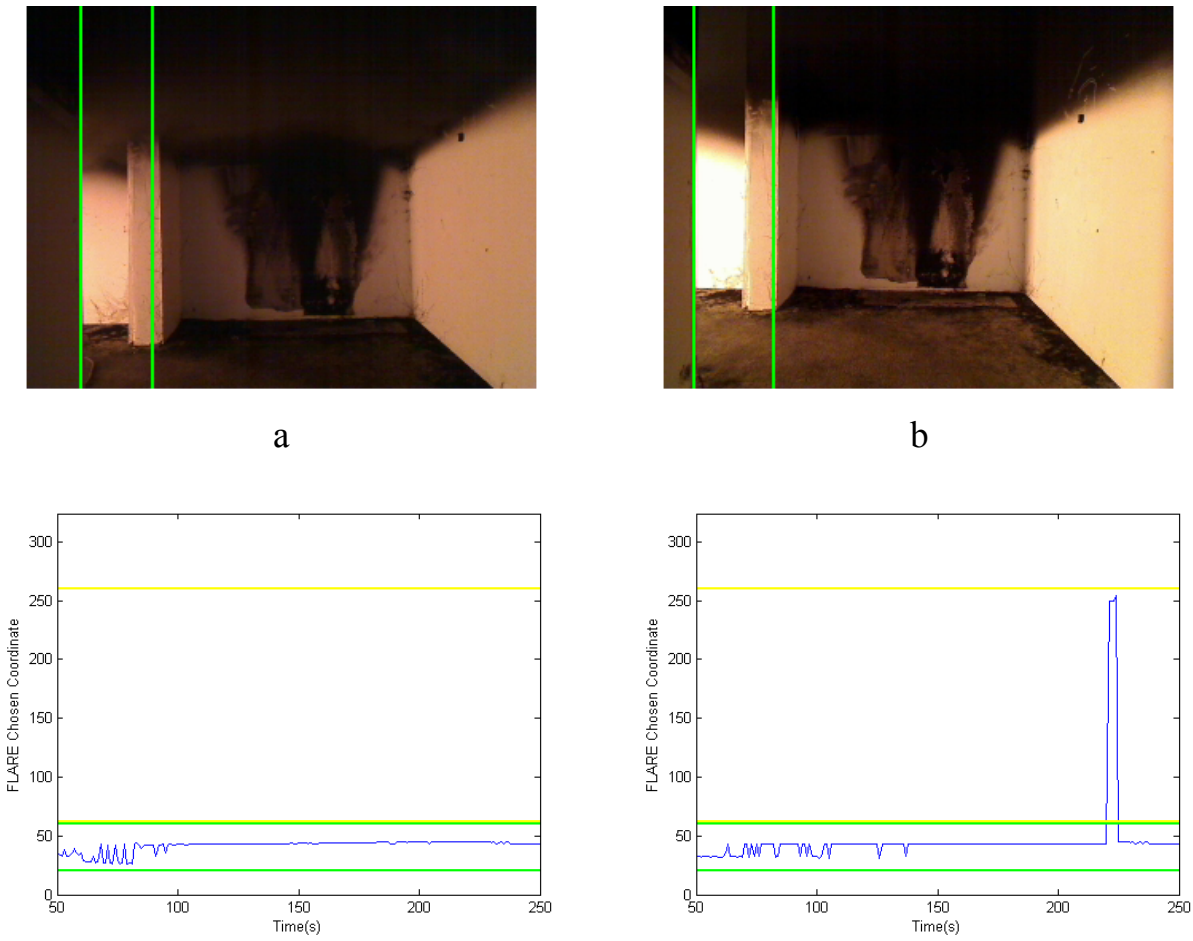

Figure C-3. Position C during basic FLARE test scenario. Results with (a) acceptable coordinate ranges shown in visible image for latex foam test, (b) acceptable coordinate ranges shown in visible image for propane test, (c) FLARE result pixel variation FLIR A35 during latex foam test, and (d) FLARE result pixel variation for FLIR A35 during 60 kW propane test

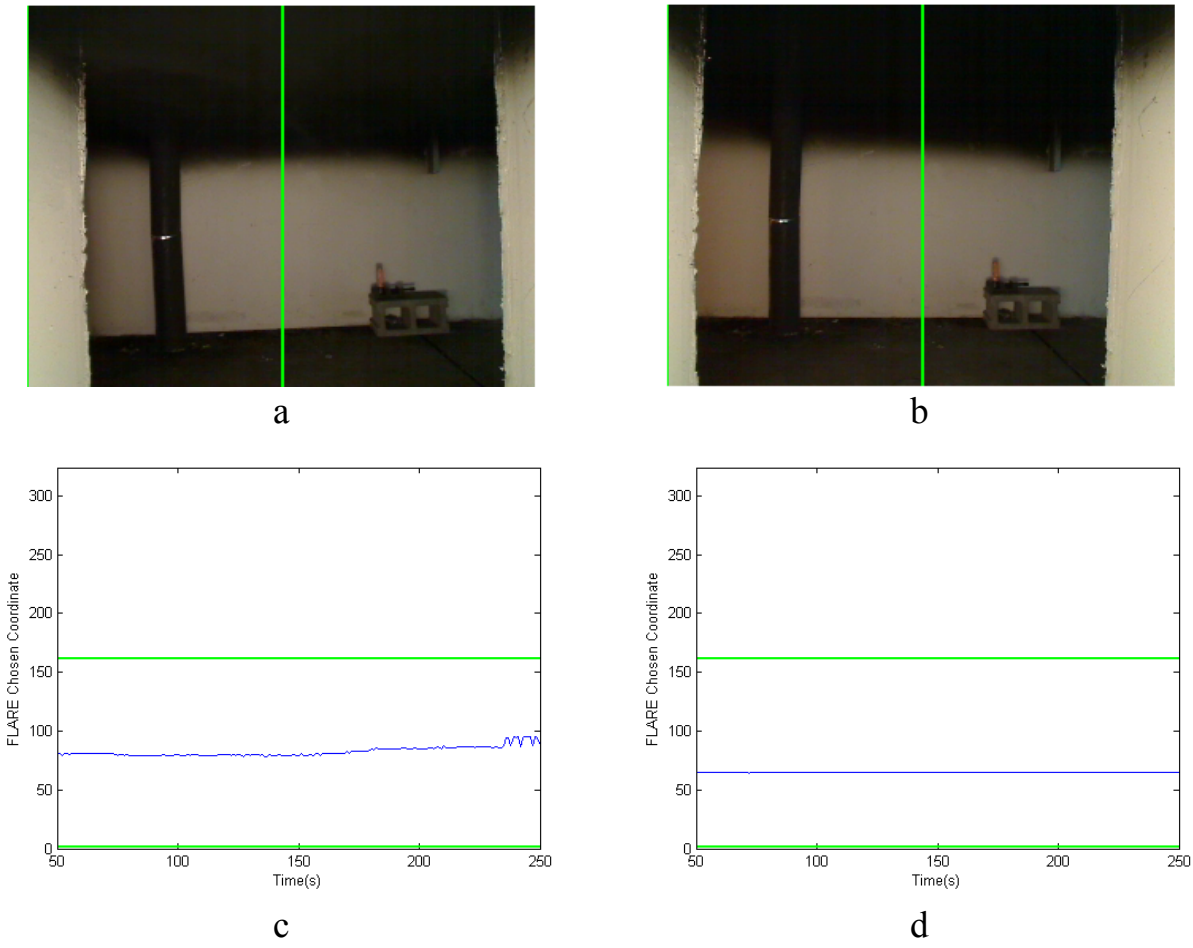

Figure C-4. Position D during basic FLARE test scenario. Results with (a) acceptable coordinate ranges shown in visible image for latex foam test, (b) acceptable coordinate ranges shown in visible image for propane test, (c) FLARE result pixel variation FLIR A35 during latex foam test, and (d) FLARE result pixel variation for FLIR A35 during 60 kW propane test

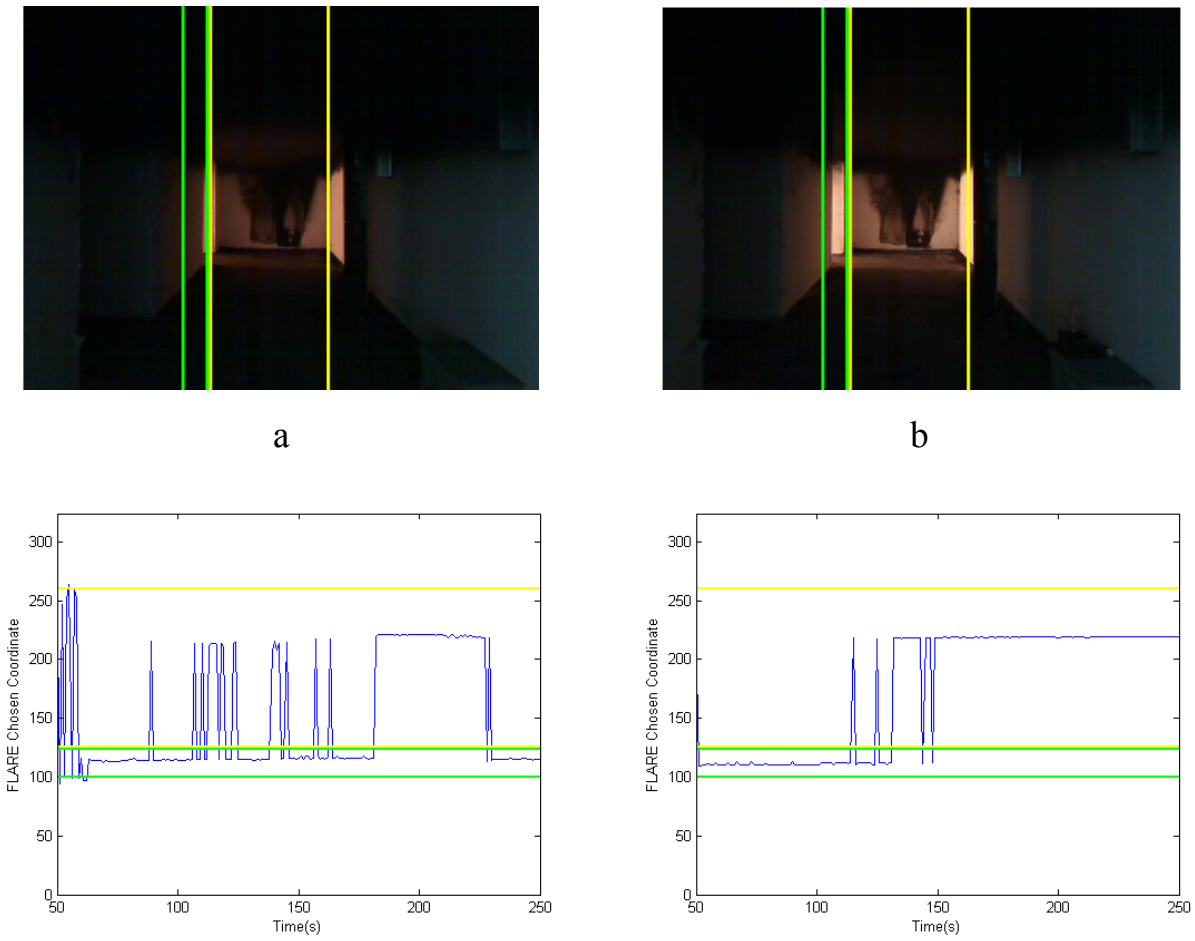

Figure C-5. Position B during FLARE heated pipe non-fire hot object test scenario. Results with (a) acceptable coordinate ranges shown in visible image for latex foam test, (b) acceptable coordinate ranges shown in visible image for propane test, (c) FLARE result pixel variation FLIR A35 during latex foam test, and (d) FLARE result pixel variation for FLIR A35 during 60 kW propane test

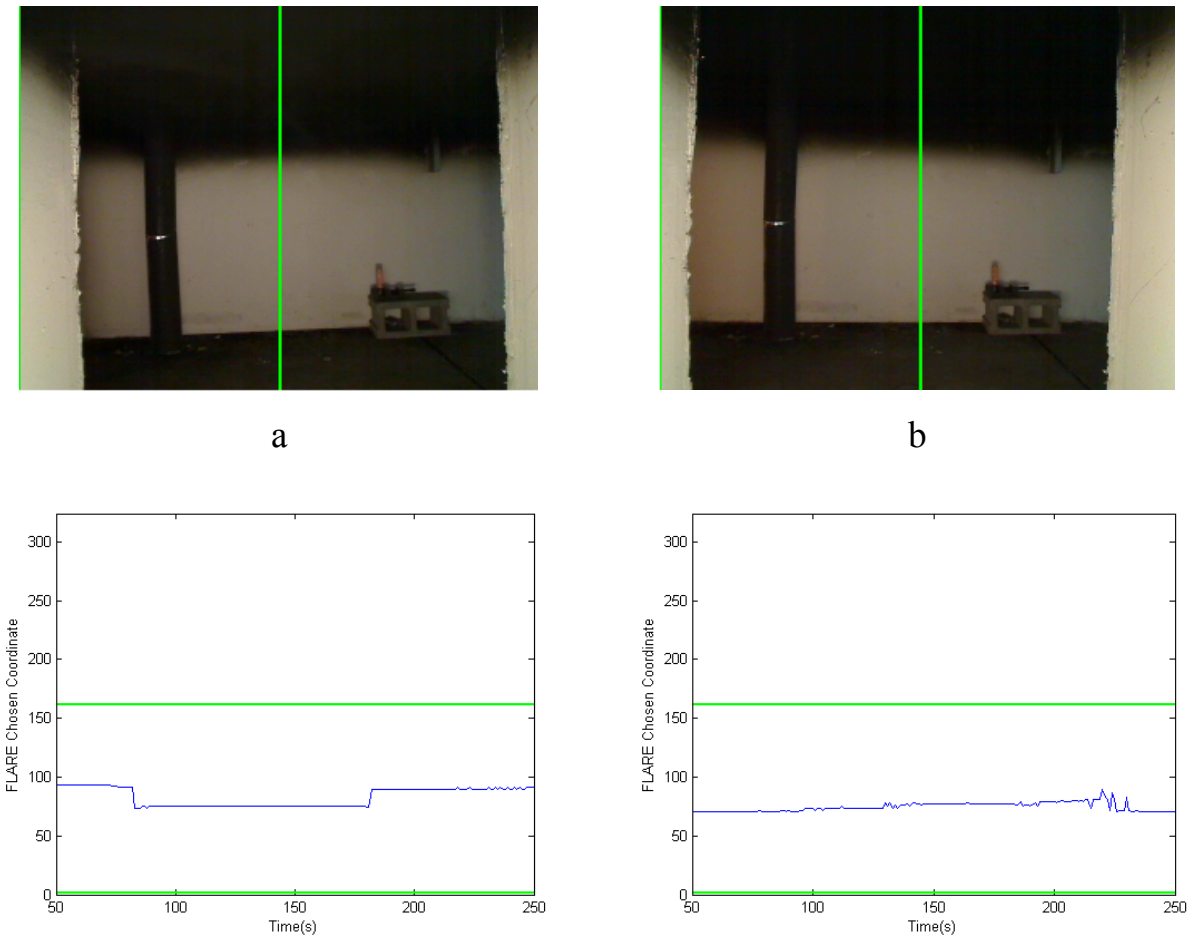

Figure C-6. Position D during FLARE heated pipe non-fire hot object test scenario. Results with (a) acceptable coordinate ranges shown in visible image for latex foam test, (b) acceptable coordinate ranges shown in visible image for propane test, (c) FLARE result pixel variation FLIR A35 during latex foam test, and (d) FLARE result pixel variation for FLIR A35 during 60 kW propane test

a

b

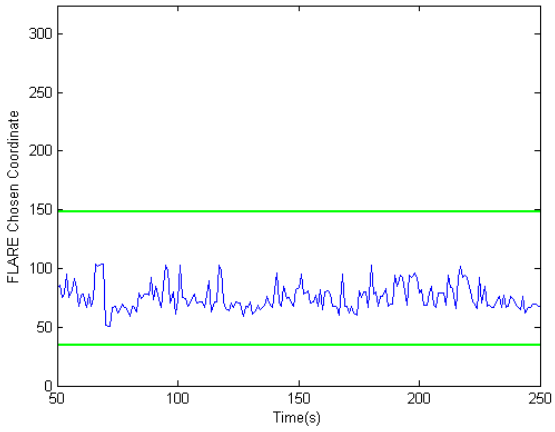

c

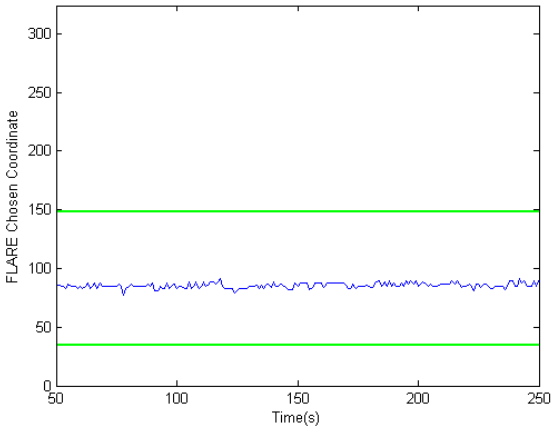

d

Figure C-7. Position A during FLARE non-fire hot object test scenario with heater. Results with (a) acceptable coordinate ranges shown in visible image for latex foam test, (b) acceptable coordinate ranges shown in visible image for propane test, (c) FLARE result pixel variation FLIR A35 during latex foam test, and (d) FLARE result pixel variation for FLIR A35 during 60 kW propane test

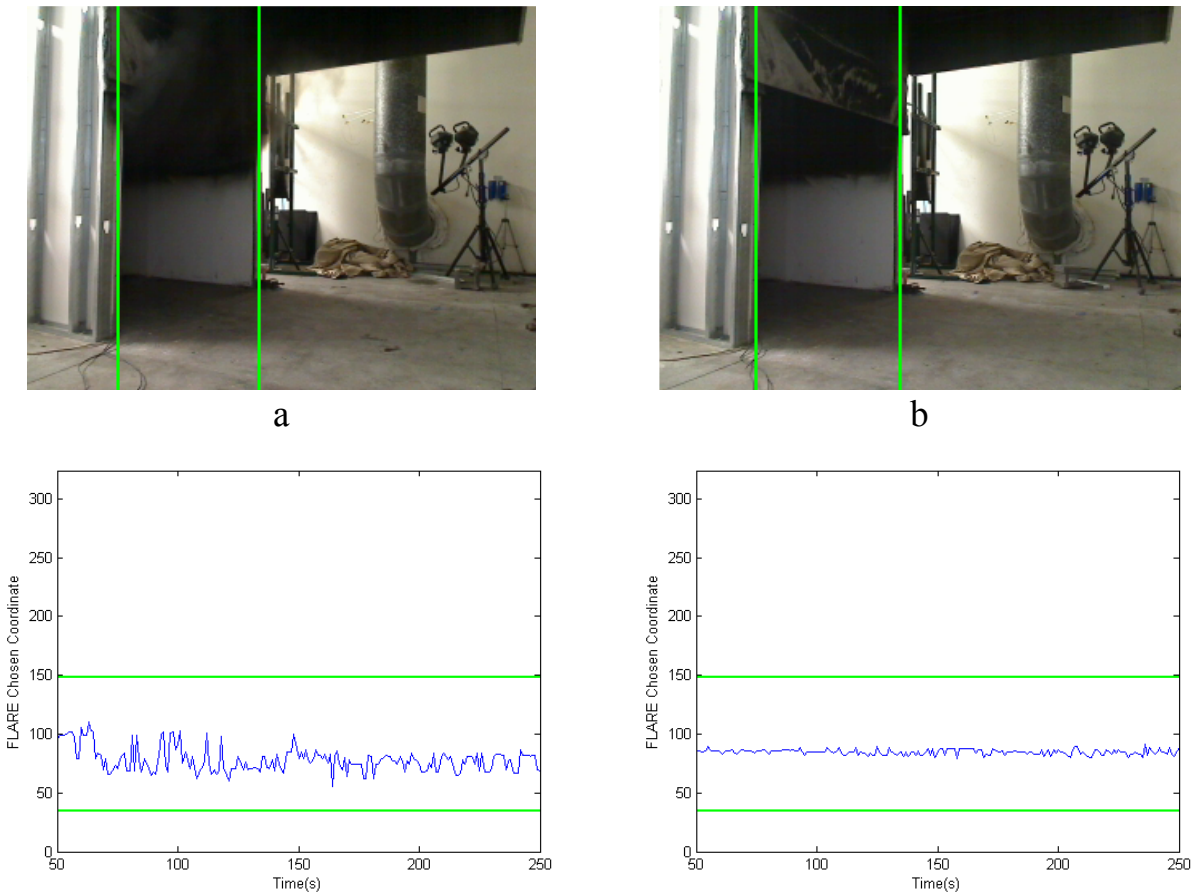

Figure C-8. Position A during FLARE non-fire hot object test scenario with heater near heading. Results with (a) acceptable coordinate ranges shown in visible image for latex foam test, (b) acceptable coordinate ranges shown in visible image for propane test, (c) FLARE result pixel variation FLIR A35 during latex foam test, and (d) FLARE result pixel variation for FLIR A35 during 60 kW propane test

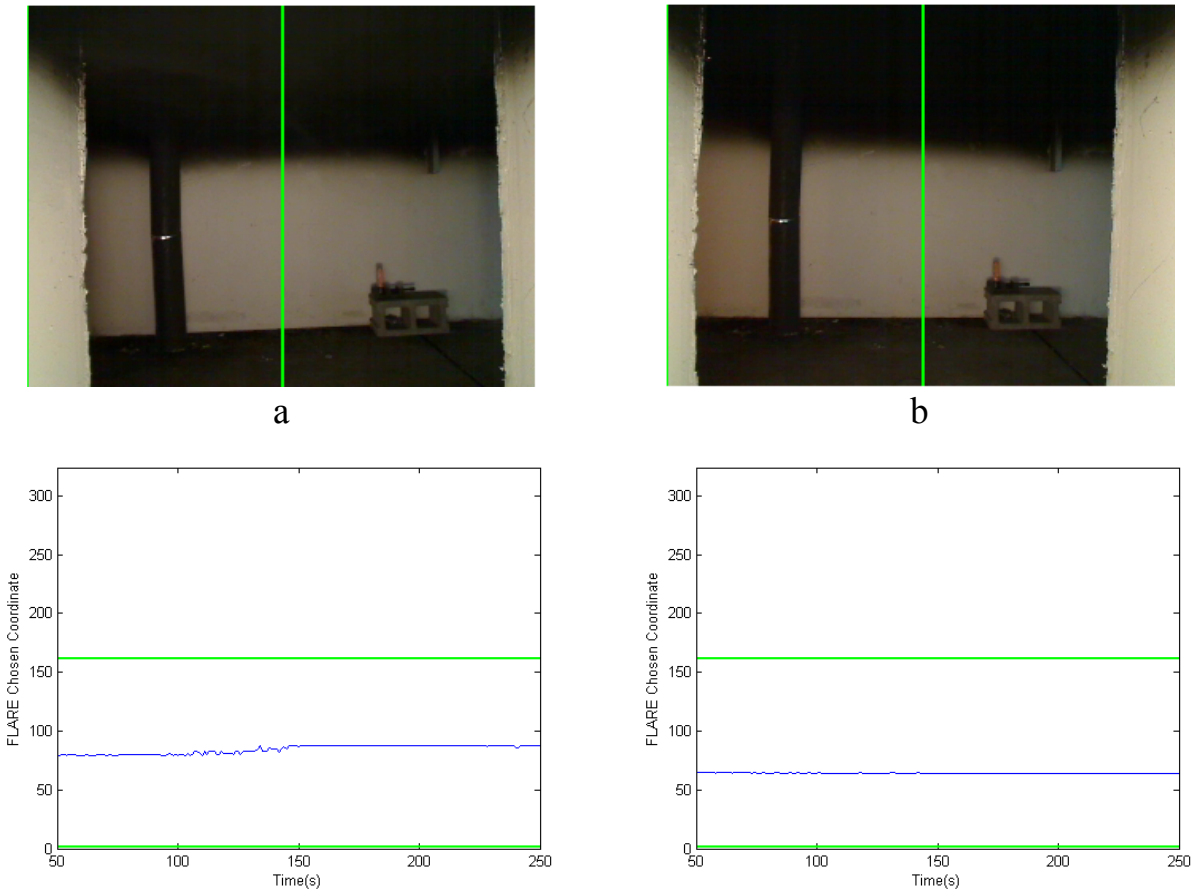

Figure C-9. Position D during FLARE non-fire hot object test scenario with a heater on the floor. Results with (a) acceptable coordinate ranges shown in visible image for latex foam test, (b) acceptable coordinate ranges shown in visible image for propane test, (c) FLARE result pixel variation FLIR A35 during latex foam test, and (d) FLARE result pixel variation for FLIR A35 during 60 kW propane test

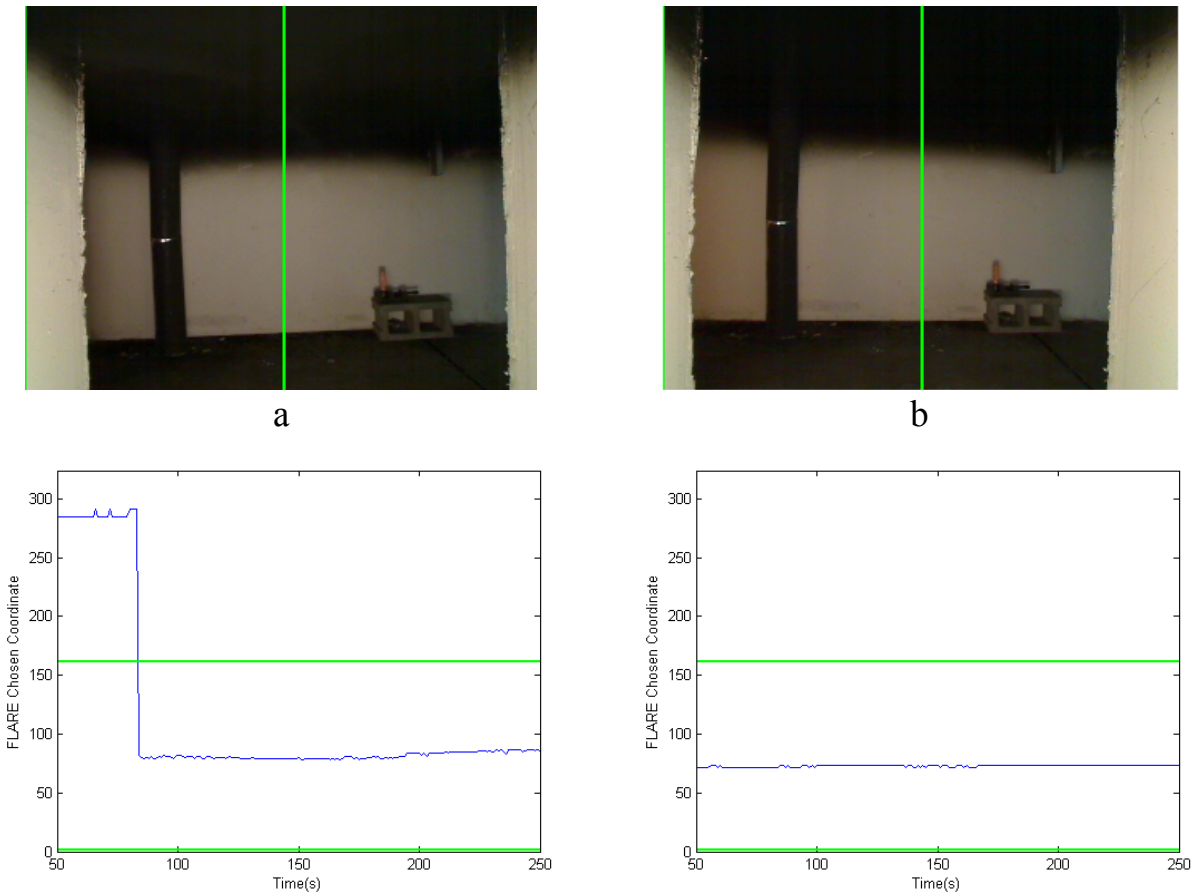

Figure C-10. Position D during FLARE non-fire hot object test scenario with a heater on the ceiling. Results with (a) acceptable coordinate ranges shown in visible image for latex foam test, (b) acceptable coordinate ranges shown in visible image for propane test, (c) FLARE result pixel variation FLIR A35 during latex foam test, and (d) FLARE result pixel variation for FLIR A35 during 60 kW propane test

Appendix D: Permissions

Hamamatsu

Dear Mr. Keller,

Thank you for using the Hamamatsu UVTRON in your research. We're delighted that it has been useful to you. Please feel free to use the figures from the R9454 and C10423 in your thesis.

Sincerely,

Leo Kohyama
Marketing Communications Manager
Hamamatsu Corporation
Phone: 408-615-3731
http://www.hamamatsu.com

- -